Chapter 11

Seasonality of Amazonian Rainforests

Myneni et al.

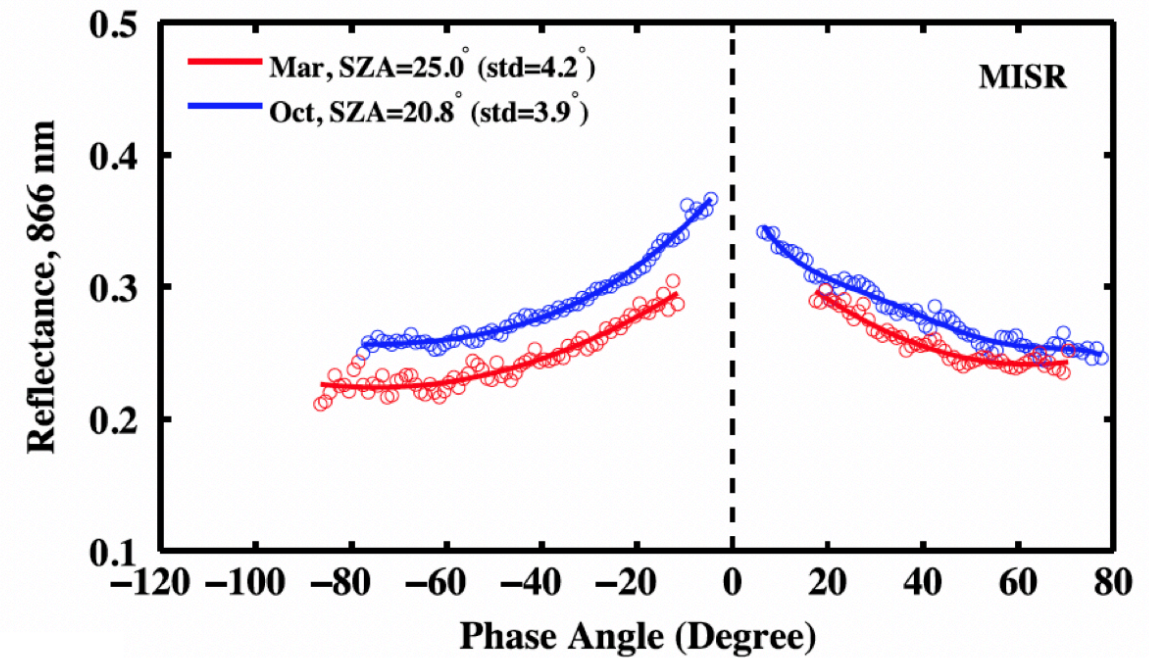

Large seasonal swings in leaf area of Amazon rainforests

Ranga B. Myneni[a], Wenze Yang[a,b], Ramakrishna R. Nemani[c], Alfredo R. Huete[d], Robert E. Dickinson[e,f], Yuri Knyazikhin[a], Kamel Didan[d], Rong Fu[e], Robinson I. Negrón Juárez[e], Sasan S. Saatchi[g], Hirofumi Hashimoto[h], Kazuhito Ichii[i], Nikolay V. Shabanov[a], Bin Tan[a,j], Piyachat Ratana[d], Jeffrey L. Privette[k,l], Jeffrey T. Morisette[m], Eric F. Vermote[k,n], David P. Roy[o], Robert E. Wolfe[p], Mark A. Friedl[a], Steven W. Running[q], Petr Votava[h], Nazmi El-Saleous[r], Sadashiva Devadiga[r], Yin Su[a], and Vincent V. Salomonson[s]

[a]Department of Geography and Environment, Boston University, 675 Commonwealth Avenue, Boston, MA 02215; [c]Ecosystem Science and Technology Branch, National Aeronautics and Space Administration (NASA) Ames Research Center, Mail Stop 242-4, Moffett Field, CA 94035; [d]Department of Soil, Water, and Environmental Science, University of Arizona, Tucson, AZ 85721; [e]School of Earth and Atmospheric Sciences, Georgia Institute of Technology, 311 Ferst Drive, Atlanta, GA 30332; [g]Jet Propulsion Laboratory, California Institute of Technology, 4800 Oak Grove Drive, Pasadena, CA 91109; [h]California State University at Monterey Bay and Ecosystem Science and Technology Branch, NASA Ames Research Center, Mail Stop 242-4, Moffett Field, CA 94035; [i]San Jose State University and Ecosystem Science and Technology Branch, NASA Ames Research Center, Mail Stop 242-4, Moffett Field, CA 94035; [k]Biospheric Sciences Branch, NASA Goddard Space Flight Center, 8600 Greenbelt Road, Mail Code 614.4, Greenbelt, MD 20771; [m]Terrestrial Information Systems Branch, NASA Goddard Space Flight Center, 8600 Greenbelt Road, Mail Code 614.5, Greenbelt, MD 20771; [n]Department of Geography, University of Maryland, College Park, MD 20742; [o]Geographic Information Science Center of Excellence, South Dakota State University, Wecota Hall, Box 506B, Brookings, SD 57007; [p]Raytheon Technology Services Corporation at NASA Goddard Space Flight Center, 8600 Greenbelt Road, Mail Code 614.5, Greenbelt, MD 20771; [q]School of Forestry, University of Montana, Missoula, MT 59812; [r]Science Systems and Applications, Inc., at NASA Goddard Space Flight Center, 8600 Greenbelt Road, Mail Code 614.5, Greenbelt, MD 20771; and [s]Department of Geography and Meteorology, University of Utah, Salt Lake City, UT 84112-0110

Contributed by Robert E. Dickinson, December 22, 2006 (sent for review June 5, 2006)

Despite early speculation to the contrary, all tropical forests studied to date display seasonal variations in the presence of new leaves, flowers, and fruits. Past studies were focused on the timing of phenological events and their cues but not on the accompanying changes in leaf area that regulate vegetation–atmosphere exchanges of energy, momentum, and mass. Here we report, from analysis of 5 years of recent satellite data, seasonal swings in green leaf area of ≈25% in a majority of the Amazon rainforests. This seasonal cycle is timed to the seasonality of solar radiation in a manner that is suggestive of anticipatory and opportunistic patterns of net leaf flushing during the early to mid part of the light-rich dry season and net leaf abscission during the cloudy wet season. These seasonal swings in leaf area may be critical to initiation of the transition from dry to wet season, seasonal carbon balance between photosynthetic gains and respiratory losses, and litterfall nutrient cycling in moist tropical forests.

remote sensing | tropical forests phenology | vegetation climate interaction

The trees of tropical rainforests are known to exhibit a range of phenological behavior, from episodes of ephemeral leaf bursts followed by long quiescent periods to continuous leafing, and from complete intraspecific synchrony to complete asynchrony (1). Several agents (e.g., herbivory, water stress, day length, light intensity, mineral nutrition, and flood pulse) have been identified as proximate cues for leafing and abscission in these communities (1–8). These studies were focused on the timing of phenological events but not on the accompanying changes in leaf area. Leaves selectively absorb solar radiation, emit longwave radiation and volatile organic compounds, and facilitate growth by regulating carbon dioxide influx and water vapor efflux from stomates. Therefore, leaf area dynamics are relevant to studies of climatic, hydrological, and biogeochemical cycles.

The sheer size and diversity of rainforests preclude a synoptic view of leaf area changes from ground sampling. We therefore used data on green leaf area of the Amazon basin ($\approx 7.2 \times 10^6$ km^2) derived from measurements made by the Moderate Resolution Imaging Spectroradiometer (MODIS) onboard the National Aeronautics and Space Administration's (NASA's) Terra satellite [see ref. 9 and supporting information (SI) *Materials and Methods*]. These data were expressed as one-sided green leaf area per unit ground area [leaf area index (LAI)].

Results

Seasonality in LAI Time Series. Leaf area data for the Amazon rainforests exhibit notable seasonality, with an amplitude (peak-to-trough difference) that is 25% of the average annual LAI of 4.7 (Fig. 1*A*). This average amplitude of 1.2 LAI is about twice the error of a single estimate of MODIS LAI, and thus is not an artifact of remote observation or data processing (see *SI Materials and Methods*). The aggregate phenological cycle appears timed to the seasonality of solar radiation in a manner that is suggestive of anticipatory and opportunistic patterns of leaf flushing and abscission. These patterns result in leaf area leading solar radiation during the entire seasonal cycle, with higher leaf area during the shorter dry season when solar radiation loads are high and lower leaf area during the longer wet season when radiation loads decline significantly. This seasonality is roughly consistent with the hypothesis that in moist tropical forests, where rainfall is abundant and herbivore pressures are modest, seasonal increase in solar radiation during the dry season might act as a proximate cue for leaf production (1, 2, 4).

In a community dominated by leaf-exchanging (10) evergreen trees, leaf area can increase if some of the older leaves that are photosynthetically less efficient because of epiphylls and poor stomatal control are exchanged for more numerous new leaves. Leaf area can decrease if the new leaves are less numerous than

Author contributions: R.B.M. and A.R.H. designed research; Y.K., R.I.N.J., H.H., K.I., N.V.S., B.T., P.R., and M.A.F. performed research; R.R.N., R.F., R.I.N.J., S.S.S., H.H., K.I., J.L.P., J.T.M., E.F.V., D.P.R., R.E.W., M.A.F., S.W.R., P.V., N.E.-S., S.D., and V.V.S. contributed new reagents/analytic tools; W.Y., K.D., and Y.S. analyzed data; and R.B.M., A.R.H., R.E.D., R.F., J.L.P., J.T.M., E.F.V., D.P.R., and S.W.R. wrote the paper.

The authors declare no conflict of interest.

Freely available online through the PNAS open access option.

Abbreviations: LAI, leaf area index; MODIS, Moderate Resolution Imaging Spectroradiometer.

[b]Present address: Department of Atmospheric, Oceanic, and Space Sciences, University of Michigan, 2455 Hayward Street, Ann Arbor, MI 48109.

[f]To whom correspondence should be addressed. E-mail: robted@eas.gatech.edu.

[j]Present address: Earth Resources Technology, Inc., 10810 Guilford Road, Suite 105, Annapolis Junction, MD 20701.

[l]Present address: Remote Sensing and Applications Division, National Oceanic and Atmospheric Administration, National Climatic Data Center, 151 Patton Avenue, Asheville, NC 28801.

This article contains supporting information online at www.pnas.org/cgi/content/full/0611338104/DC1.

© 2007 by The National Academy of Sciences of the USA

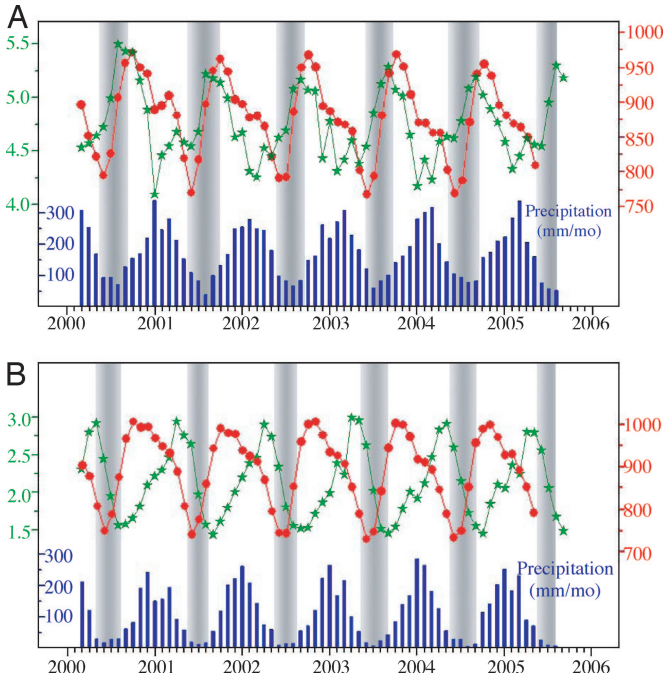

Fig. 1. Time series of monthly LAI from the Terra MODIS instrument (green), monthly maximum of hourly average surface solar radiation from the Terra Clouds and the Earth's Radiant Energy System (CERES) and Geostationary Operational Environmental Satellite 8 (GOES-8) instruments (red), and monthly merged precipitation from the Tropical Rainfall Measuring Mission (TRMM) and other sources (blue). (*A*) Time series based on data averaged over all Amazon rainforest pixels, as identified in the MODIS land cover map (SI Fig. 4*B*), south of the equator. The start of the data record is March 2000 and the end points are September 2005 (LAI), May 2005 (solar radiation), and August 2005 (precipitation). The shaded areas denote dry seasons, defined as months with precipitation <100 mm or less than one-third the precipitation range [0.33·(maximum–minimum) + minimum]. The solar radiation data are for all sky conditions and include direct and diffuse components. (*B*) Same as *A* except that the data are from savanna and grassland pixels adjacent to the Amazon basin in Brazil and south of the equator (SI Fig. 4*B*). The shaded areas denote dry seasons, defined as months with precipitation <50 mm. Information on the data is given in *SI Materials and Methods*.

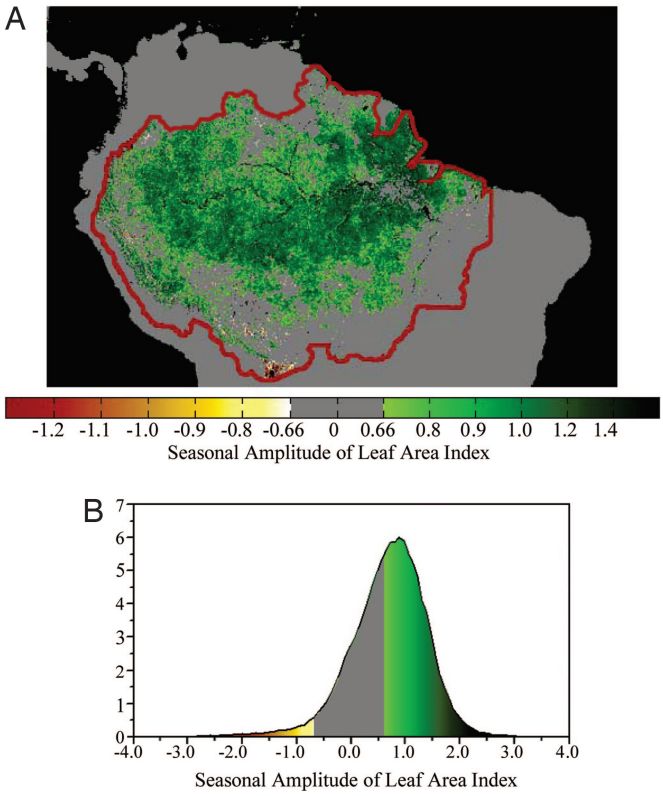

Fig. 2. Seasonal amplitude of LAI. (*A*) Color-coded map of LAI amplitudes greater than 0.66 or less than −0.66; this threshold (|0.66|) is the smallest LAI difference discernable with the MODIS LAI data set (see *SI Materials and Methods*). In regions with dry seasons longer than 3 months, the amplitude is calculated as the difference between the maximum 4-month average LAI in the dry season minus the minimum 4-month average LAI in the wet season. Where the dry season is three or fewer months, the amplitude is calculated as the difference between the dry-season average LAI and the minimum 4-month average LAI in the wet season. The dry and wet seasons are defined based on the precipitation data set at 15′ spatial resolution (see *SI Materials and Methods*). Thus, the seasons vary spatially and interannually. (*B*) Distribution of LAI amplitude for all Amazon rainforest pixels. The color scheme is similar to that in *A*.

the older ones that are dropped. If such exchanges are staggered in time among the individuals over a large area, for example due to asynchrony (7), they can result in a gradually increasing spatially averaged leaf area over a period of several months during the ascending phase of the seasonal cycle, and a gradually decreasing leaf area during the descending phase, while maintaining the evergreen character of the rainforest (Fig. 1*A*). These patterns of net leaf flushing and abscission also generate higher leaf litterfall in the dry season relative to the wet season, as reported in refs. 11–13. Such a leaf strategy will enhance photosynthetic gain during the light-rich dry season (14–19), provided the trees are well hydrated (2), and reduce respiratory burden during the cloudy wet season.

Leaf area changes in the adjacent grasslands and savannas in Brazil are concordant with rainfall data (Fig. 1*B*): higher leaf area in the wet season and lower leaf area in the dry season. This expected behavior imbues confidence in the opposing seasonality of deep-rooted and generally well hydrated (2), but light-limited (2, 4, 17, 18), rainforests inferred from the same LAI data set.

Geographic Details of Leaf Area Changes. The satellite data provide geographic details of leaf area changes in the Amazon (Fig. 2*A*). The region with a distinct seasonality of leaf area spans a broad contiguous swath of land that is anchored to the Amazon River, from its mouth in the east to its westernmost reaches in Peru, in the heart of the basin. This pattern is notable for at least two reasons. First, for its homogeneity; a higher dry-season leaf area relative to the wet season is observed in ≈58% of all rainforest-occupied pixels, whereas only 3% show the opposite change (Fig. 2*B*). Second, the homogeneous region roughly overlies the precipitation gradient (20) in the basin (see *SI Materials and Methods* and SI Fig. 4*C*), suggesting that the amplitude is, to a first approximation, independent of the duration and intensity of the dry season. For example, an amplitude of ≈1 LAI unit is observed in areas with two to five dry months in a year. Ostensibly, these forests maintain high leaf area (19, 21) and remain well hydrated during the dry season in nondrought years (see *SI Materials and Methods* and SI Fig. 5) via their deep root systems (2, 22) and/or through hydraulic redistribution (23, 24), which is also verified through a recent model study (see *SI Materials and Methods*: *Modeling GPP Seasonality of Amazon Rainforests by Constraining Rooting Depths*). Similar changes are not seen in ≈40% of the rainforest pixels, some of which represent transitional and drier rainforests to the south and east.

Correlation Among Changes in Leaf Area, Solar Radiation, and Precipitation. To associate quantitatively the changes in leaf area, solar radiation, and precipitation, we correlated the successive

ENVIRONMENTAL SCIENCES

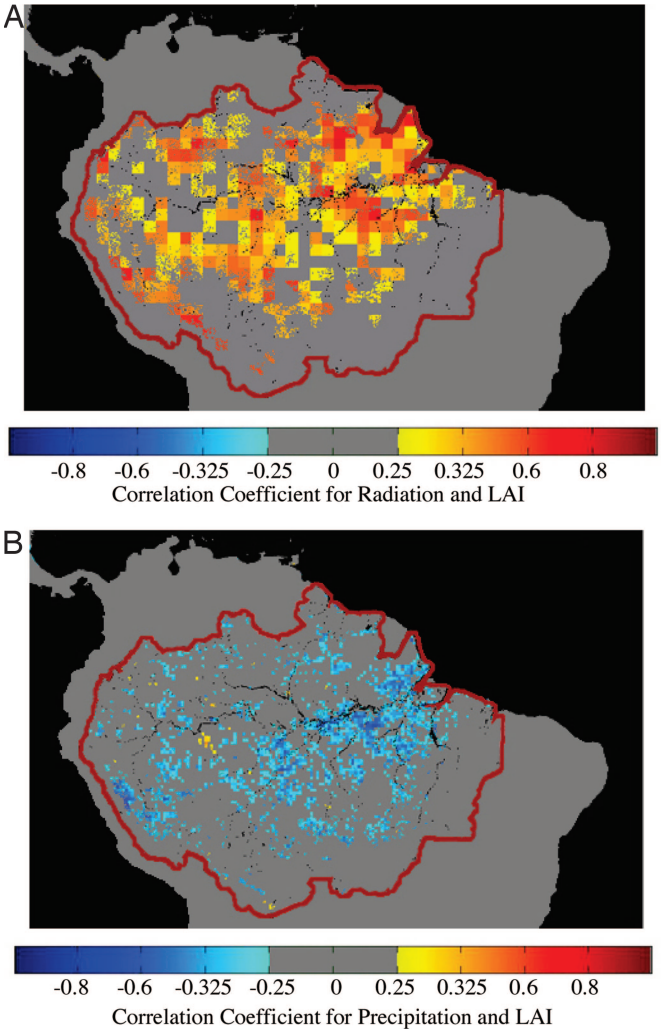

Fig. 3. Correlation coefficients. (*A*) Correlation between first differences of LAI and solar radiation. The first differences of LAI [ΔLAI(*t*)] are calculated as LAI($t + 1$) − LAI(t), where t is months in the timeline March 2000 to May 2005. The number of data points is 62 for each pixel. Correlation coefficients greater than 0.25 or less than −0.25 are shown ($P < 0.05$). The analysis was performed for rainforest pixels with LAI amplitudes greater than 0.66 or less than −0.66; this threshold (|0.66|) is the smallest LAI difference discernable with the MODIS LAI data set (see *SI Materials and Methods*). (*B*) Correlation between first differences of LAI and precipitation.

monthly differences of these variables, first by using the spatially averaged data shown in Fig. 1*A* and second by using pixel-level data. Changes in LAI are both positively correlated with changes in solar radiation ($P < 0.0001$) and negatively correlated with changes in precipitation ($P < 0.0001$), but the correlations between leaf area and radiation changes are larger and, at the pixel level, more numerous (Fig. 3 and SI Fig. 6). The negative correlations between LAI and precipitation are likely an indirect effect of the changes in cloudiness and radiation associated with precipitation changes (17). These results, together with past phenological studies, support the idea of an evolved pattern of endogenously controlled vegetative phenology that is timed to the seasonality of solar radiation (2, 10).

Discussion

The consistency between leaf area, solar radiation, and precipitation data from various satellite instruments is especially noteworthy. However, the strong seasonality in cloud cover and tropospheric aerosol loading may introduce seasonally opposing artifacts in MODIS leaf area. In the Amazon region there is significant cloudiness, which varies greatly between the wet and dry seasons. This seasonality in cloud cover can bias the results if cloud-contaminated retrievals are not screened out from the analysis. To minimize the impact of clouds, we used a coarse-resolution (8 km and monthly) data set that was derived by averaging the best-quality LAI values from the standard 1-km, 8-day MODIS data set (see *SI Materials and Methods*). Although some of the coarse-resolution LAI values were based on fewer high-quality estimates in the wet season, this did not bias the inferred seasonal LAI amplitudes.

The high aerosol content in the dry season, from biomass burning, natural biogenic emissions, and soil dust resuspension (25), can result in artificially low LAI values unless the reflectance data are corrected for aerosol effects. The MODIS processing system was found to correct well for such effects (see *SI Materials and Methods* and SI Fig. 7). The LAI values may have been underestimated by ≈5% from any residual aerosol effects. This effect is small and of opposite timing relative to the observed seasonality. Other possible sources of bias, such as reflectance saturation at high leaf area and changes in the light scattering and absorption properties of leaves due to aging and epiphylls (26), were found to be small and with the wrong timing to significantly alter our estimates of the amplitude of LAI seasonality (see *SI Materials and Methods*).

A robust validation of leaf area seasonality recorded in the MODIS satellite data requires a large number of leaf area measurements. These are presently lacking for the obvious reasons of cost, site accessibility, and the difficulty and questionable accuracy of ground sampling techniques. Nevertheless, the available data and published evidence support early to mid-dry season leaf area enhancement (21, 22), although further testing of this phenomenon is needed. The mechanism by which leaf area increases through the early dry season and decreases through the wet season (cf. Fig. 1) is partially supported by published observations on litterfall seasonality (11–13), but data on accompanying leaf emergence and expansion are lacking.

There is emerging evidence that the rainforest plays a critical role in initiating the onset of the wet season in the Amazon (ref. 27; see also *SI Materials and Methods*). An increase in surface evapotranspiration at the end of the dry season appears to be the primary cause of increased buoyancy of surface air, which consequently increases the probability of atmospheric convection and rainfall. The 25% increase in LAI over nearly 60% of the Amazon rainforest during the dry season reported in this article therefore suggests a potentially important role of vegetation in controlling the initiation of the wet season.

The seasonal dynamics and interplay between canopy photosynthesis and ecosystem respiration will likely be altered by this unexpected seasonality in leaf area (11, 14–19, 28), with attendant consequences for litterfall nutrient cycling (29). However, depending on other environmental and ecological constraints associated with vapor pressure deficits, temperatures, water and nutrient availability, etc., the dry-season increase in leaf area and sunlight may or may not result in enhanced photosynthetic activity. The transitional and seasonally dry forests in the southern Amazon do not show enhanced dry-season greening, which may indicate that these forests could be water-limited. A similar response can be envisioned for the more humid forests in drought years, especially those associated with strong El Niño events. Therefore, it is important to further investigate the significance of these changes in regard to climatic, hydrological, and biogeochemical cycles, and whether such swings in leaf area also exist in the moist forests of Africa and Asia.

Materials and Methods

A continuous record of data on green leaf area from the MODIS onboard NASA's Terra satellite was used to track leaf area changes over the Amazon basin from March 2000 to September 2005. An 8-km monthly LAI data set obtained by averaging the cloud-free main algorithm LAI estimates available in the standard 1-km, 8-day data set was used in this study. Monthly precipitation data at 15′ spatial resolution for the period January 1998 to August 2005, and monthly solar radiation data at 1° spatial resolution for the period March 2000 to May 2005, were also used. A detailed description of these data sets and of the validation of the MODIS LAI data set are given in *SI Materials and Methods* and SI Table 1.

This work was supported by grants from the National Aeronautics and Space Administration. V.V.S. is a Senior Scientist (Emeritus) of NASA Goddard Space Flight Center.

1. van Schaik CP, Terborgh JW, Wright SJ (1993) *Annu Rev Ecol Syst* 24:353–377.
2. Wright SJ (1996) in *Tropical Forest Plant Ecophysiology*, eds Mulkey SS, Chazdon RL, Smith AP (Chapman & Hall, New York), pp 440–460.
3. Morellato PC (2003) in *Phenology: An Integrative Environmental Science*, ed Schwartz MD (Kluwer, Dordrecht, The Netherlands), pp 75–92.
4. Wright SJ, van Schaik CP (1994) *Am Nat* 143:192–199.
5. Borchert R (1994) *Ecology* 75:1437–1449.
6. Schöngart J, Piedade MTF, Ludwigshausen S, Horna V, Worbes M (2002) *J Trop Ecol* 18:581–597.
7. Singh KP, Kushwaha CP (2005) *Curr Sci* 89:964–975.
8. Borchert R, Rivera G, Hagnauer W (2002) *Biotropica* 34:27–39.
9. Salomonson VV, Barnes WL, Maymon PW, Montgomery HE, Ostrow H (1989) *IEEE Trans Geosci Remote Sens* 27:145–153.
10. Borchert R (2000) in *Dormancy in Plants: From Whole Plant Behaviour to Cellular Control*, eds Viemont JD, Crabbe J (CABI, Wallingford, UK), pp 87–107.
11. Goulden ML, Miller SD, da Rocha HR, Menton MC, Freitas HC, Figueira AMS, de Sousa CAD (2004) *Ecol Appl* 14(Suppl):S42–S54.
12. Luizao FJ (1989) *Geo J* 19:407–417.
13. Rodrigues WA, Furch K, Klinge H (2001) *Amazoniana* 16:441–462.
14. Carswell FE (2002) *J Geophys Res* 107:8076.
15. Würth MKR, Peláez-Riedl S, Wright SJ, Körner C (2005) *Oecologia* 143:11–24.
16. Graham EA, Mulkey SS, Kitajima K, Phillips NG, Wright SJ (2003) *Proc Nat Acad Sci USA* 100:572–576.
17. Schuur EAG (2003) *Ecology* 84:1165–1170.
18. Nemani RR, Keeling CD, Hashimoto H, Jolly WM, Piper SC, Tucker CJ, Myneni RB, Running SW (2003) *Science* 300:1560–1563.
19. Huete AR, Didan K, Shimabukuro YE, Ratana P, Saleska S, Yang W, Nemani RR, Myneni RB, Hutyra L, Fitzjarrald D (2006) *Geophys Res Lett* 33:L06405.
20. Sombroek W (2001) *Ambio* 30:388–396.
21. Asner GP, Nepstad DC, Cardinot G, Ray D (2004) *Proc Nat Acad Sci USA* 101:6039–6044.
22. Nepstad DC, de Carvalho CR, Davidson EA, Jipp PH, Lefebvre PA, Negreiros GH, da Silva ED, Stone TA, Trumbore SE, Vieira S (1994) *Nature* 372:666–669.
23. da Rocha HR, Goulden ML, Miller SD, Menton MC, Pinto LDVO, de Freitas HC, Figueira AMES (2004) *Ecol Appl* 14(Suppl):S22–S32.
24. Oliveira RS, Dawson TE, Burgess SSO, Nepstad DC (2005) *Oecologia* 145:354–363.
25. Echalar F, Artaxo P, Martins JV, Yamasoe M, Gerab F, Maenhaut W, Holben B (1998) *J Geophys Res* 103:31849–31864.
26. Roberts DA, Nelson BW, Adams JB, Palmer F (1998) *Trees* 12:315–325.
27. Fu R, Li W (2004) *Theor Appl Climatol* 78:98–110.
28. Seleska SR, Miller SD, Matross DM, Goulden ML, Wofsy SC, da Rocha HR, de Camargo PB, Crill P, Daube BC, de Freitas HC, *et al.* (2003) *Science* 302:1554–1557.
29. Vitousek PM, Sanford RL, Jr, (1986) *Annu Rev Ecol Syst* 17:137–167.

Seasonal changes in leaf area of Amazon forests from leaf flushing and abscission

Arindam Samanta,[1,2] Yuri Knyazikhin,[1] Liang Xu,[1] Robert E. Dickinson,[3] Rong Fu,[3] Marcos H. Costa,[4] Sassan S. Saatchi,[5] Ramakrishna R. Nemani,[6] and Ranga B. Myneni[1]

Received 18 July 2011; revised 23 November 2011; accepted 1 December 2011; published 11 February 2012.

[1] A large increase in near-infrared (NIR) reflectance of Amazon forests during the light-rich dry season and a corresponding decrease during the light-poor wet season has been observed in satellite measurements. This increase has been variously interpreted as seasonal change in leaf area resulting from net leaf flushing in the dry season or net leaf abscission in the wet season, enhanced photosynthetic activity during the dry season from flushing new leaves and as change in leaf scattering and absorption properties between younger and older leaves covered with epiphylls. Reconciling these divergent views using theory and observations is the goal of this article. The observed changes in NIR reflectance of Amazon forests could be due to similar, but small, changes in NIR leaf albedo (reflectance plus transmittance) resulting from the exchange of older leaves for newer ones, but with the total leaf area unchanged. However, this argument ignores accumulating evidence from ground-based reports of higher leaf area in the dry season than the wet season, seasonal changes in litterfall and does not satisfactorily explain why NIR reflectance of these forests decreases in the wet season. More plausibly, the increase in NIR reflectance during the dry season and the decrease during the wet season would result from changes in both leaf area and leaf optical properties. Such change would be consistent with known phenological behavior of tropical forests, ground-based reports of seasonal changes in leaf area, litterfall, leaf optical properties and fluxes of evapotranspiration, and thus, would reconcile the various seemingly divergent views.

Citation: Samanta, A., Y. Knyazikhin, L. Xu, R. E. Dickinson, R. Fu, M. H. Costa, S. S. Saatchi, R. R. Nemani, and R. B. Myneni (2012), Seasonal changes in leaf area of Amazon forests from leaf flushing and abscission, *J. Geophys. Res.*, *117*, G01015, doi:10.1029/2011JG001818.

1. Introduction

[2] The spectral signatures of Amazon forests as measured by passive optical satellite sensors such as the Moderate Resolution Spectroradiometer (MODIS) are characterized by two distinguishing features, strong scattering in the near-infrared (NIR) from internal-leaf cellular structures, and equally strong absorption in the shorter red and blue wavelengths from chlorophyll and other pigments vital to the process of photosynthesis. The NIR reflectance, the fraction of incident solar radiation at NIR wavelengths reflected by a surface, of these forests is an order of magnitude greater than the reflectance at red and blue wavelengths (Figure 1 and Figure S1 in the auxiliary material), and in any given year, increases by about 23% during the dry season and similarly decreases during the following wet season (Figure 1) [also *Asner et al.*, 2004].[1] This large increase in NIR reflectance of Amazon forests during the light-rich dry season has been variously interpreted, but generally characterized as from a greening of the Amazon forests during the dry season [*Huete et al.*, 2006; *Xiao et al.*, 2006; *Brando et al.*, 2010; *Myneni et al.*, 2007]. The objective of this paper is to harmonize these divergent interpretations of dry season greening of Amazon forests.

[3] The MODIS Enhanced Vegetation Index (EVI) is defined by an algebraic manipulation of vegetation reflectances at NIR, red and blue wavelengths [*Huete et al.*, 2002]. It is principally sensitive to NIR reflectance, as one can readily deduce from its formulation (cf. Section 3.3, equation (4)). Not surprisingly, the EVI displays higher values in the late dry season compared to the wet season or early dry season [*Huete et al.*, 2006; *Xiao et al.*, 2006;

[1]Department of Geography and Environment, Boston University, Boston, Massachusetts, USA.
[2]Atmospheric and Environmental Research Inc., Lexington, Massachusetts, USA.
[3]Department of Geological Sciences, University of Texas at Austin, Austin, Texas, USA.
[4]Agricultural and Environmental Engineering, Federal University of Viçosa, Vicosa, Brazil.
[5]Jet Propulsion Laboratory, California Institute of Technology, Pasadena, California, USA.
[6]Biospheric Sciences Branch, NASA AMES Research Center, Moffett Field, California, USA.

Copyright 2012 by the American Geophysical Union.
0148-0227/12/2011JG001818

[1]Auxiliary materials are available in the HTML. doi:10.1029/2011JG001818.

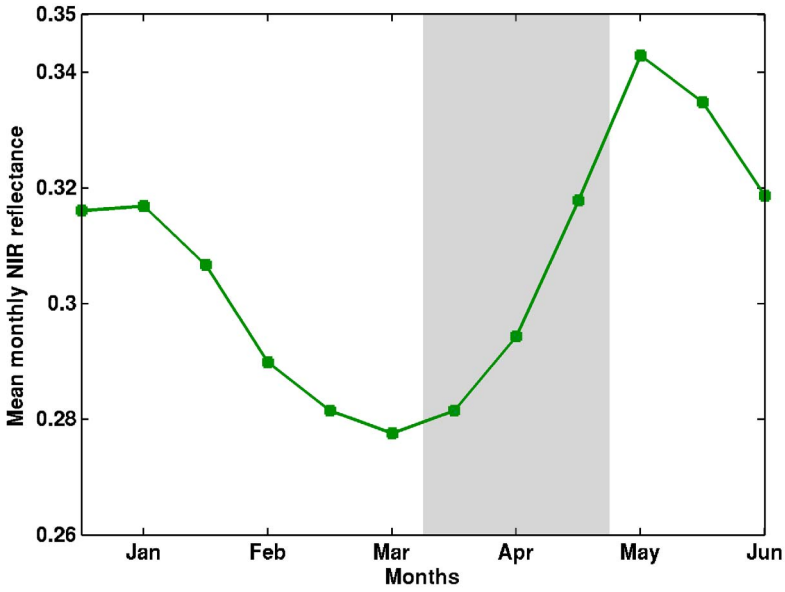

Figure 1. Monthly mean near-infrared (NIR) reflectance over forests, in the Amazon region 0°–20°S and 80°–40°W, with statistically significant green-up from June to October during 2000–2009 (Figure 6a).

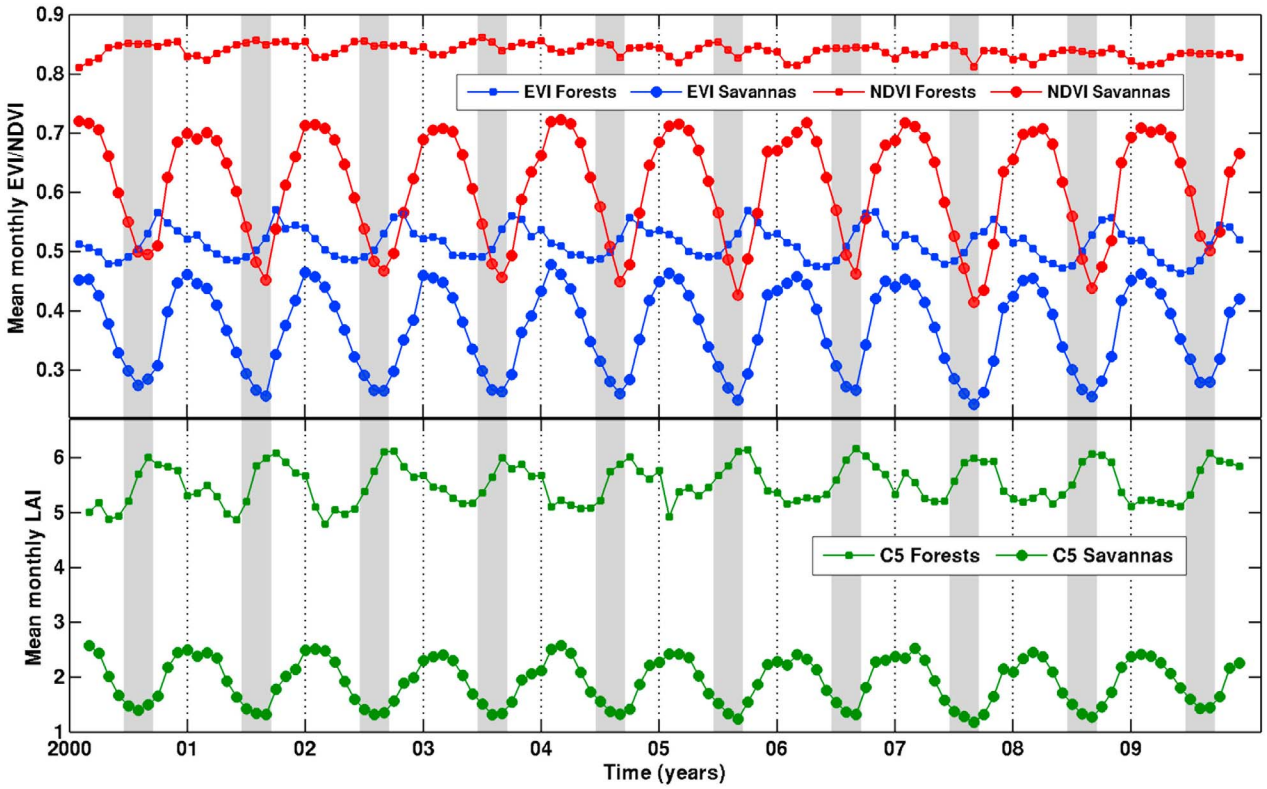

Figure 2. Monthly time series of EVI, NDVI and LAI over forests and savannas in the region 0°–20°S and 80°–40°W. Valid EVI and NDVI values are averaged over all forest pixels showing statistically significant green-up from June to October for EVI (Figure 6a). Similarly, valid LAI values are averaged over all forest pixels showing statistically significant increase in LAI (Figure 6c). Mean EVI, NDVI and LAI for savannas are the mean values over all savanna pixels in the region. The dry season, July to September, is shaded.

Brando et al., 2010] over the Amazon forests (Figure 2). What does an increase in EVI mean? Spatiotemporal changes in EVI are proposed to characterize similar variations in vegetation greenness [*Huete et al.*, 2002]. But, greenness itself is a poorly defined property of vegetation, unlike leaf area, for example. Nevertheless, a corresponding increase in dry season gross primary production (GPP) inferred from flux tower measurements at two experimental sites in Amazon forests [*Huete et al.*, 2006] lends credibility to the idea of enhanced greening, possibly from flushing of new leaves, during the light-rich dry season.

[4] The same seasonal changes in spectral reflectances of Amazon forests have been interpreted as resulting from large seasonal changes in green leaf area, a gradual increase through the dry season and a corresponding decrease through the wet season [*Myneni et al.*, 2007] (Figure 2). Green leaf area per unit ground area, or leaf area index (LAI) for short, is a physical attribute of vegetation, and thus measurable, and can be used to mechanistically quantify the exchange of energy, mass and momentum between the surface and the boundary layer [*Dickinson*, 1983]. The inferred seasonal swings in LAI were hypothesized to result from net leaf flushing in the light-rich dry season and net leaf abscission in the light-poor wet season, a behavior that is consistent with earlier reports of sunlight as the dominant proximate cue for leaf flushing in tropical forests [*Wright and van Schaik*, 1994] and not inconsistent with observations of enhanced GPP [*Huete et al.*, 2006] and carbon uptake [*Carswell et al.*, 2002; *Saleska et al.*, 2003] during the dry season, relative to the wet season, as younger leaves tend to be more photosynthetically vigorous than epiphyll-infested older leaves with poor stomatal control, as long as these light-limited forests [*Nemani et al.*, 2003; *Würth et al.*, 2005; *Graham et al.*, 2003; *Schuur*, 2003] remain well hydrated through deep roots [*Nepstad et al.*, 1994].

[5] The idea that tropical forests flush new leaves in response to various cues, and most prominently to sunlight, is not new [e.g., *Wright and van Schaik*, 1994]. However, the idea that these evergreen forests display large seasonal changes in leaf area is new [*Myneni et al.*, 2007]. It has also been argued by *Myneni et al.* [2007] that a gradually increasing leaf area enhances the evapotranspiratory water vapor flux into the atmosphere during the dry season, which would facilitate convection and increase the probability of rainfall during the late dry season, factors that influence a transition to the wet season [*Li and Fu*, 2004; *Fu and Li*, 2004]. Field-based studies support these ideas through reports of enhanced leaf area: 5.5 to 6.5 [*Carswell et al.*, 2002], 3.32 to 4.25 [*Pinto-Junior et al.*, 2010], 8% increase [*Malhado et al.*, 2009], a small increase [*Negrón Juárez et al.*, 2009] but consistent with work of *Myneni et al.* [2007], and a moderate increase in LAI [*Doughty and Goulden*, 2008]. Besides, higher (on average 30%) evapotranspiration fluxes have been observed during the dry season [*Juárez et al.*, 2007, 2008].

[6] Nevertheless, changes in vegetation canopy spectral reflectances do not necessarily imply changes in LAI. Changes in leaf optical properties from the exchange of older leaves for newer ones during the dry season, without changes in total leaf area, can also result in observed changes in vegetation canopy spectral reflectances. In fact, this has been the argument in one recent study [*Doughty and Goulden*, 2008], which reported disagreement between the seasonal course of MODIS LAI and ground-measured LAI. This is inconsistent with other data from the same forest in the Amazon that shows considerable litterfall in the wet season [*Xiao et al.*, 2005]. A more recent detailed analysis of litterfall data from 81 sites across the forests of tropical South America actually shows a relationship between litterfall and rainfall seasonality, with some evidence of high levels of litterfall during the wet season, in addition to the dry season [*Chave et al.*, 2010]. Nevertheless, a sensitivity analysis with a simple radiative transfer model confirmed [*Doughty and Goulden*, 2008] that changes in canopy reflectances could be explained from changes in leaf optical properties [*Roberts et al.*, 1998] alone. These findings have additional support from another study [*Asner and Alencar*, 2010], which suggested that the higher NIR canopy reflectance during the dry season could be due to enhanced new leaf area at the top of the canopy, with overall canopy leaf area remaining unchanged, presumably through abscission of more numerous older leaves in the bottom reaches of the canopy. Neither of these studies provided valid explanation for the observed decrease in NIR canopy reflectance during the wet season (Figure 1), although aging and epiphylls are invoked by *Doughty and Goulden* [2008] in a manner that is inconsistent with observations of leaf demography [*Reich et al.*, 2004] and phenological behavior (see Introduction by *Myneni et al.* [2007]) in tropical forests.

[7] This brings us to the heart of the debate: are the observed seasonal changes in NIR reflectance of Amazon forests (Figure 1) due to changes in leaf area, or to changes in leaf optical properties, or both? The proposition that changes in forest canopy reflectances are due alone to changes in leaf optical properties, as argued by *Doughty and Goulden* [2008] and *Asner and Alencar* [2010] and recently discussed by *Brando et al.* [2010], does not acknowledge ground-based measurements of seasonal leaf area changes [*Asner et al.*, 2004; *Carswell et al.*, 2002; *Pinto-Junior et al.*, 2010; *Malhado et al.*, 2009; *Negrón Juárez et al.*, 2009; *Doughty and Goulden*, 2008] and litterfall [*Xiao et al.*, 2005; *Chave et al.*, 2010], and emerging evidence regarding the role Amazon forests play in the transition from dry to wet season [*Li and Fu*, 2004; *Fu and Li*, 2004; *Juárez et al.*, 2007, 2008], all of which support the interpretation proposed by *Myneni et al.* [2007]. On the other hand, the argument that only leaf area changes explain changes of forest canopy reflectance ignores the very obvious changes in leaf optical properties between younger and older leaves and between healthy and epiphyll infested leaves. A way to reconcile these divergent views is the goal of this research.

[8] The rest of this paper is organized as follows: data and methods are described in Sections 2 and 3, respectively. Results are presented in Section 4, followed by discussion in Section 5. Finally, conclusions are presented in Section 6.

2. Data

2.1. Satellite Vegetation Data

[9] The latest version of NASA land products, Collection 5 (C5) Enhanced Vegetation Index (EVI), Normalized Difference Vegetation Index (NDVI) and Leaf Area Index (LAI) and landcover data sets are used in this study.

2.1.1. Collection 5 (C5) Vegetation Indices (VI)

[10] These are satellite data based measurements of vegetation greenness produced by NASA using blue (BRF_{BLUE}, 459–479 nanometers (nm)), red (BRF_{RED}, 620–670 nm) and near-infrared (BRF_{NIR}, 842–876 nm) band surface reflectance data, called Bidirectional Reflectance Factor (*BRF*), from the MODIS instrument aboard the Terra and Aqua satellites [*NASA Land Processes Data Active Archive Center* (*LP DAAC*), 2010a; *Huete et al.*, 2002]. VIs consist of NDVI and EVI. NDVI (1) is a radiometric measure of photosynthetically active radiation absorbed by canopy chlorophyll, and therefore, is a good surrogate measure of the physiologically functioning surface greenness level in a region [*Myneni et al.*, 1995]. NDVI has been used in many studies of vegetation dynamics in the Amazon [e.g., *Asner et al.*, 2000; *Dessay et al.*, 2004; *Ferreira and Huete*, 2004]. EVI (2) is also a measure of greenness that generally correlates well with ground measurements of photosynthesis [e.g., *Rahman et al.*, 2005; *Sims et al.*, 2008] and found to be especially useful in high biomass tropical broadleaf forests like the Amazon [*Huete et al.*, 2006]. C5 MODIS Terra VI data were used in this study.

$$NDVI = \frac{BRF_{NIR} - BRF_{RED}}{BRF_{NIR} + BRF_{RED}} \quad (1)$$

$$EVI = 2.5\frac{BRF_{NIR} - BRF_{RED}}{1 + BRF_{NIR} + 6BRF_{RED} - 7.5BRF_{BLUE}} \quad (2)$$

Two kinds of VI data sets were used, 1×1 km^2 and 16-day MOD13A2, and $0.05° \times 0.05°$ and 16-day MOD13C1, for the period February 2000–December 2009. The data set "Vegetation Indices 16-Day L3 Global 1 km" (MOD13A2) contains EVI (NDVI) at 1×1 km^2 spatial resolution and 16-day frequency. This 16-day frequency arises from compositing, i.e., assigning one best-quality EVI (NDVI) value to represent a 16-day period [*Huete et al.*, 2002]. This data set is available in tiles ($10° \times 10°$ at the equator) of Sinusoidal projection; 16 such tiles cover the Amazon region (approximately 10°N–20°S and 80°W–45°W). The data were obtained from the NASA Land Processes Data Active Archive Center (LP DAAC) (https://lpdaac.usgs.gov). The data set "Vegetation Indices 16-Day L3 Global 0.05Deg CMG" (MOD13C1) contains EVI (NDVI) at $0.05° \times 0.05°$ spatial resolution and 16-day frequency. These are "cloud-free spatial composites" of MOD13A2 [*LP DAAC*, 2010b].

2.1.2. Collection 5 (C5) Leaf Area Index (LAI)

[11] LAI is defined as the one-sided green leaf area per unit ground area in broadleaf canopies, and one-half the total surface area per unit ground area in needleleaf canopies (coniferous) [*Myneni et al.*, 2007]. LAI is operationally derived from atmospherically corrected surface reflectance in the red and NIR bands measured by the MODIS sensor onboard NASA's Terra and Aqua satellites [*LP DAAC*, 2010c]. The LAI retrieval algorithm ingests surface reflectances and their uncertainties, and information about land cover as well as sun and view geometry to estimate LAI from "look-up tables" (LUTs) pre-calculated using vegetation canopy radiative transfer model simulations [*Knyazikhin et al.*, 1998]. The C5 algorithm incorporates major improvements including an 8 biome input landcover map and refined LUTs, especially over woody biomes [*Shabanov et al.*, 2005]. The LAI product has been validated globally as well as at sites in the Amazon [*Yang et al.*, 2006; *Aragao et al.*, 2005], and has been used in studies of vegetation dynamics [e.g., *Myneni et al.*, 2007]. C5 MODIS Terra LAI data are used in this study.

[12] The data set "Leaf Area Index – Fraction of Photosynthetically Active Radiation 8-Day L4 Global 1 km" (MOD15A2) contains LAI at 1×1 km^2 spatial resolution and 8-day temporal frequency. This 8-day frequency arises from compositing, i.e., assigning one best-quality LAI value to represent an 8-day period. This data set is available in tiles ($10° \times 10°$ at the equator) of Sinusoidal projection; 16 such tiles cover the Amazon region (approximately 10°N–20°S and 80°W–45°W) [*LP DAAC*, 2010c]. The data were obtained from the NASA LP DAAC (https://lpdaac.usgs.gov) for the period February 2000–December 2009.

2.1.3. Landcover Data

[13] Land cover information was obtained from the "MODIS Terra Land Cover Type Yearly L3 Global 1 km SIN Grid" product (MOD12Q1). This is the official NASA C5 land cover data set [*LP DAAC*, 2009; *Friedl et al.*, 2010]. It consists of five land cover classification schemes at 1×1 km^2 spatial resolution. The International Geosphere Biosphere Programme (IGBP) land cover classification scheme was used to identify forest pixels in the Amazon region.

2.2. Leaf Spectral Data

[14] Leaf albedo (reflectance + transmittance) data in NIR were obtained from two published studies on the effects of age and epiphyll cover on leaf spectra in the Amazon [*Roberts et al.*, 1998; *Toomey et al.*, 2009]. Epiphylls comprise a wide range of organisms-lichens, liverworts, fungi, algae and bacteria-that infest leaf surfaces in humid tropical forests [*Toomey et al.*, 2009]. Epiphylls coat the surface of leaves, which decreases light interception in both the photosynthetically active (PAR, 400–700 nm) and NIR spectral intervals [*Roberts et al.*, 1998; *Toomey et al.*, 2009]. The data are categorized into two classes, age-based and epiphyll-based. The age-based class consists of new and old leaves: new leaves are about 70 days in age (late dry season), fully formed and with minimal infestation while old leaves are a year old (late wet season/early dry season) and moderately infested. Spectra for this class are available for four plants of the Caatinga (low density scrubs, woodlands and woodland forests) dominant *Aldina heterophylla* [*Roberts et al.*, 1998]. The epiphyll-based class comprises clean and colonized leaves; clean leaves refer to mature leaves with no epiphyll infestation while colonized leaves refer to mature leaves that are moderately colonized by epiphyll. Spectra for this category are available for two Caatinga dominants, *Pradosia schomburgkiana* and *Protium heptaphyllam* [*Roberts et al.*, 1998], and three Terra Firme (dense forests) dominants, *Byrsonima* cf *poeppigiana*, *Inga* cf *sertulifera* and *Porouma tomentosa* [*Toomey et al.*, 2009]. The higher leaf albedo of new leaves is due to greater transmittance, while reflectance changes are minimal. The effect of epiphyll infestation is to reduce both reflectance and transmittance; relative decline in

transmittance is greater than reflectance [*Roberts et al.*, 1998; *Toomey et al.*, 2009].

3. Methods

3.1. VI Data Quality

[15] The quality of VI (EVI/NDVI) data in each pixel can be assessed using the accompanying 16-bit quality flags, in both 1×1 km^2 as well as the $0.05° \times 0.05°$ products. Sets of bits, from these 16 bits, are assigned to flags pertaining to clouds and aerosols (details can be found in work by *Samanta et al.* [2010, 2011a, 2011b] and *Xu et al.* [2011]). Each 1×1 km^2 16-day composite VI value is considered valid when (a) VI data is produced—"MODLAND_QA" equals 0 (good quality) or 1 (check other QA), (b) VI Usefulness is between 0 and 11, (c) Clouds are absent—"Adjacent cloud detected" (0), "Mixed Clouds" (0) and "Possible shadow" (0), and (d) Aerosol content is low or average—"Aerosol Quantity" (1 or 2). Note that "MODLAND_QA" checks whether VI is produced or not, and if produced, its quality is good or whether other quality flags should also be checked. Besides, VI Usefulness Indices between 0 to 11 essentially include all VI data. Thus, these two conditions serve as additional checks. Each $0.05° \times 0.05°$ 16-day VI pixel is considered valid when (a) VI data is produced—"MODLAND_QA" equals 0 (good quality) or 1 (check other QA), (b) VI Usefulness is between 0 and 11, (c) Clouds are absent—"Adjacent cloud detected" (0) and "Mixed Clouds" (0), and (d) Aerosol content is low or average—"Aerosol Quantity" (1 or 2). Here, the utility of "MODLAND_QA" and VI Usefulness flags is the same as in the case of 1×1 km^2 VI validity.

3.2. LAI Data Quality

[16] The quality of LAI data in each 1×1 km^2 8-day pixel can be assessed using two accompanying 8-bit quality flags, FparLai_QC and FparExtra_QC (details can be found in work by *Samanta et al.* [2011b]). The validity of LAI was determined through a two-stage process: (1) a 1×1 km^2 8-day LAI pixel was considered valid when (a) data is of good quality—"SCF_QC" equals 0 (main algorithm without saturation) or 1 (main algorithm with saturation), (b) Clouds are absent—"CloudState" (0), "Cirrus" (0), "MODAGAGG_Internal_CloudMask" (0) and "MODAGAGG_Cloud_Shadow" (0). (2) As the 8-day LAI aerosol flag does not distinguish between average and high aerosol loadings nor reports climatology aerosols, valid 8-day values are averaged to 16-day LAI whose validity was further determined using MOD13A2 cloud and aerosol flags: (a) VI data is produced-"MODLAND_QA" equals 0 (good quality) or 1 (check other QA), (b) VI Usefulness is between 0 and 11, (c) Clouds are absent—"Adjacent cloud detected" (0), "Mixed Clouds" (0) and "Possible shadow" (0), and (d) Aerosol content is low or average-"Aerosol Quantity" (1 or 2). Valid 1×1 km^2 16-day values were averaged to obtain monthly LAI. Finally, valid 1×1 km^2 monthly LAI values are aggregated to 8×8 km^2 spatial resolution. This 8×8 km^2 monthly LAI data set spanning February 2000–December 2009 was used in this study.

[17] In order to test the effectiveness of the quality flags, we have analyzed the seasonal time series of surface reflectances and vegetation indices (VI) of both uncorrupted (clean) and corrupted (contaminated) data (Figure S1). Interaction of photons with dense Amazonian forests is characterized by strong scattering in near-infrared (NIR), and equally strong absorption in the shorter red and blue wavelengths. The NIR reflectance of these forests is an order of magnitude greater than the reflectance at red (blue) wavelengths. On the other hand, atmospheric influences scatter more strongly in the shorter red/blue wavelengths. Thus, NIR reflectance is much less affected by atmospheric effects in comparison to red (blue) reflectance, which is shown in Figure S1a. Contaminated red reflectances are artificially higher-almost double in magnitude in comparison to clean values (Figure S1a). The difference between clean and contaminated red reflectance remains steady during the course of the year, which indicates lack of bias due to seasonal changes in atmospheric effects, such as high aerosol loads in the dry season from biomass burning (e.g., as discussed by *Samanta et al.* [2010]). These changes in surface reflectances translate into lower estimates of surface greenness or VIs. NDVI reduces by about 24% and EVI by about 18%, especially during the dry season (Figure S1b). Moreover, *Myneni et al.* [2007] have reported that residual atmospheric effects reduce leaf area index (LAI) estimates by about 5% during the dry season. These results show that seasonal variations in atmosphere-corrupted data are inconsistent with those observed with clean data. Furthermore, any remaining residual atmospheric influences that would reduce seasonal changes in measured greenness are eliminated by ensuring that the observed increase in VIs is greater than the errors in VIs (as mentioned in the caption of Figure 6). Thus, we conclude that the seasonal changes in vegetation greenness reported in the manuscript are not an artifact of residual atmospheric effects in surface reflectances.

3.3. Saturation of NDVI

[18] Photosynthesizing (green) vegetation strongly absorbs in red and blue bands and scatters in the NIR band. NIR reflectance of dense canopies such as Amazonian forests is an order of magnitude higher than red reflectance (Figures 1 and S1). In such situations, the formulation of NDVI (1) renders it relatively insensitive to changes in NIR, which can be shown as follows:

$$\delta NDVI = \frac{2BRF_{RED}}{(BRF_{NIR}+BRF_{RED})^2}\delta BRF_{NIR} - \frac{2BRF_{NIR}}{(BRF_{NIR}+BRF_{RED})^2}\delta BRF_{RED}$$

$$\delta NDVI = \frac{2BRF_{RED}}{(BRF_{NIR}+BRF_{RED})^2}\delta BRF_{NIR}, \delta BRF_{NIR} \gg \delta BRF_{RED}$$

$$\frac{\delta NDVI}{NDVI} = 0.2\frac{\delta BRF_{NIR}}{BRF_{NIR}}, BRF_{NIR} \sim 10BRF_{RED} \quad (3)$$

Similarly, for EVI we can write,

$$\delta EVI = G\frac{(1+C1)BRF_{RED} - C2BRF_{BLUE} + L}{(BRF_{NIR} + C1BRF_{RED} - C2BRF_{BLUE} + 1)^2}\delta BRF_{NIR},$$

$$\delta BRF_{NIR} \gg \delta BRF_{RED}, \delta BRF_{BLUE}$$

$$\frac{\delta EVI}{EVI} = \left(\frac{\delta BRF_{NIR}}{BRF_{NIR}}\right)\left[\frac{1+0.325BRF_{NIR}}{0.9(1+1.225BRF_{NIR})}\right],$$

$$C1 = 6, C2 = 7.5, BRF_{NIR} \sim 10BRF_{RED}, BRF_{RED} \sim 2BRF_{BLUE} \quad (4)$$

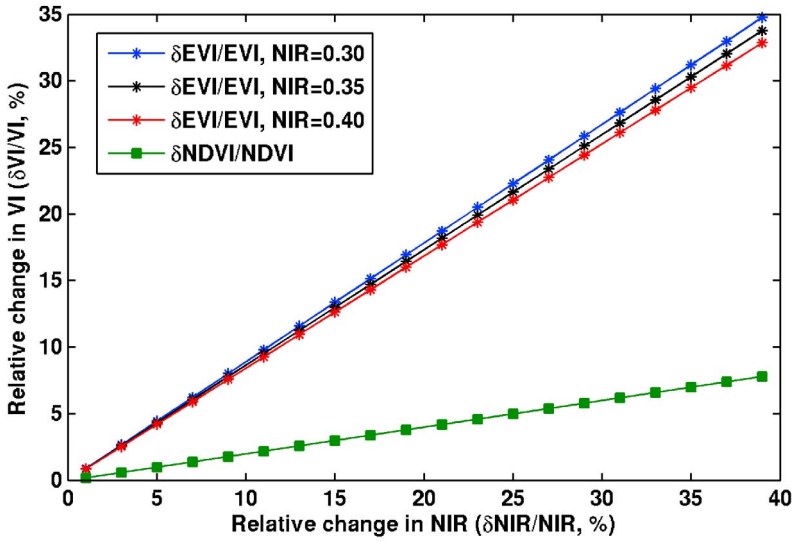

Figure 3. Sensitivity of Enhanced Vegetation Index (EVI) and Normalized Difference Vegetation Index (NDVI) to changes in near-infrared (NIR) reflectance (BRF_{NIR}) for dense vegetation. NIR reflectance is set at 10*red (BRF_{RED}) and 20*blue (BRF_{BLUE}), which is typically observed in dense canopies such as Amazon forests. Note that relative change in NDVI is independent of the magnitude of NIR reflectance.

Equation (4) implies that a given increase in NIR would translate into a five times lesser increase in NDVI (Figure 3). On the other hand, EVI is very sensitive to changes in NIR and does not exhibit the saturation problem (Figure 3).

3.4. Sensitivity of BRF to Variation in LAI and Leaf Optics

[19] The theory of spectral invariants [*Knyazikhin et al.*, 2010] was used to examine the sensitivity of the canopy near-infrared (NIR) *BRF* to LAI and leaf optical properties under saturation conditions. If the impact of canopy background on canopy reflectance is negligible as in the case of dense Amazonian forests, the spectral *BRF* can be approximated as [*Knyazikhin et al.*, 2010; *Schull et al.*, 2010; *Huang et al.*, 2008]:

$$BRF(\lambda,\Omega)=\frac{\rho(\Omega)\omega_\lambda}{1-p\omega_\lambda}i_0=\left[\frac{\rho(\Omega)}{1-p}i_0(\Omega_0)\right]\left[\frac{\omega_\lambda(1-p)}{1-p\omega_\lambda}\right]=K(\Omega,\Omega_0)W_\lambda \tag{5}$$

Here ρ is the directional escape probability, i.e., probability that a photon scattered by a leaf will escape the vegetation medium in a given direction Ω. It also can be interpreted as the probability of seeing a gap in the direction Ω from a leaf surface [*Stenberg*, 2007]. Spherical integration of ρ over all directions gives the total escape probability, $(1-p)$, where p is the recollision probability, i.e., the probability that a photon scattered by a leaf will interact with another leaf in the canopy again. Further, i_0, the probability of initial collision, or canopy interceptance, is the portion of incoming photons that collide with leaves for the first time. It depends on the direction of radiation incident on the vegetation canopy. Finally, ω_λ is the leaf albedo, which is the portion of the radiation incident on the surface of an individual leaf that the leaf transmits or reflects. In the present approach, this is the only variable that is dependent on the wavelength. It allows the parameterization of *BRF* in terms of leaf albedo rather than wavelength. Therefore wavelength dependence will be suppressed in further notations.

[20] Two separate factors are shown in equation (5), each exhibiting a different sensitivity to canopy structure and leaf optics. The wavelength independent ratio $P = \rho/(1 - p)$ gives the portion of gaps as seen from a leaf surface in a given direction Ω. This variable is sensitive to canopy geometrical properties such as spatial distribution of trees, ground cover, crown shape, size, and transparency [*Schull et al.*, 2010]. In the case of Amazon forests, changes in canopy structure over monthly time-scales are assumed negligible. At high LAI values, the canopy interceptance i_0 varies insignificantly with LAI due to the saturation. Under such conditions, the observed variation in NIR *BRF* is much stronger than corresponding variation in $K = Pi_0$, typically 2–3%, and thus changes in canopy structure alone cannot explain the observations (cf. Section 3.4.1).

[21] The second factor is the canopy scattering coefficient, $W_\lambda = \omega_\lambda\ (1 - p)\ /\ (1 - p\omega_\lambda)$ [*Smolander and Stenberg*, 2005], which depends on both canopy structure and leaf optics. It increases with the leaf albedo; the more the leaves scatter, the brighter the canopy is. Variations in LAI, however, trigger an opposite tendency. As the recollision probability increases with LAI [*Knyazikhin et al.*, 1998; *Smolander and Stenberg*, 2005; *Rautiainen et al.*, 2009], an increase in LAI results in more photon-canopy interactions and consequently a higher chance for photon to be absorbed. This mechanism makes the canopy appear darker. The effect of multiple scattering is described by the denominator in the equation for W_λ [*Huang et al.*, 2008], which in turn is fully determined by the product $\kappa = p\omega_\lambda$. An increase in κ not only enhances the effect of multiple scattering but also changes the sensitivity of the *BRF*: the closer its value is to unity, the stronger the response of canopy *BRF* to variations in canopy structure and leaf optics. If variation in K is negligible, changes in *BRF* can be reduced to examining variations in the scattering coefficient.

[22] The vegetation canopy is parameterized in terms of the recollision probability, $0 \le p \le 1$, leaf albedo, $0 \le \omega \le 1$, and the sensitivity parameter, $\kappa = p\omega \le \min(\omega, p)$. Let the sensitivity of *BRF* to canopy structure and leaf optics at time t and $t_1 = t + \Delta t$ be κ and $\kappa_1 = \kappa + \delta\kappa$, $\delta\kappa \ge 0$, respectively. Note that κ and κ_1 do not uniquely specify the recollision probabilities and leaf albedos since various combinations can result in the same values of the sensitivity parameter, which impact canopy reflective properties differently. To characterize the contribution of LAI to a change in the sensitivity parameter from by κ to $\kappa+\delta\kappa$, the following impact function is introduced:

$$k = \frac{\delta p/p}{\delta\kappa/\kappa} = \frac{\delta p/p}{\delta p/p + \delta\omega/\omega} \tag{6}$$

In general, k varies between $-\infty$ and $+\infty$. Values of k greater than 1 imply a decrease in leaf albedo, i.e., $\delta\omega/\omega < 0$. Variations in LAI and leaf optics make the vegetation darker in this case. On the other hand, a decrease in canopy structure, $\delta p/p < 0$, involves a negative value of the parameter k. In this case, changes in p and ω lead to brightening of the vegetated surface. This study will focus on the case when both LAI and leaf albedo increase, i.e., k varies between 0 (no change in LAI) and 1 (no change in leaf albedo). Such variations trigger competing processes: changes in LAI tend to darken the vegetation while variations in the leaf albedo suppress it. It should be emphasized, however, that this mechanism refers to the scattering coefficient W_λ and is applicable to $BRF = KW_\lambda$ (cf. equation (5)) if variations in K are negligible. In general, K increases with LAI and therefore compensates for a decrease in the canopy scattering coefficient. This lowers the darkening effect and even can result in an increase in the canopy *BRF* (cf. Sections 3.4.2 and 3.4.3).

[23] Under saturation conditions (i.e., $\delta BRF/BRF \gg \delta K/K$), the impact function ($k$), sensitivity parameter (κ), leaf albedo at time t (ω), variations $\delta BRF/BRF$, $\delta K/K$ and $\delta\kappa/\kappa$ are related as (cf. Section 3.4.1):

$$k(\omega) = \frac{\omega - \kappa}{\omega}\theta \tag{7}$$

where

$$\theta = \frac{1}{1-\kappa} - \beta, \beta = \frac{\delta BRF/BRF - \delta K/K}{\delta\kappa/\kappa} \tag{7a}$$

Here β characterizes the amplitude of the variability in reflectance. Since the goal of this study is to examine contributions of LAI and leaf albedo to large positive changes in the canopy *BRF* under saturation conditions, i.e., $\delta BRF/BRF \gg \delta K/K$, this analysis is restricted to the case when $\beta > 0$. It should be noted that in general, $\delta K/K$ is proportional to the impact function k (cf. Section 3.4.1). Under saturation conditions, this term can be neglected, and thus, equation (7) quantifies the impact of canopy structure on the *BRF* when both LAI and ω vary.

[24] If $k(\omega) = 1$ ($\delta\kappa/\kappa = \delta p/p$), then $(\omega-\kappa)\theta/\omega = 1$. This relationship holds true if and only if $\beta \le 0$ (cf. Section 3.4.1). It means that LAI alone cannot explain positive changes in canopy *BRF* under the saturation condition.

[25] If $k(\omega) = 0$ ($\delta\kappa/\kappa = \delta\omega/\omega$), then either $\omega = \kappa$ or $\theta = 0$. The former corresponds to an extreme and unrealistic case when $p = 1$. It means that photons cannot escape the vegetation canopy and therefore $BRF = 0$. The latter implies that variations in canopy *BRF* are proportional to $\delta\omega/\omega$, i.e.,

$$\frac{\delta BRF}{BRF} = \frac{1}{1-\kappa}\frac{\delta\omega}{\omega} \tag{8}$$

One can see that the closer the value of the sensitivity parameter is to unity, the stronger the response of the *BRF* to leaf albedo. Changes in leaf optics alone can explain a rather large range of variation in canopy reflectance under the saturation conditions.

[26] If $0 < k(\omega) < 1$ (i.e., $\delta p/p > 0$ and $\delta\omega/\omega > 0$), the contribution of LAI to the *BRF* is given by equation (7). It should be emphasized that this equation refers to the case when both LAI and the leaf albedo are changing. Figure 4 illustrates the LAI versus leaf albedo "competing process" under saturation conditions, which results in the observed *BRF* change by 23% ($\delta BRF/BRF = 0.23$ and $\delta BRF/BRF \gg \delta K/K = 0.01$, cf. Sections 3.4.2 and 3.4.3).

3.4.1. Derivation of Equation (7)

[27] It follows from equation (5) that

$$\frac{\delta BRF}{BRF} = \delta \ln BRF = \frac{\delta K}{K} + \frac{1}{1-p\omega}\left[\frac{\delta\omega}{\omega} - \frac{p(1-\omega)}{1-p}\frac{\delta p}{p}\right] \tag{9}$$

We parameterize the relative variation in *BRF* in terms of the sensitivity parameter, κ, its variation, $\delta\kappa/\kappa$, and the impact function, k, by substituting $p = \kappa/\omega$, $\delta p/p = k\delta\kappa/\kappa$ and $\delta\omega/\omega = (1-k)\delta\kappa/\kappa$ into equation (9). Solving the resulting equation for k yields equation (7).

[28] Case $k(\omega) = 1$: Letting $\delta\omega/\omega = 0$ in equation (9) and taking into account that $p(1-\omega)/(1-p\omega)(1-p)$ decreases with ω, one gets

$$-\frac{\delta p}{1-p} \le \frac{\delta BRF}{BRF} - \frac{\delta K}{K} \le 0 \tag{10}$$

Thus, a positive response of *BRF* to a positive variation in the recollision probability can be achieved if the parameter β defined by equation (7a) is negative.

3.4.2. Assumptions

[29] Since our goal is the qualitative description of the sensitivity of *BRF* to LAI and leaf albedo under the saturation conditions, we use a simple canopy model to specify the relationship between $\delta p/p$, δLAI/LAI and $\delta K/K$. We idealize the vegetation canopy as a spatially homogeneous layer filled with small planar elements of infinitesimally small sizes. All organs other than green leaves are ignored. For such a structurally simple uniform canopy, *Stenberg* [2007] found an analytical formula that relates the recollision probability, p, and canopy interceptance, $i_{0,d}$, under diffuse illumination condition, i.e.,

$$i_{0,d} = (1-p)LAI \tag{11}$$

Analyses of LAI-2000 data suggest the following relationship between $i_{0,d}$ and *LAI* [*Rautiainen et al.*, 2009]

$$i_{0,d} = 1 - \exp(-k_{CAN} \cdot LAI) \tag{12}$$

where the coefficient $k_{CAN} = 0.81$ was found to be almost insensitive to stand age, tree species or growing conditions. Finally, the canopy interceptance, i_0, can be estimated as $i_0 = 1 - \exp(-G \cdot \mathrm{LAI}/\mu_0)$ where G and μ_0 are the geometry

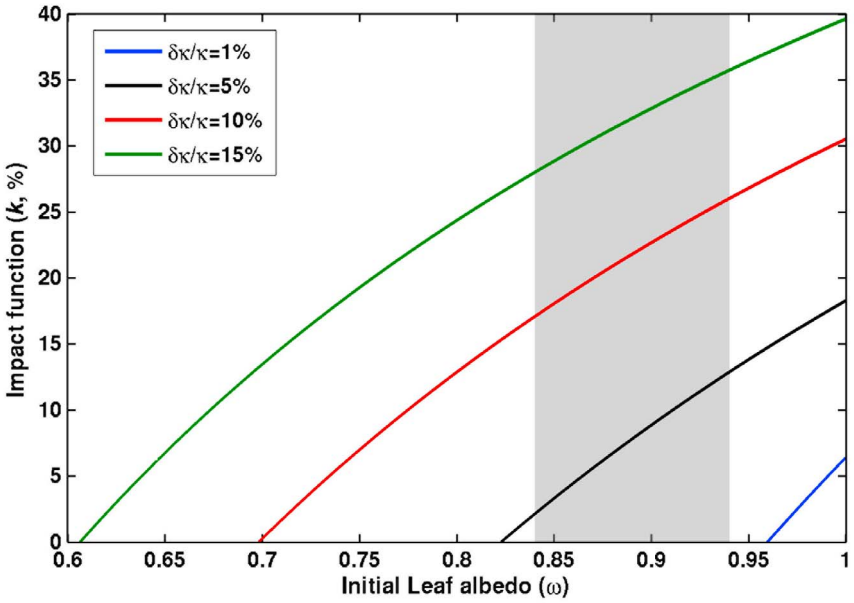

Figure 4. Impact function k (%) for a 23% increase in canopy near-infrared (NIR) bi-directional reflectance factor (*BRF*) and three values of the sensitivity parameter, $\kappa = 0.6$, 0.7, 0.82 and 0.96. The horizontal axis represents the initial value (late wet season/early dry season, June) of the leaf albedo ω, i.e., $\omega p = \kappa$. Each line corresponds to a fixed change in the sensitivity parameter from κ to $\kappa + \delta\kappa/\kappa$ and crosses the horizontal axis at the corresponding sensitivity parameter κ. Vertical axis shows the relative contribution of the recollision probability p to the 23% change in the NIR *BRF*. For example, if $\omega = 0.9$, a value of the recollision probability corresponding to $\kappa = 0.7$ is 0.7/0.9 = 0.78. For this combination of $p = 0.78$ and $\omega = 0.9$, the 23% change in *BRF* is attainable from changes in the recollision probability and leaf albedo by $k(0.9)\delta\kappa/\kappa = 0.23 \times 0.10 = 2.3\%$ (red curve) and $(1-k(0.9))\delta\kappa/\kappa = 0.77 \times 0.10 = 7.7\%$, respectively. The 2.3% change in $p = 0.78$ translates to an 11% increase in LAI of 4.5. The shaded region shows the range of initial NIR leaf albedo values (late wet season/early dry season, and leaves that are old and/or epiphyll infested) from field-based studies in the Amazon (cf. Section 2.2).

factor [*Ross*, 1981] and cosine of the solar zenith angle (SZA), respectively. It follows from this equation and equation (11) that

$$1 - i_0 = \left(1 - i_{0,d}\right)^{\alpha} \tag{13}$$

where $\alpha = G/(k_{CAN}\mu_0)$. For simplicity, the geometry factor G is set to $k_{CAN}\mu_0 = 0.81*\cos(30) = 0.81*0.87 = 0.70$ (mean SZA = 30°, std. = 5°–6° (20%)). The mean SZA for the dry season is about 30° and varies by about 5°–6° during this time, as reported in the MODIS VI data. Therefore, the small changes in SZA are not likely to induce large changes in μ_0, and G. Under the above assumptions, LAI is the only variable that fully describes canopy structure. The recollision probability (p) is an increasing function of LAI.

[30] We neglect angular dependence of the directional escape probability by replacing this term by its hemispherically integrated counterpart, i.e., $\rho(\Omega) = r/\pi$ where r is the probability that a scattered photon will escape the vegetation canopy through its upper boundary. Neglecting radiation transmitted through a very dense canopy, we get $\rho(\Omega) = (1 - p)/\pi$. The relative portion of gaps as seen from a leaf surface, $P = \rho/(1 - p)$, is approximated by a constant and thus $\delta K/K = \delta P/P + \delta i_0/i_0 \approx \delta i_0/i_0$. Note that this approximation is accurate for the uniform canopies with horizontally oriented leaves since such canopies transmit and reflect radiation diffusely and approximate for other canopies.

3.4.3. Properties of the Impact Function

[31] The impact function k requires specification of the parameter θ, which includes the term $\delta BRF/BRF - \delta K/K$ that appears in β. Our structurally simple canopy suggests negligible contribution of $\delta K/K \approx \delta i_0/i_0$ under the saturation conditions. For example, a change in LAI from 5 to 6 results in $\delta i_0/i_0 \approx 1\%$ which is significantly below the observed variation, $\delta BRF/BRF \approx 23\%$, in NIR surface reflectance. Although a more realistic canopy model can result in a different value of the relative variation in K, its use would not change our qualitative results as long as $\delta BRF/BRF \gg \delta K/K$. Figure 5 and the following properties of the impact function provide the necessary justification.

[32] If $\theta \geq 0$, the impact function k has the following properties (Figure 5).

$$\text{A. } \lim_{\omega \to 0+} k(\omega) = -\infty;$$

$$\text{B. } k(\kappa) = 0;$$

$$\text{C. } \lim_{\omega \to \infty} k(\omega) = \theta = \frac{1}{1-\kappa} - \beta;$$

[33] D. *If* $\theta > 1$, the equation $k(\omega) = 1$ has a unique solution given by $\omega^* = \kappa\psi$ where

$$\psi(\beta, \kappa) = \frac{\theta}{\theta - 1} = \frac{1 - \beta(1-\kappa)}{\kappa - \beta(1-\kappa)} = \frac{1}{\kappa} \quad \frac{1 - \beta(1-\kappa)}{1 - \beta\frac{1-\kappa}{\kappa}}$$

The function ψ increases with β and decreases with κ.

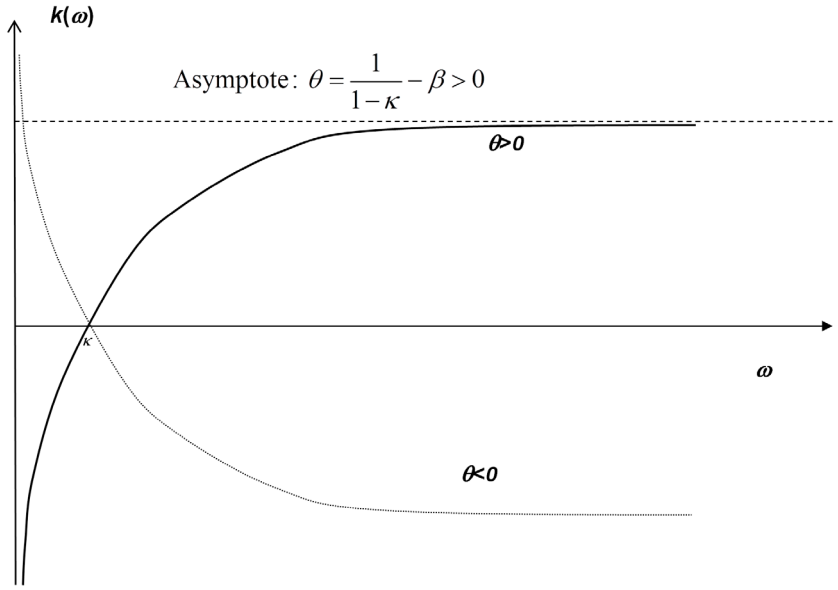

Figure 5. Schematics of properties A–C of the impact function $k(\omega)$. For positive θ, interpretation of $\delta BRF/BRF$ depends on the location of the asymptote relative to unity, i.e., whether $\theta \leq 1$ or $\theta > 1$ (i.e., property D described in Section 3.4.1).

[34] If $\theta \leq 0$, its properties can be formulated in a similar manner (see Figure 5). Let $\theta > 0$, i.e., $\beta < 1/(1 - \kappa)$. As one can see from Figure 5, interpretation of variation in the *BRF* depends on the location of the asymptote and the root of the equation $k(\omega) = 1$ relative to unity. The following cases are possible.

[35] Case 1: $0 < \theta < 1$, i.e., $\beta > \kappa/(1 - \kappa)$. The asymptote is below unity. If $\omega \leq \kappa$, the impact of canopy structure is negative (i.e., LAI should decrease in order to achieve a given variation in *BRF*). If $\omega > \kappa$, both the canopy structure and leaf optics have a positive impact. If θ tends to zero, the impact of canopy structure becomes negligible.

[36] Case 2: $\theta \geq 1$, i.e., $\beta \leq \kappa/(1 - \kappa)$. The asymptote is above unity. The equation $k(\omega) = 1$ has a solution given by $\omega^* = \kappa\psi$. Since ψ increases with β, the solution is above unity if $\beta > 0$; is equal to 1 if $\beta = 0$ and approaches to κ if β tends to $-\infty$. If κ tends to unity, the solution tends to unity, resulting in a jump from $k = 0$ to 1 at $\omega = \kappa$. Thus, if $\omega \leq \kappa$, the impact of canopy structure is negative. If $\kappa < \omega \leq \omega^*$, both structure and leaf optics positively contribute to variation in *BRF*. If $\omega > \omega^*$, the impact of structure is positive and leaf optics is negative.

[37] To summarize, a small variation in the parameter β does not change qualitatively the behavior of the impact function. Under saturation conditions, i.e., $\delta BRF/BRF \gg \delta K/K$, and the term $\delta K/K$ can be neglected.

4. Results

4.1. Comparison of Dry-Season Greening Patterns With Previous Studies

[38] Nearly 48% of Amazon forests (forests south of the Equator) display statistically significant EVI increase of about 16% from June to October in a given year during 2000–2009, which is in contrast to about 22% decline in EVI over the adjoining savannas from June to September (Figures 6a and 2). Approximately opposing changes are observed over these two vegetation types during the wet season (Figure 2). Interestingly, NDVI data do not show any appreciable changes in forests during the dry season (Figure 6b), or during other times of the year (Figure 2). However, the same data display large swings over savannas consisting of decline during the dry season and increase during the wet season, with an amplitude of about 41% (Figure 2). Further, LAI increase of about 0.93 units (18%) is observed over 33% of Amazon forests, while LAI decline of about 1.1 units is observed over adjacent Savannas during the dry season (Figures 6c and 2). These LAI variations are part of a seasonal cycle of opposing timing between forests and savannas (Figure 2). Thus, MODIS EVI and LAI data show large seasonal variations of approximately opposing timing over forests and savannas, with green-up of 16–18% over a third to half of Amazon forests during dry seasons of the decade 2000–2009.

[39] The spatial patterns of dry-season EVI increase seen here (Figure 6a) are consistent with a previous report [*Huete et al.*, 2006], albeit the magnitude of forest green-up is smaller (16% versus 25%) and is similar over a broad region extending across a large gradient in number of dry seasons, from the perpetually wet northwestern parts to the seasonally dry southeastern parts of the Amazon basin. Besides, the elimination of atmosphere-corrupted data (persistent during the dry season [e.g., *Samanta et al.*, 2010]) results in missing patches, especially in eastern Amazonia (Figures 6a and 6b). While the spatial patterns of dry-season enhancement in LAI (Figure 6c) are similar to those in work by *Myneni et al.* [2007], the extent (33% versus 68%) and average magnitude (0.93 versus 1.2) of LAI upswing are smaller than the previous estimate. These changes are attributable to the improved C5 LAI algorithm [*Shabanov et al.*, 2005] and

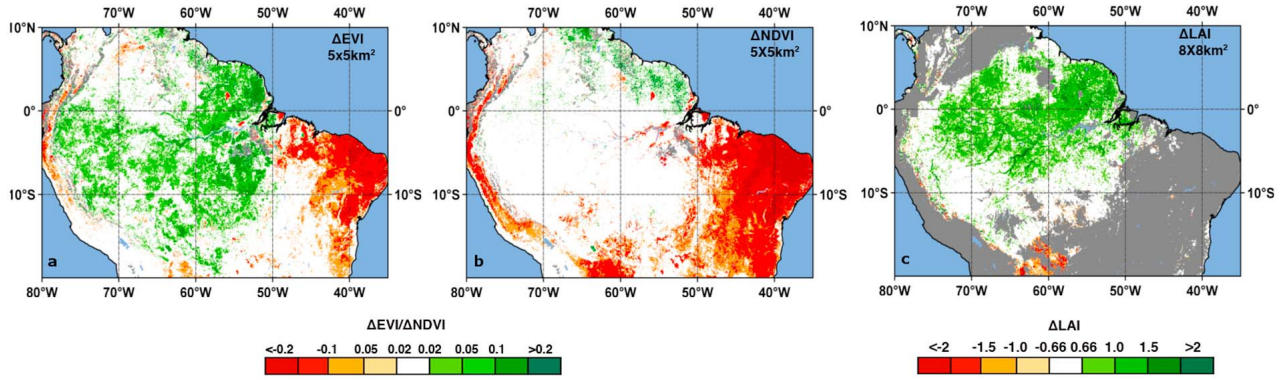

Figure 6. Spatial patterns of dry season greenness changes in the Amazon. (a) Change in Enhanced Vegetation Index (EVI), at 0.05° × 0.05° spatial resolution, from June (EVI_{jun}) to October (EVI_{oct}) expressed as ΔEVI (EVI_{oct} - EVI_{jun}) as in work by *Huete et al.* [2006]. Shown are only statistically significant changes i.e., $|\Delta EVI| >= |0.04*EVI_{jun} + 0.04|$ (2 standard deviation or 95% confidence interval of error in EVI_{jun} [*Vermote and Kotchenova*, 2008]). (b) Same as Figure 6a but for Normalized Difference Vegetation Index (NDVI). (c) Change in Leaf area index (LAI), at 8 × 8 km^2 spatial resolution, greater than 0.66 or less than −0.66. This threshold (|0.66|) is the smallest LAI difference discernable with the MODIS LAI data set. The amplitude, in regions with dry seasons longer than three months, is calculated as the difference between the maximum four-month average LAI in the dry season minus the minimum four-month average LAI in the wet season. Where the dry season is three or fewer months, the amplitude is calculated as the difference between the dry season average LAI and the minimum four-month average LAI in the wet season. The definition of the dry season is the same as in work by *Myneni et al.* [2007]. LAI difference for only forest pixels is shown as by *Myneni et al.* [2007]. Missing data are also shaded white.

with stricter screening of cloud-and aerosol-corrupted data. The patterns of seasonal greenness changes of Amazon forests observed with the latest version (C5) of MODIS greenness data are generally similar to previous reports.

4.2. Plausible Mechanisms of Dry-Season Increase in NIR Reflectance

[40] The cause of dry season increase in NIR BRF of Amazon forests (Figure 1) can be ascertained by assessing its sensitivity to LAI and leaf albedo (see Section 3.4; in this section, the term *BRF* is used instead of the more colloquial term, reflectance, to be technically consistent with the formulation in Section 3.4). This is determined by the sensitivity parameter ($\kappa = p\omega$), which couples vegetation canopy structure p (a function of LAI) and leaf albedo, ω. Positive changes in p and ω lead to an increase in the sensitivity parameter κ, which in turn alters how the *BRF* responds to changes in canopy structure and leaf optics. An increase in canopy *BRF* can be due to changes in (*i*) the sensitivity parameter from κ to $\kappa_1 = \kappa + \delta\kappa$ and (*ii*) canopy structure from p to $p_1 = p + \delta p$ and leaf optics from ω to $\omega_1 = \omega + \delta\omega$ such that $\kappa_1 = p_1\omega_1$ (cf. Section 3.4). The observed dry season increase in NIR *BRF* can be achieved variously, as discussed below.

4.2.1. Increase in LAI and Leaf Albedo Unchanged

[41] In this case, $\delta p/p > 0$ and $\delta\omega/\omega = 0$, i.e., $k = 100\%$ and $\delta\kappa/\kappa = \delta p/p$ (see Section 3.4). Variation in *BRF* does not exceed variation in K (see equation (5)), resulting in a negative value of the parameter β (cf. Section 3.4.1). In other words, adding more leaf area with the same spectral properties as the rest of the canopy will not change the observed canopy reflectance. Thus, the observed change in NIR *BRF* cannot be achieved by only increasing LAI.

4.2.2. Increase in Leaf Albedo and LAI Unchanged

[42] In this case, $\delta p/p = 0$ and $\delta\omega/\omega > 0$, i.e., $k = 0$ and $\delta\kappa/\kappa = \delta\omega/\omega$ (see Section 3.4). The relationship between variation in *BRF* and leaf albedo is given by (equation (8)), which suggests a strong response of the *BRF* to variation in leaf albedo. This response becomes stronger as the sensitivity parameter approaches unity, which is typical of dense vegetation and leaf albedo at NIR wavelengths. For instance, the observed 23% increase in NIR *BRF* can be attained through an increase in ω by $\delta\omega/\omega = 6.9\%$ for $\kappa = 0.7$ and any combination of ω and p such that $\omega p = \kappa = 0.7$. In the case of Amazonian forests, possible combinations could be $\omega = 0.9$ and $p = 0.78$ (which corresponds to LAI = 4.5), or $\omega = 0.88$ and $p = 0.8$ (LAI = 5). Thus, variations in leaf optics alone can explain the observed *BRF* changes, consistent with the arguments by *Doughty and Goulden* [2008], *Asner and Alencar* [2010], and *Brando et al.* [2010].

4.2.3. Increase in Both LAI and Leaf Albedo

[43] In this case, $\delta p/p > 0$ and $\delta\omega/\omega > 0$, i.e., $0 < k < 100\%$ and $\delta\kappa/\kappa = \delta\omega/\omega + \delta p/p$ (see Section 3.4). Changes in leaf optics and LAI that can lead to the observed dry season variation in *BRF* depend on the sensitivity parameter κ and its increment $\delta\kappa$. This is illustrated in Figure 4. For instance, consider a 10% change in the *BRF* sensitivity from $\kappa = 0.7$ (in early dry season, June) to $\kappa_1 = 0.77$ (in late dry season, September/October) ($\delta\kappa/\kappa = 0.10$). This case is described by the red curve in Figure 4. Assuming $\omega = 0.9$ in June (horizontal axis in Figure 4), the impact of canopy structure to *BRF* change is $k(0.9) = 23\%$ (vertical axis in Figure 4). It means that the 23% increase in NIR *BRF* would require an

increase in p of 2.3% ($k(0.9)$, $\delta\kappa/\kappa = 0.23 \times 0.10 = 2.3\%$; $p = \kappa/\omega = 0.78$ in June to $p_1 = 0.80$ in September/October) which translates into an 11% increase in LAI of 4.5. The corresponding increase in leaf albedo is 7.7% [$(1 - k(0.9))\delta\kappa/\kappa = 0.77 \times 0.10$]. In this example, a larger increment of the leaf albedo is required to achieve a given increase in *BRF* compared to the previous case of $\kappa = 0.7$ and unchanged LAI ($\delta\omega/\omega = 6.9\%$). Thus, variation in both leaf optics and LAI can equally well explain the observed *BRF* change, not inconsistent with *Myneni et al.* [2007], who interpreted the increased NIR *BRF* as more leaf area during the dry season and vice versa.

5. Discussion

[44] The dry season NIR reflectance (*BRF*) increase of 0.06 units, or about 23% (Figure 1), translates to a 16% increment in EVI (Figure 2), which is primarily sensitive to NIR (cf. Section 3.3), and this sensitivity increases with the magnitude of NIR reflectance (Figure 3). This change in EVI cannot be unambiguously interpreted because the exact property of the vegetation that this index measures is unknown. Another widely used index, the Normalized Difference Vegetation Index (NDVI), on the other hand, increases by only a small amount (4–5%) for the same increase in NIR reflectance (cf. Section 3.3), because its formulation is such that it dampens NIR reflectance changes and is independent of the magnitude of NIR reflectance (Figure 3). This NDVI change in absolute units is only 0.04, which is insignificant relative to the annual mean NDVI value of about 0.85 (Figure 2); this behavior is known as saturation in dense vegetation canopies, such as the Amazon forests. This rather small increase in NDVI, compared to a much larger increase in EVI, for the same change in canopy spectral reflectances further highlights the limitations of using vegetation indices for remote sensing of vegetation (as in work by *Huete et al.* [2006], *Xiao et al.* [2006], and *Brando et al.* [2010]).

[45] The MODIS LAI algorithm converts surface red and NIR reflectances and their overall uncertainties to most probable values of LAI [*Knyazikhin et al.*, 1998]. Uncertainties in surface reflectances include both observation and model uncertainties [*Wang et al.*, 2001]. The latter account for possible deviations of simulated reflectances from prescribed values in the look-up table due to variations in leaf optical properties. Thus, the algorithm converts surface spectral reflectances into LAI under the assumption that both leaf optical properties and LAI can vary (i.e., the impact function $k(\omega)$ is strictly positive, Section 3.4). Therefore, the algorithm is capable of detecting changes in leaf area. The MODIS algorithm reports approximately 18% increase in LAI (Figure 2) given the observed increase in NIR reflectance (Figure 1) during the dry season and a similar decrease in LAI during the wet season.

[46] New and mature leaves have leaf albedos (leaf reflectance plus transmittance) at NIR wavelengths that are 2–10% higher than those of older leaves due to aging and epiphyll cover [*Roberts et al.*, 1998; *Toomey et al.*, 2009]. The observed changes in NIR reflectance of Amazon forests (Figure 1) could be due to similar, but small, changes in NIR leaf albedos only, from exchanging older with newer leaves, with total leaf area unchanged, as argued by *Doughty and Goulden* [2008] and *Asner and Alencar* [2010] and confirmed by our analysis in Section 4.2.2. However, this ignores accumulating evidence from ground-based studies of higher leaf area in the dry season relative to the wet season, seasonal changes in litterfall and does not satisfactorily explain why NIR reflectance of these forests decreases in the following wet season. A more convincing explanation for the observed increase in NIR reflectance during the dry season and decrease during the wet season is one that invokes changes in both leaf area and leaf optical properties (Section 4.2.3). Such an argument is consistent with known phenological behavior of tropical forests (see the Introduction by *Myneni et al.* [2007]), ground-based reports of changes in leaf area [*Asner et al.*, 2004; *Carswell et al.*, 2002; *Pinto-Junior et al.*, 2010; *Malhado et al.*, 2009; *Negrón Juárez et al.*, 2009; *Doughty and Goulden*, 2008], litterfall [*Xiao et al.*, 2005; *Chave et al.*, 2010], leaf optical properties [*Roberts et al.*, 1998; *Toomey et al.*, 2009] and fluxes of evapotranspiration [*Juárez et al.*, 2007, 2008] and reconciles the various seemingly divergent views.

[47] A different line of reasoning on the cause of the dry season increase in NIR reflectance has been presented in a recent study by *Galvão et al.* [2011] using MODIS and hyperspectral (Hyperion and Hymap) data from a forest-savanna transitional site in Mato Grasso. The authors suggest that the dry season increase in NIR reflectance is caused by decreasing shade fraction resulting from large changes ($\sim$20°) in solar zenith angle (SZA), which in turn drives increase in EVI and MODIS LAI, given no observable changes in field-measured leaf area. While this study has correctly interpreted the increase in EVI arising from its dependence on NIR reflectance, the interpretation is based on correlation between the two rather than a thorough theoretical analysis presented here (cf. Section 3.3, Figure 3). The large SZA changes could be very specific to their study site because we have found significantly smaller changes in average SZA over Amazon forests (5°–6°, cf. Section 3.4.2). The suggestion that MODIS LAI changes are not representative of actual changes in leaf area is without basis because the MODIS LAI algorithm explicitly accounts for changes in SZA [*Knyazikhin et al.*, 1998] so as to preclude spurious LAI changes. Moreover, a large body of literature presents evidence of dry season leaf area increase [*Asner et al.*, 2004; *Carswell et al.*, 2002; *Pinto-Junior et al.*, 2010; *Malhado et al.*, 2009; *Negrón Juárez et al.*, 2009; *Doughty and Goulden*, 2008]. In addition, *Galvão et al.* [2011] did not examine the influence of leaf flush—leaf spectral changes—on NIR reflectance changes, which is presented here. All of these suggest that the results of *Galvão et al.* [2011] could be specific to their field site, as noted by the authors themselves, and may not be relevant to the vast expanse of Amazonian forests, the focus of our study.

[48] We have shown that the observed seasonal changes in NIR reflectance of Amazon forests are unlikely to be caused by changes in leaf area alone, but could, more plausibly, result from changes in both leaf area and leaf optical properties; however, our analysis is restricted to leaf optical property changes owing to leaf aging and epiphyll cover, given the paucity of literature on the sources of leaf optical property changes. The presence of a film of water on leaf surfaces, for instance due to a rainfall event, would tend to decrease greenness estimates because water reflects strongly

in red (blue) relative to NIR, an effect which is similar to the presence of residual atmospheric influences in the surface reflectances (cf. Figure S1). The use of VI error budget [from *Vermote and Kotchenova*, 2008] as an additional constraint on valid greenness increase in the dry season (cf. Figure 6 caption) would eliminate data showing such an effect. Among other possible causes of changes in leaf optical properties are leaf water content changes, dust coatings and coating with soot and carbonaceous particles emanating from biomass burning which is prevalent during the dry season. Thus, there is a need to explore these different mechanisms of leaf optical property variations. Finally, future research should also focus on spatial patterns of the causes (leaf area and leaf optical properties) of seasonal NIR reflectance variations of Amazonian forests.

[49] **Acknowledgment.** This work was supported by the NASA Earth Science Enterprise.

References

Aragao, L., Y. E. Shimabukuro, F. D. B. Espirito-Santo, and M. Williams (2005), Spatial validation of the collection 4 MODIS LAI product in Eastern Amazonia, *IEEE Trans. Geosci. Remote Sens.*, *43*(11), 2526–2534, doi:10.1109/TGRS.2005.856632.

Asner, G. P., and A. Alencar (2010), Drought impacts on the Amazon forest: The remote sensing perspective, *New Phytol.*, *187*(3), 569–578, doi:10.1111/j.1469-8137.2010.03310.x.

Asner, G. P., A. R. Townsend, and B. H. Braswell (2000), Satellite observation of El Niño effects on Amazon forest phenology and productivity, *Geophys. Res. Lett.*, *27*(7), 981–984, doi:10.1029/1999GL011113.

Asner, G. P., D. Nepstad, G. Cardinot, and D. Ray (2004), Drought stress and carbon uptake in an Amazon forest measured with spaceborne imaging spectroscopy, *Proc. Natl. Acad. Sci. U. S. A.*, *101*(16), 6039–6044, doi:10.1073/pnas.0400168101.

Brando, P. M., S. J. Goetz, A. Baccini, D. C. Nepstad, P. S. A. Beck, and M. C. Christman (2010), Seasonal and interannual variability of climate and vegetation indices across the Amazon, *Proc. Natl. Acad. Sci. U. S. A.*, *107*(33), 14,685–14,690, doi:10.1073/pnas.0908741107.

Carswell, F. E., et al. (2002), Seasonality in CO_2 and H_2O flux at an eastern Amazonian rain forest, *J. Geophys. Res.*, *107*(D20), 8076, doi:10.1029/2000JD000284.

Chave, J., et al. (2010), Regional and seasonal patterns of litterfall in tropical South America, *Biogeosciences*, *7*, 43–55, doi:10.5194/bg-7-43-2010.

Dessay, N., H. Laurent, L. A. T. Machado, Y. E. Shimabukuro, G. T. Batista, A. Diedhiou, and J. Ronchail (2004), Comparative study of the 1982–1983 and 1997–1998 El Niño events over different types of vegetation in South America, *Int. J. Remote Sens.*, *25*(20), 4063–4077, doi:10.1080/0143116031000101594.

Dickinson, R. E. (1983), Land surface processes and climate-surface albedos and energy balance, *Adv. Geophys.*, *25*, 305–353, doi:10.1016/S0065-2687(08)60176-4.

Doughty, C. E., and M. L. Goulden (2008), Seasonal patterns of tropical forest leaf area index and CO_2 exchange, *J. Geophys. Res.*, *113*, G00B06, doi:10.1029/2007JG000590.

Ferreira, L. G., and A. R. Huete (2004), Assessing the seasonal dynamics of the Brazilian Cerrado vegetation through the use of spectral vegetation indices, *Int. J. Remote Sens.*, *25*(10), 1837–1860, doi:10.1080/0143116031000101530.

Friedl, M. A., D. Sulla-Menashe, B. Tan, A. Schneider, N. Ramankutty, A. Sibley, and X. M. Huang (2010), MODIS Collection 5 global land cover: Algorithm refinements and characterization of new datasets, *Remote Sens. Environ.*, *114*(1), 168–182, doi:10.1016/j.rse.2009.08.016.

Fu, R., and W. Li (2004), The influence of land-surface on transition from dry to wet season in Amazonia, *Theor. Appl. Climatol.*, *78*, 97–110, doi:10.1007/s00704-004-0046-7.

Galvão, L. S., et al. (2011), On intra-annual EVI variability in the dry season of tropical forest: A case study with MODIS and hyperspectral data, *Remote Sens. Environ.*, *115*, 2350–2359, doi:10.1016/j.rse.2011.04.035.

Graham, E. A., S. S. Mulkey, K. Kitajima, N. G. Phillips, and S. J. Wright (2003), Cloud cover limits productivity in a tropical rain forest tree during La Nina, *Proc. Natl. Acad. Sci. U. S. A.*, *100*, 572–576, doi:10.1073/pnas.0133045100.

Huang, D., Y. Knyazikhin, W. Wang, D. W. Deering, P. Stenberg, N. Shabanov, B. Tan, and R. B. Myneni (2008), Stochastic transport theory for investigating the three-dimensional canopy structure from space measurements, *Remote Sens. Environ.*, *112*(1), 35–50, doi:10.1016/j.rse.2006.05.026.

Huete, A., K. Didan, T. Miura, E. P. Rodriguez, X. Gao, and L. G. Ferreira (2002), Overview of the radiometric and biophysical performance of the MODIS vegetation indices, *Remote Sens. Environ.*, *83*(1–2), 195–213, doi:10.1016/S0034-4257(02)00096-2.

Huete, A. R., K. Didan, Y. E. Shimabukuro, P. Ratana, S. R. Saleska, L. R. Hutyra, W. Z. Yang, R. R. Nemani, and R. Myneni (2006), Amazon rainforests green-up with sunlight in dry season, *Geophys. Res. Lett.*, *33*, L06405, doi:10.1029/2005GL025583.

Juárez, R. I. N., M. G. Hodnett, R. Fu, M. L. Goulden, and C. von Randow (2007), Control of dry season evapotranspiration over Amazonian forest as inferred from observations at a southern Amazon forest site, *J. Clim.*, *20*, 2827–2839, doi:10.1175/JCLI4184.1.

Juárez, R. I. N., et al. (2008), An empirical approach to retrieving monthly evapotranspiration over Amazonia, *Int. J. Remote Sens.*, *29*(24), 7045–7063, doi:10.1080/01431160802226026.

Knyazikhin, Y., J. V. Martonchik, R. B. Myneni, D. J. Diner, and S. W. Running (1998), Synergistic algorithm for estimating vegetation canopy leaf area index and fraction of absorbed photosynthetically active radiation from MODIS and MISR data, *J. Geophys. Res.*, *103*(D24), 32,257–32,275, doi:10.1029/98JD02462.

Knyazikhin, Y., L. Xu, M. A. Schull, R. B. Myneni, and A. Samanta (2010), Canopy spectral invariants. Part 1: A new concept in remote sensing of vegetation, *J. Quant. Spectrosc. Radiat. Transfer*, *112*, 727–735, doi:10.1016/j.jqsrt.2010.06.014.

Li, W., and R. Fu (2004), Transition of the large-scale atmospheric and land surface conditions from the dry to the wet season over Amazonia as diagnosed by the ECMWF Reanalysis, *J. Clim.*, *17*, 2637–2651, doi:10.1175/1520-0442(2004)017<2637:TOTLAA>2.0.CO;2.

Malhado, A. C. M., M. H. Costa, F. Z. de Lima, K. C. Portilho, and D. N. Figueiredo (2009), Seasonal leaf dynamics in an Amazonian tropical forest, *For. Ecol. Manage.*, *258*(7), 1161–1165, doi:10.1016/j.foreco.2009.06.002.

Myneni, R. B., F. G. Hall, P. J. Sellers, and A. L. Marshak (1995), The interpretation of spectral vegetation indexes, *IEEE Trans. Geosci. Remote Sens.*, *33*(2), 481–486, doi:10.1109/36.377948.

Myneni, R. B., et al. (2007), Large seasonal swings in leaf area of Amazon rainforests, *Proc. Natl. Acad. Sci. U. S. A.*, *104*(12), 4820–4823, doi:10.1073/pnas.0611338104.

NASA Land Processes Data Active Archive Center (LP DAAC) (2009), Land Cover Type Yearly L3 Global 1 km SIN Grid (MOD12Q1), https://lpdaac.usgs.gov/lpdaac/products/modis_products_table/land_cover/yearly_l3_global_1km2/mod12q1, USGS EROS Data Cent., Sioux Falls, S. D.

NASA Land Processes Data Active Archive Center (LP DAAC) (2010a), Vegetation Indices 16-Day L3 Global 1 km (MOD13A2), https://lpdaac.usgs.gov/lpdaac/content/view/full/6648, USGS EROS Data Cent., Sioux Falls, S. D.

NASA Land Processes Data Active Archive Center (LP DAAC) (2010b), Vegetation Indices 16-Day L3 Global 0.05deg CMG (MOD13C1), https://lpdaac.usgs.gov/content/view/full/6661, USGS EROS Data Cent., Sioux Falls, S. D.

NASA Land Processes Data Active Archive Center (LP DAAC) (2010c), Leaf Area Index–Fraction of Photosynthetically Active Radiation 8-Day L4 Global 1 km (MOD15A2), https://lpdaac.usgs.gov/lpdaac/products/modis_products_table/leaf_area_index_fraction_of_photosynthetically_active_radiation/8_day_l4_global_1km/mod15a2, USGS EROS Data Cent., Sioux Falls, S. D.

Negrón Juárez, R. I., H. R. da Rocha, A. Figueira, M. L. Goulden, and S. D. Miller (2009), An improved estimate of leaf area index based on the histogram analysis of hemispherical photographs, *Agric. For. Meteorol.*, *149*(6–7), 920–928, doi:10.1016/j.agrformet.2008.11.012.

Nemani, R. R., C. D. Keeling, H. Hashimoto, W. M. Jolly, S. C. Piper, C. J. Tucker, R. B. Myneni, and S. W. Running (2003), Climate-driven increases in global terrestrial net primary production from 1982 to 1999, *Science*, *300*(5625), 1560–1563, doi:10.1126/science.1082750.

Nepstad, D. C., C. R. Decarvalho, E. A. Davidson, P. H. Jipp, P. A. Lefebvre, G. H. Negreiros, E. D. Dasilva, T. A. Stone, S. E. Trumbore, and S. Vieira (1994), The role of deep roots in the hydrological and carbon cycles of Amazonian forests and pastures, *Nature*, *372*(6507), 666–669, doi:10.1038/372666a0.

Pinto-Junior, Q. B., L. Sanches, F. D. Lobo, A. A. Brandao, and J. S. Nogueira (2010), Leaf area index of a tropical semi-deciduous forest of the southern Amazon Basin, *Int. J. Biometeorol.*, *55*, 109–118, doi:10.1007/s00484-010-0317-1.

Rahman, A. F., D. A. Sims, V. D. Cordova, and B. Z. El-Masri (2005), Potential of MODIS EVI and surface temperature for directly estimating

per-pixel ecosystem C fluxes, *Geophys. Res. Lett.*, *32*, L19404, doi:10.1029/2005GL024127.

Rautiainen, M., M. Mottus, and P. Stenberg (2009), On the relationship of canopy LAI and photon recollision probability in boreal forests, *Remote Sens. Environ.*, *113*(2), 458–461, doi:10.1016/j.rse.2008.10.014.

Reich, P. B., C. Uhl, M. B. Walters, L. Prugh, and D. S. Ellsworth (2004), Leaf demography and phenology in Amazonian rain forest: A census of 40,000 leaves of 23 tree species, *Ecol. Monogr.*, *74*(1), 3–23, doi:10.1890/02-4047.

Roberts, D. A., B. W. Nelson, J. B. Adams, and F. Palmer (1998), Spectral changes with leaf aging in Amazon Caatinga, *Trees (Heidelberg, Ger.)*, *12*, 315–325, doi:10.1007/s004680050157.

Ross, J. (Ed.) (1981), *The Radiation Regime and Architecture of Plant Stands*, Dr. W. Junk, Boston, Mass.

Saleska, S. R., et al. (2003), Carbon in Amazon forests: Unexpected seasonal fluxes and disturbance-induced losses, *Science*, *302*(5650), 1554–1557, doi:10.1126/science.1091165.

Samanta, A., S. Ganguly, H. Hashimoto, S. Devadiga, E. Vermote, Y. Knyazikhin, R. R. Nemani, and R. B. Myneni (2010), Amazon forests did not green-up during the 2005 drought, *Geophys. Res. Lett.*, *37*, L05401, doi:10.1029/2009GL042154.

Samanta, A., S. Ganguly, and R. B. Myneni (2011a), MODIS Enhanced Vegetation Index data do not show greening of Amazon forests during the 2005 drought, *New Phytol.*, *189*(1), 11–15, doi:10.1111/j.1469-8137.2010.03516.x.

Samanta, A., M. H. Costa, E. L. Nunes, S. L. Vieira, L. Xu, and R. Myneni (2011b), Comment on "Drought-induced reduction in global terrestrial net primary production from 2000 through 2009", *Science*, *333*(6046), 1093, doi:10.1126/science.1199048.

Schull, M. A., et al. (2010), Canopy spectral invariants, Part 2: Application to classification of forest types from hyperspectral data, *J. Quant. Spectrosc. Radiat. Transfer*, *112*, 736–750, doi:10.1016/j.jqsrt.2010.06.004.

Schuur, E. A. G. (2003), Net primary productivity and global climate revisited: The sensitivity of tropical forest growth to precipitation, *Ecology*, *84*, 1165–1170, doi:10.1890/0012-9658(2003)084[1165:PAGCRT]2.0.CO;2.

Shabanov, N. V., et al. (2005), Analysis and optimization of the MODIS leaf area index algorithm retrievals over broadleaf forests, *IEEE Trans. Geosci. Remote Sens.*, *43*(8), 1855–1865, doi:10.1109/TGRS.2005.852477.

Sims, D. A., et al. (2008), A new model of gross primary productivity for North American ecosystems based solely on the enhanced vegetation index and land surface temperature from MODIS, *Remote Sens. Environ.*, *112*(4), 1633–1646, doi:10.1016/j.rse.2007.08.004.

Smolander, S., and P. Stenberg (2005), Simple parameterizations of the radiation budget of uniform broadleaved and coniferous canopies, *Remote Sens. Environ.*, *94*(3), 355–363, doi:10.1016/j.rse.2004.10.010.

Stenberg, P. (2007), Simple analytical formula for calculating average photon recollision probability in vegetation canopies, *Remote Sens. Environ.*, *109*(2), 221–224, doi:10.1016/j.rse.2006.12.014.

Toomey, M., D. Roberts, and B. Nelson (2009), The influence of epiphylls on remote sensing of humid forests, *Remote Sens. Environ.*, *113*(8), 1787–1798, doi:10.1016/j.rse.2009.04.002.

Vermote, E. F., and S. Kotchenova (2008), Atmospheric correction for the monitoring of land surfaces, *J. Geophys. Res.*, *113*, D23S90, doi:10.1029/2007JD009662.

Wang, Y. J., Y. H. Tian, Y. Zhang, N. El-Saleous, Y. Knyazikhin, E. Vermote, and R. B. Myneni (2001), Investigation of product accuracy as a function of input and model uncertainties: Case study with SeaWiFS and MODIS LAI/FPAR algorithm, *Remote Sens. Environ.*, *78*(3), 299–313, doi:10.1016/S0034-4257(01)00225-5.

Wright, S. J., and C. P. van Schaik (1994), Light and the phenology of tropical trees, *Am. Nat.*, *143*(1), 192–199, doi:10.1086/285600.

Würth, M. K. R., S. Peláez-Riedl, S. J. Wright, and C. Körner (2005), Non-structural carbohydrate pools in a tropical forest, *Oecologia*, *143*, 11–24, doi:10.1007/s00442-004-1773-2.

Xiao, X., et al. (2005), Satellite-based modeling of gross primary production in a seasonally moist tropical evergreen forest, *Remote Sens. Environ.*, *94*, 105–122, doi:10.1016/j.rse.2004.08.015.

Xiao, X. M., S. Hagen, Q. Y. Zhang, M. Keller, and B. Moore (2006), Detecting leaf phenology of seasonally moist tropical forests in South America with multi-temporal MODIS images, *Remote Sens. Environ.*, *103*(4), 465–473, doi:10.1016/j.rse.2006.04.013.

Xu, L., A. Samanta, M. H. Costa, S. Ganguly, R. R. Nemani, and R. B. Myneni (2011), Widespread decline in greenness of Amazonian vegetation due to the 2010 drought, *Geophys. Res. Lett.*, *38*, L07402, doi:10.1029/2011GL046824.

Yang, W., N. V. Shabanov, D. Huang, W. Wang, R. E. Dickinson, R. R. Nemani, Y. Knyazikhin, and R. B. Myneni (2006), Analysis of leaf area index products from combination of MODIS Terra and Aqua data, *Remote Sens. Environ.*, *104*(3), 297–312, doi:10.1016/j.rse.2006.04.016.

M. H. Costa, Federal University of Viçosa, Av. P. H. Rolfs, s/n, Viçosa, MG CEP 36570-000, Brazil.

R. E. Dickinson and R. Fu, Department of Geological Sciences, University of Texas at Austin, Austin, TX 78712, USA.

Y. Knyazikhin, R. B. Myneni, and L. Xu, Department of Geography and Environment, Boston University, Boston, MA 02215, USA.

R. R. Nemani, Biospheric Sciences Branch, NASA AMES Research Center, Moffett Field, CA 94035, USA.

S. S. Saatchi, Jet Propulsion Laboratory, California Institute of Technology, Pasadena, CA 91109, USA.

A. Samanta, Atmospheric and Environmental Research Inc., Lexington, MA 02421, USA. (arindam.sam@gmail.com)

Environmental Research Letters

LETTER

Sunlight mediated seasonality in canopy structure and photosynthetic activity of Amazonian rainforests

Jian Bi[1,20], **Yuri Knyazikhin**[1,20], **Sungho Choi**[1], **Taejin Park**[1], **Jonathan Barichivich**[2], **Philippe Ciais**[3], **Rong Fu**[4], **Sangram Ganguly**[5], **Forrest Hall**[6], **Thomas Hilker**[7], **Alfredo Huete**[8], **Matthew Jones**[9], **John Kimball**[9], **Alexei I Lyapustin**[10], **Matti Mõttus**[11], **Ramakrishna R Nemani**[12], **Shilong Piao**[13,14], **Benjamin Poulter**[15], **Scott R Saleska**[16], **Sassan S Saatchi**[17,18], **Liang Xu**[17], **Liming Zhou**[19] **and Ranga B Myneni**[1]

[1] Department of Earth and Environment, Boston University, Boston, MA 02215, USA
[2] Climatic Research Unit, School of Environmental Sciences, University of East Anglia, Norwich NR4 7TJ, UK
[3] Laboratoire des Sciences du Climat et de l'Environnement, IPSL-LSCE, CEA-CNRS-UVSQ, 91191 Gif sur Yvette Cedex, France
[4] Department of Geological Sciences, The University of Texas at Austin, Austin, TX 78712, USA
[5] Bay Area Environmental Research Institute, NASA Ames Research Center, Moffett Field, CA 94035, USA
[6] Biospheric Sciences Laboratory, NASA Goddard Space Flight Center, Greenbelt, MD 20771, USA
[7] College of Forestry, Oregon State University, Corvallis, OR 97331, USA
[8] Plant Functional Biology and Climate Change Cluster, University of Technology Sydney, New South Wales 2007, Australia
[9] Numerical Terradynamic Simulation Group, The University of Montana, Missoula, MT 59812, USA
[10] Climate and Radiation Laboratory, NASA Goddard Space Flight Center, Greenbelt, MD 20771, USA
[11] Department of Geosciences and Geography, University of Helsinki, FI-00014, Helsinki, Finland
[12] NASA Advanced Supercomputing Division, Ames Research Center, Moffett Field, California 94035, USA
[13] Department of Ecology, Peking University, Beijing 100871, People's Republic of China
[14] Institute of Tibetan Plateau Research, Chinese Academy of Sciences, Beijing 100085, People's Republic of China
[15] Department of Ecology, Montana State University, Bozeman, MT 59717, USA
[16] Department of Ecology and Evolutionary Biology, University of Arizona, Tucson, AZ 85721, USA
[17] Institute of the Environment and Sustainability, University of California, Los Angeles, CA 90095, USA
[18] Radar Science and Engineering section, Jet Propulsion Laboratory, California Institute of Technology, Pasadena, CA 91109, USA
[19] Department of Atmospheric and Environmental Sciences, University at Albany, State University of New York, Albany, New York 12222, USA
[20] These authors contributed equally to this work.

E-mail: jknjazi@bu.edu

OPEN ACCESS

RECEIVED
26 February 2015

REVISED
28 May 2015

ACCEPTED FOR PUBLICATION
1 June 2015

PUBLISHED
16 June 2015

Content from this work may be used under the terms of the Creative Commons Attribution 3.0 licence.

Any further distribution of this work must maintain attribution to the author(s) and the title of the work, journal citation and DOI.

Keywords: Amazonian rainforests, seasonality, remote sensing, MISR, MODIS

Supplementary material for this article is available online

Abstract

Resolving the debate surrounding the nature and controls of seasonal variation in the structure and metabolism of Amazonian rainforests is critical to understanding their response to climate change. *In situ* studies have observed higher photosynthetic and evapotranspiration rates, increased litterfall and leaf flushing during the Sunlight-rich dry season. Satellite data also indicated higher greenness level, a proven surrogate of photosynthetic carbon fixation, and leaf area during the dry season relative to the wet season. Some recent reports suggest that rainforests display no seasonal variations and the previous results were satellite measurement artefacts. Therefore, here we re-examine several years of data from three sensors on two satellites under a range of sun positions and satellite measurement geometries and document robust evidence for a seasonal cycle in structure and greenness of wet equatorial Amazonian rainforests. This seasonal cycle is concordant with independent observations of solar radiation. We attribute alternative conclusions to an incomplete study of the seasonal cycle, i.e. the dry season only, and to prognostications based on a biased radiative transfer model. Consequently, evidence of dry season greening in geometry corrected satellite data was ignored and the absence of evidence for seasonal variation in lidar data due to noisy and saturated signals was misinterpreted as evidence of the absence of changes during the dry season. Our results, grounded in the physics of radiative transfer, buttress previous reports of dry season increases in leaf flushing, litterfall, photosynthesis and evapotranspiration in well-hydrated Amazonian rainforests.

© 2015 IOP Publishing Ltd

1. Introduction

Understanding the seasonal variation in functioning of rainforests and its controls are requisite for understanding how rainforests will respond to climate change. *In situ* studies report counter-intuitive seasonal variation in wet equatorial Amazonian rainforests —higher photosynthetic and evapotranspiration rates and increased litterfall and leaf flushing during the Sunlight-rich dry season (Saleska *et al* 2003, da Rocha *et al* 2004, Goulden *et al* 2004, Rice *et al* 2004, Hasler and Avissar 2007, Hutyra *et al* 2007, Negrón Juárez *et al* 2009, Costa *et al* 2010, Jones *et al* 2014). Water limitation during the dry season is alleviated in these forests through deep roots and hydraulic redistribution (Nepstad *et al* 1994, Oliveira *et al* 2005). Satellite data, which cover a large area and span a long time period, support findings of *in situ* studies—higher radiometric greenness level and green leaf area during the dry season compared to the wet season (Xiao *et al* 2005, Huete *et al* 2006, Myneni *et al* 2007, Samanta *et al* 2012, Hilker *et al* 2014, Jones *et al* 2014, Maeda *et al* 2014). This convergent view of seasonality, parsed from several studies, shows how sunlight interacts with adaptive mechanisms to result in higher rates of leaf flushing, litterfall, photosynthesis and evapotranspiration in tropical forests if water limitation is absent (Wright and Van Schaik 1994, Restrepo-Coupe *et al* 2013, Borchert *et al* 2015, Guan *et al* 2015).

This community-consensual view was questioned in recent studies (Galvão *et al* 2011, Morton *et al* 2014). The studies claim that the dry season greening inferred from passive remote sensing data resulted from an artificial increase in forest canopy reflectance at near-infrared (NIR) wavelengths caused by variations in sun-satellite sensor geometry. Their analyses of satellite-borne lidar data suggested that these forests exhibited no seasonal variations in canopy structure or leaf area. Relying on model simulations to guide and imbue a physical meaning to the satellite data analysis, the studies conclude that Amazon rainforests maintain consistent structure and greenness during the dry season.

These contradictory results justify a re-examination of the same satellite data with the goal of assessing seasonality in wet equatorial Amazonian rainforests. In addition to data from NASA's Moderate Resolution Imaging Spectroradiometer (MODIS) on the Terra platform and the Geoscience Laser Altimeter System (GLAS) instrument onboard the Ice, Cloud and land Elevation Satellite (ICESat) used in (Morton *et al* 2014), we also include data from the MODIS instrument on Aqua and Multiangle Imaging Spectroradiometer (MISR) on the Terra satellite. The MISR sensor views the Earth's surface with nine cameras simultaneously, as opposed to the two MODIS sensors, which are capable of only one view each. This feature enables the rigorous use of the theory of radiative transfer in vegetation canopies—the fundamental theory that explains from first principles the mechanisms underlying the signals generated by the canopy and measured by a remote sensor (Knyazikhin *et al* 2005).

This study is focused on terra firme rainforests in central Amazonia that are relatively undisturbed by human activities (supplementary data and methods section 1, figure S1). The period June to May is treated as one seasonal cycle as per convention (Huete *et al* 2006, Morton *et al* 2014). It consists of a short dry season, June to October, and a long wet season thereafter (supplementary data and methods section 1). The following analysis of satellite borne sensor data addresses the question at the center of current debate —did previous studies (Xiao *et al* 2005, Huete *et al* 2006, Myneni *et al* 2007, Brando *et al* 2010, Samanta *et al* 2012) misinterpret changes in near-infrared (NIR) reflectance caused by seasonal changes in sun-satellite sensor geometry (figures S2 and S3) as seasonal variations in rainforest canopy structure and greenness (Galvão *et al* 2011, Morton *et al* 2014)?

2. Data and methods

A detailed description of methods and data used is given in the supplementary information available at stacks.iop.org/ERL/10/064014/mmedia. A brief summary is provided here. The study region and the various data analysed in this study are detailed in the supplementary data and methods section 1–2. The sun-sensor geometry relevant to the discussion in this article is presented in the supplementary data and methods section 3. The theory of remote measurements and evaluation of NIR reflectance angular signatures (figure 3) and their interpretation is described in the supplementary data and methods section 4. A critical look at Morton *et al* 2014 analyses of MODIS and GLAS data is presented in the supplementary discussion. Abbreviations and symbols are listed in supplementary table S5.

3. Results and discussioin

3.1. Leaf area index seasonality

The seasonal cycle of green leaf area inferred from satellite data (figure 1(a)) exhibits rising values during the dry season (June to October), high values during the early part of the wet season (November to February) and decreasing values thereafter (March to May). This seasonal variation of about 20% is imposed on a base value of Leaf Area Index (LAI, one-sided green leaf area per unit ground area) of about 5.75, is greater than the uncertainty of the LAI product (0.66 LAI, Yang *et al* 2006) and is observed in nearly 70% of the rainforests in the study domain (figure S4(a)); the rest lacked valid data. Is this seasonal variation real or a misinterpretation of changes in satellite-sensor measurements caused by seasonal changes in sun position

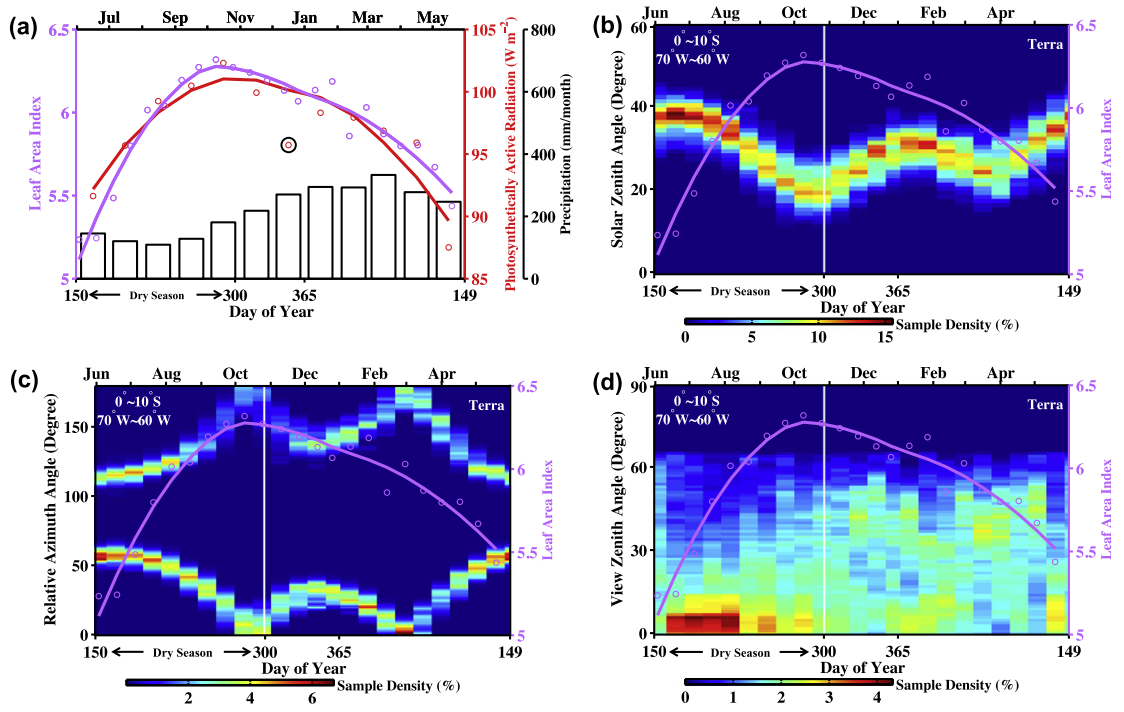

Figure 1. Seasonal variations in green leaf area of central Amazonian rainforests. (a) Seasonal cycles of Terra MODIS leaf area index (LAI), at-surface photosynthetically active radiation (PAR) from CERES, and TRMM precipitation. The PAR polynomial regression curve excludes the circled data point. The seasonal profiles represent average values over pixels that exhibited dry season greening in at least 4 out of 7 seasonal cycles analyzed (63% of all forest pixels). (b)–(d) Seasonal cycle of LAI, as in panel (a), contrasted against seasonal variations in (b) solar zenith angle, (c) sensor view relative azimuth angle and (d) view zenith angle.

in the sky and the manner in which the sensor measures reflected radiation ('sun-sensor geometry')? The answer requires an understanding of how this geometry changes during the seasonal cycle, which is described in the supplementary data and methods section 3.

The seasonal cycle of leaf area in figure 1(a) cannot be an artefact of seasonal changes in sun-sensor geometry because the algorithm with which leaf area is derived explicitly accounts for geometry changes, i.e. the algorithm is capable of differentiating between changes in measurements caused by leaf area changes and those caused by geometry changes (Knyazikhin *et al* 1999, Knyazikhin *et al* 1998). This is also evident from the fact that the seasonal cycle of leaf area does not track the seasonal course of either the Sun position in the sky (figure 1(b)) or the MODIS sensor sampling (figures 1(c) and (d)). Instead, it tracks independently obtained observations of seasonal variation in sunlight (figure 1(a)). This behavior is consistent with the idea that sunlight acts as a proximate cue for leaf production in moist tropical forests if water limitation is absent (Wright and Van Schaik 1994, Borchert *et al* 2015, Guan *et al* 2015). Thus, relatively high sunlight levels from absence of clouds during the dry season cause leaf area to increase, which in turn generates higher rates of photosynthesis (Saleska *et al* 2003, Da Rocha *et al* 2004, Restrepo-Coupe *et al* 2013, Gatti *et al* 2014). But, photosynthesis becomes decoupled from sunlight during the early to middle part of the wet season. This results in increasing rates of photosynthesis, which are possibly sustained by still sufficiently high levels of light and increasing leaf production (Restrepo-Coupe *et al* 2013). All three decrease rapidly thereafter. A bimodal seasonal cycle of LAI reported in one instance could be site-specific (figure 2 in Doughty and Goulden (2008)) as alternate *in situ* evidence does not exist (Restrepo-Coupe *et al* 2013, Xiao *et al* 2005, Asner *et al* 2000, Carswell *et al* 2002, Chave *et al* 2010, Malhado *et al* 2009, Negrón Juárez *et al* 2009).

3.2. Evidence for seasonality after sun-sensor geometry correction

The Enhanced Vegetation Index (EVI) is a proven proxy for the potential photosynthetic carbon fixation by vegetation (Xiao *et al* 2005, Huete *et al* 2006, Brando *et al* 2010). It is calculated from satellite-sensor measurements of reflected solar radiation at three different wavelength bands. These measurements depend on sun-sensor geometry, but this dependency can be eliminated by expressing the measurements in a fixed geometry (Morton *et al* 2014, Lyapustin *et al* 2012). The EVI calculated from MODIS sensor measurements in a fixed geometry, i.e. nadir viewing direction and 45° solar zenith angle, shows a distinct wet season decrease (figure 2(a)) and dry season increase (figure 2(b)). These changes are greater than a highly conservative estimate of the precision in 43% of the pixels during the wet season and 31% of the pixels

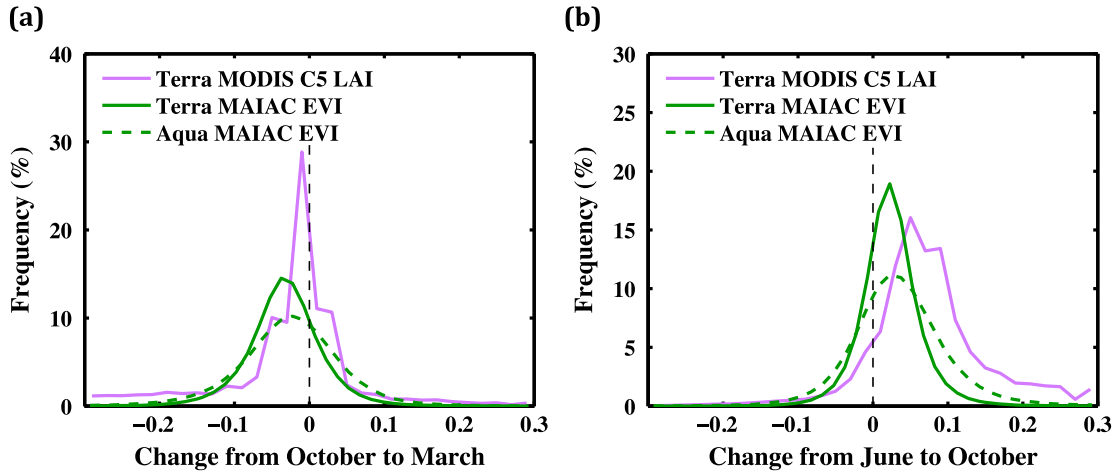

Figure 2. Wet and dry season changes in sun-sensor geometry corrected estimates of leaf area and greenness. Per-pixel changes in MODIS leaf area index (LAI) and MODIS MAIAC enhanced vegetation index (EVI) from (a) October to March and (b) June to October. LAI values are normalized by 10. The changes are calculated as the difference between the values in March and October, and October and June, respectively.

in the dry season. Here, the precision is estimated as the spatial standard deviation of the EVI data in the study domain. Analogous to EVI, pixel level estimates of green leaf area show a strong decrease in the wet season and increase during the dry season. The wet season decrease (figure 2(a)) suggests net leaf abscission, i.e. more older leaves dropped than those newly flushed, and the dry season increase indicates net leaf flushing (figure 2(b)), resulting in a sunlight mediated phenological behavior (Myneni *et al* 2007). The fact that both EVI and LAI show congruent changes during the seasonal cycle even though the Sun-sensor geometry effect is removed from measurements in different ways (Knyazikhin *et al* 1999, Knyazikhin *et al* 1998, Lyapustin *et al* 2012, Hilker *et al* 2014, Maeda *et al* 2014) is particularly noteworthy.

3.3. Evidence for seasonality from multiple sensors and geometries

Now we turn to satellite-sensor measurements of reflected solar radiation at the NIR wavelength band, which are at the heart of the controversy. These measurements are usually expressed as normalized quantities called reflectances (supplementary data and methods section 4.1–4.2). The geometric structure and radiation scattering properties of the rainforest canopy determine the magnitude and angular distribution of reflected radiation. The angular signatures of reflectance are therefore unique and rich sources of diagnostic information about rainforest canopies (Diner *et al* 1999). We first examine NIR angular signatures from the late dry season (October 15 to 30) and the middle part of the wet season (March 5 to 20). The Solar Zenith Angle (SZA) at the time when Terra (10:30 am) and Aqua (1:30 pm) satellites view the central Amazonian forests in March and October is between 20° and 30°. This variation minimally impacts the shape of angular signatures (supplementary data and methods section 4.4). MODIS and MISR sensors sample the rainforests very differently (figures S2(c)–(f); also see figure S1(c)). However, all the sensors record a distinct decrease in reflected NIR radiation in all view directions between October and March with no change in the overall shape of the angular signatures (figures 3(a) and (b)). Such a simple change in magnitude can only result from a change in canopy properties—this conclusion is based on the physics of how solar radiation interacts with foliage in vegetation canopies (supplementary data and methods section 4.3, figures S5(a) and (b)). The EVI, although evaluated from reflectances at NIR, red and blue wavelength bands, is tightly linked to NIR reflectance (Samanta *et al* 2012). Thus, the decrease in sun-sensor geometry corrected EVI (figure 2(a)) is in agreement with directly observed decreases in NIR angular signatures from October to March (figures 3(a) and (b)).

The wet season reduction in greenness is inconsistent with the hypothesis of invariant dry season greenness. Indeed the net loss of leaf area, without a corresponding net gain elsewhere during the seasonal cycle, will result in rainforests without leaves in a few years. If wet Amazonian forests somehow maintain consistent canopy structure and greenness during the dry season, then they must be either aseasonal or the entire seasonal cycle must be confined to the wet season, but this argument lacks empirical support. The question then arises whether variations in angular signatures of forest reflectance during the dry season support this inference?

Therefore, let us now consider NIR reflectances from early (25 June to 10 July) and the late dry season (15 October to 30 October) when both sun position in the sky and sensor sampling vary significantly (figures S2(a)–(d); also see figure S1(c)). MODIS and MISR measurements are made at significantly higher SZA in June (~35°–40°) compared to October (~20°–30°).

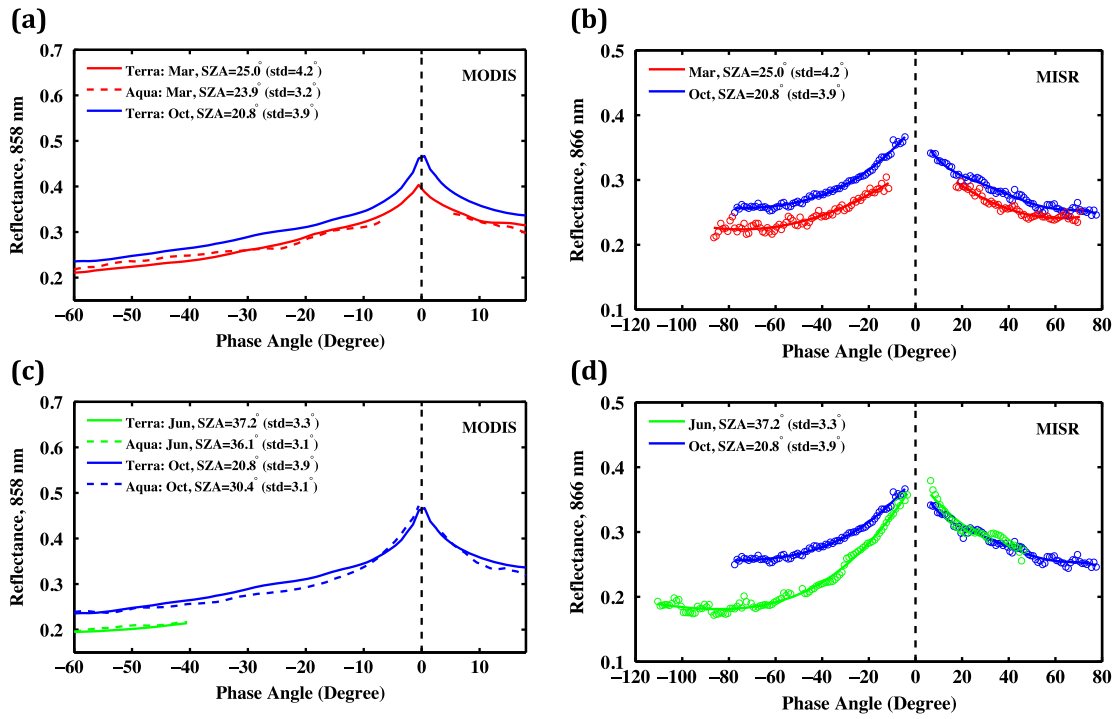

Figure 3. Seasonal changes in angular signatures of near-infrared (NIR) reflectance from three satellite borne sensors. Angular signatures of NIR reflectance in March (5 Mar to 20 Mar), June (25 Jun to 10 Jul) and October (15 Oct to 30 Oct). The Aqua MODIS signature for October is shown in panel (c) for clarity. The phase angle is the angle between the directions to the Sun and sensor (figure S1(c)).

The magnitude and shape of angular signatures are impacted when both canopy properties and SZA vary. However, a higher or equal reflectance at lower SZA relative to reflectance at higher SZA always indicates an increase in leaf area and foliage scattering properties according to the physics of radiation interaction in vegetation (supplementary data and methods section 4.4–4.5, figures S5(c)–(f)). This is observed clearly in MISR data (figure 3(d)) because this sensor views the Earth's surface with nine cameras simultaneously, as opposed to the two MODIS sensors (figure 3(c)), which are capable of only one view each (figure S3). Further, the juxtaposition of the two angular signatures in figure 3(d) is significantly different than that predicted by theory for the case of identical canopies (supplementary data and methods section 4.6). Thus, the NIR angular signatures in figure 3(d) indicate a change in vegetation structure (LAI) and greenness (EVI) during the dry season.

4. Conclusions

Satellite data indicate a distinct sunlight-mediated seasonality in leaf area and photosynthetic carbon fixation over unstressed rainforests in central Amazonia. This seasonal cycle is not an artefact of seasonal changes in sun position in the sky or how the satellite-sensor measures the reflected radiation field. The spatially expansive remote sensing data agree with available *in situ* data. A better understanding of how the rainforests will respond to climate change depends on future ground campaigns as satellite data can complement, but not substitute, field data.

Acknowledgments

This study was supported by NASA Earth Science Division.

Author contributions

J B, Y K, S C and T P performed the analyses. RBM wrote the initial draft. All authors contributed with ideas to the analyses and with writing the article. The authors declare no conflict of interest.

References

Asner G P, Townsend A R and Braswell B H 2000 Satellite observation of El Nino effects on Amazon forest phenology and productivity *Geophys. Res. Lett.* **27** 981–4

Brando P M, Goetz S J, Baccini A, Nepstad D C, Beck P S and Christman M C 2010 Seasonal and interannual variability of climate and vegetation indices across the Amazon *Proc. Natl Acad. Sci. USA* **107** 14685–90

Borchert R, Calle Z, Strahler A H, Baertschi A, Magill R E, Broadhead J S, Kamau J, Njoroge J and Muthuri C 2015 Insolation and photoperiodic control of tree development near the equator *New Phytol.* **205** 7–13

Carswell F *et al* 2002 Seasonality in CO2 and H2O flux at an eastern Amazonian rain forest *J. Geophys. Res. Atmos.* **107** LBA43–1

Chave J *et al* 2010 Regional and seasonal patterns of litterfall in tropical South America *Biogeosciences* **7** 43–55

Costa M H *et al* 2010 Atmospheric versus vegetation controls of Amazonian tropical rain forest evapotranspiration: are the

wet and seasonally dry rain forests any different? *J. Geophys. Res. Biogeosci.* **115** G04021

Da Rocha H R, Goulden M L, Miller S D, Menton M C, Pinto L D, De Freitas H C and Silva Figueira A M E 2004 Seasonality of water and heat fluxes over a tropical forest in eastern Amazonia *Ecol. Appl.* **14** S22–32

Diner D J, Asner G P, Davies R, Knyazikhin Y, Muller J P, Nolin A W, Pinty B, Schaaf C B and Stroeve J 1999 New directions in earth observing: scientific applications of multiangle remote sensing *Bull. Am. Meteorol. Soc.* **80** 2209–28

Doughty C E and Goulden M L 2008 Seasonal patterns of tropical forest leaf area index and CO_2 exchange *J. Geophys. Res. Biogeosci.* **113** G00B06

Galvão L S, Dos Santos J R, Roberts D A, Breunig F M, Toomey M and De Moura Y M 2011 On intra-annual EVI variability in the dry season of tropical forest: a case study with MODIS and hyperspectral data *Remote Sens. Environ.* **115** 2350–9

Gatti L *et al* 2014 Drought sensitivity of Amazonian carbon balance revealed by atmospheric measurements *Nature* **506** 76–80

Goulden M L, Miller S D, Da Rocha H R, Menton M C, De Freitas H C, Silva Figueira A M E and De Sousa C D 2004 Diel and seasonal patterns of tropical forest CO_2 exchange *Ecol. Appl.* **14** S42–54

Guan K *et al* 2015 Photosynthetic seasonality of global tropical forests constrained by hydroclimate *Nature Geosci.* **8** 284–9

Hasler N and Avissar R 2007 What controls evapotranspiration in the Amazon basin? *J. Hydrometeorol.* **8** 380–95

Hilker T *et al* 2014 Vegetation dynamics and rainfall sensitivity of the Amazon *Proc. Natl Acad. Sci. USA* **111** 16041–6

Huete A R *et al* 2006 Amazon rainforests green-up with sunlight in dry season *Geophys. Res. Lett.* **33** L06405

Hutyra L R *et al* 2007 Seasonal controls on the exchange of carbon and water in an Amazonian rain forest *J. Geophys. Res. Biogeosci.* **112** G03008

Jones M O, Kimball J S and Nemani R R 2014 Asynchronous Amazon forest canopy phenology indicates adaptation to both water and light availability *Environ. Res. Lett.* **9** 124021

Knyazikhin Y *et al* 1999 MODIS leaf area index (LAI) and fraction of photosynthetically active radiation absorbed by vegetation (FPAR) product (MOD15) *Algorithm Theoretical Basis Document* (https://lpdaac.usgs.gov/products/modis_products_table/mcd15a2)

Knyazikhin Y, Martonchik J, Myneni R, Diner D and Running S 1998 Synergistic algorithm for estimating vegetation canopy leaf area index and fraction of absorbed photosynthetically active radiation from MODIS and MISR data *J. Geophys. Res. Atmos.* **103** 32257–75

Knyazikhin Y, Marshak A and Myneni R B 2005 Three-dimensional radiative transfer in vegetation canopies and cloud-vegetation interaction *Three Dimensional Radiative Transfer in the Cloudy Atmosphere* ed A Marshak and A B Davis (Berlin, Heidelberg: Springer) pp 617–51

Lyapustin A I *et al* 2012 Multi-angle implementation of atmospheric correction for MODIS (MAIAC): 3. Atmospheric correction *Remote Sens. Environ.* **127** 385–93

Maeda E E, Heiskanen J, Aragão L E O C and Rinne J 2014 Can MODIS EVI monitor ecosystem productivity in the Amazon rainforest? *Geophys. Res. Lett.* **41** 7176–83

Malhado A, Costa M H, de Lima F Z, Portilho K C and Figueiredo D N 2009 Seasonal leaf dynamics in an Amazonian tropical forest *For. Ecol. Manage.* **258** 1161–5

Morton D C *et al* 2014 Amazon forests maintain consistent canopy structure and greenness during the dry season *Nature* **506** 221–4

Myneni R B *et al* 2007 Large seasonal swings in leaf area of Amazon rainforests *Proc. Natl Acad. Sci. USA* **104** 4820–3

Negrón Juárez R I, da Rocha H R, Goulden M L and Miller S D 2009 An improved estimate of leaf area index based on the histogram analysis of hemispherical photographs *Agric. For. Meteorol.* **149** 920–8

Nepstad D C *et al* 1994 The role of deep roots in the hydrological and carbon cycles of Amazonian forests and pastures *Nature* **372** 666–9

Oliveira R S, Dawson T E, Burgess S S and Nepstad D C 2005 Hydraulic redistribution in three Amazonian trees *Oecologia* **145** 354–63

Restrepo-Coupe N *et al* 2013 What drives the seasonality of photosynthesis across the Amazon basin? A cross-site analysis of eddy flux tower measurements from the Brasil flux network *Agric. For. Meteorol.* **182** 128–44

Rice A H *et al* 2004 Carbon balance and vegetation dynamics in an old-growth Amazonian forest *Ecol. Appl.* **14** 55–71

Saleska S R *et al* 2003 Carbon in Amazon forests: unexpected seasonal fluxes and disturbance-induced losses *Science* **302** 1554–7

Samanta A *et al* 2012 Seasonal changes in leaf area of Amazon forests from leaf flushing and abscission *J. Geophys. Res. Biogeosci.* **117** G01015

Wright S J and Van Schaik C P 1994 Light and the phenology of tropical trees *Am. Nat.* **143** 192–9

Xiao X *et al* 2005 Satellite-based modeling of gross primary production in a seasonally moist tropical evergreen forest *Remote Sens. Environ.* **94** 105–22

Yang W *et al* 2006 MODIS leaf area index products: from validation to algorithm improvement *IEEE Trans. Geosci. Remote Sens.* **44** 1885–98

SUPPLEMENTARY INFORMATION

Sunlight mediated seasonality in canopy structure and photosynthetic activity of Amazonian rainforests

Jian Bi, Yuri Knyazikhin, Sungho Choi, Taejin Park, Jonathan Barichivich, Philippe Ciais, Rong Fu, Sangram Ganguly, Forrest Hall, Thomas Hilker, Alfredo Huete, Matthew Jones, John Kimball, Alexei I. Lyapustin, Matti Mõttus, Ramakrishna R. Nemani, Shilong Piao, Benjamin Poulter, Scott R. Saleska, Sassan S. Saatchi, Liang Xu, Liming Zhou, and Ranga B. Myneni

This document provides Supplementary information not provided in the main text of the article "Sunlight Mediated Seasonality in Canopy Structure and Photosynthetic Activity of Amazonian Rainforests." It contains (*i*) Supplementary Data and Methods, which provides an extended description of the data and methods used; (*ii*) Supplementary Discussion related to various issues in previous studies that led to incorrect conclusions; (*iii*) Supplementary References; (*iv*) Supplementary Figures and (*v*) Supplementary Tables.

Supplementary Data and Methods

1. Study region and greening pixels

This study is focused on a 1200×1200 km^2 region in central Amazonia (MODIS tile "h11v09"; 0° to 10°S and 60°W to 70°W; figure S1(a)). About 95% of this region is covered with terra firme rainforests (Nepstad *et al* 1994). The average annual rainfall varies from about 1800 mm in the south to about 3700 mm in the northwest (figure S1(b)). The number of dry months, generally defined as months with rainfall less than 100 mm, varies from about 4 in the south to less than 2 in the northwest. For comparison purposes (Morton *et al* 2014), the dry season is defined as June to October (137 mm/month) and the wet season as November to May (276 mm/month). This is one of two tiles studied by (Morton *et al* 2014). Expanding the area to match that study did not alter our results and conclusions.

Terra MODIS and MISR data analysed in this study consisted of seven seasonal cycles (June to May), while the Aqua MODIS data consisted of four cycles, as in (Morton *et al* 2014). Forest pixels with valid Enhanced Vegetation Index (EVI) data are classified as greening pixels during a seasonal cycle if the average EVI value during the month of October is greater than the average EVI value during the month of June. Here, EVI refers to Terra MODIS Collection 5 EVI data (Section 2.5). The MODIS and MISR analyses in this study are focused on these "greening pixels" because we wish to address this key question: is the dry season greening purely an artefact of variations in sun-sensor geometry (Galvão *et al* 2011, Morton *et al* 2014) or does it reflect actual changes in canopy after accounting for variations in sun-sensor geometry (Xiao *et al* 2005, Huete *et al* 2006, Myneni *et al* 2007, Brando *et al* 2010, Samanta *et al* 2012)? The proportion of greening pixels varies from year to year. It averages ~60% of all rainforest pixels in the case of the Terra MODIS sensor (table S1) due to strict quality filtering. Nearly every rainforest pixel in the study region exhibits dry season greening at least once, if not more, because the data are accumulated, not averaged, over multiple seasonal cycles.

2. Data

2.1. TRMM Precipitation Data: Monthly precipitation data from the Tropical Rainfall Measuring Mission (TRMM) at quarter degree spatial resolution for the period January 1998 to December 2012 (TRMM product 3B43, Version 7) are used in this study (WWW-TRMM).

2.2. CERES Surface PAR Fluxes: Monthly at-surface Photosynthetically Active Radiation (PAR,

400-700 nm; the sum of "Computed PAR Surface Flux Direct – All-sky" and "Computed PAR Surface Flux Diffuse – All-sky") data at 1°×1° spatial resolution from June 2000 to May 2008 are used in this study (WWW-CERES).

2.3. CRU Temperature Data: The latest version of the 0.5° temperature data set produced by the Climatic Research Unit (CRU; University of East Anglia; CRU TS3.21) is used in this study (WWW-CRU).

2.4. MODIS Land Cover: Evergreen broadleaf forests in the study region are identified using the Collection 5 land cover data set "MODIS Land Cover Type Yearly L3 Global 500 m SIN Grid" (MCD12Q1) (WWW-MCD12Q1).

2.5. MODIS NIR Reflectance and EVI: The following Collection 5 EVI data are used in this study: (a) Terra Moderate Resolution Imaging Spectroradiometer (MODIS) EVI data from June 2000 to May 2008 (WWW-MOD13A2) and (b) Aqua MODIS EVI data from June 2003 to May 2008 (WWW-MYD13A2). Data from June 2005 to May 2006 are not used due to the dry season drought in 2005 (Samanta *et al* 2010a). These data sets also include surface reflectance at the near infrared (NIR) spectral band (858 nm) and sun-sensor measurement geometry. The data are at a spatial resolution of 1×1 km^2 and 16-day temporal frequency. The same EVI data were used in previous studies (Galvão *et al* 2011, Morton *et al* 2014). The quality of NIR reflectance and MODIS EVI data in each pixel is assessed using the 16-bit quality flags (Samanta *et al* 2010b, Xu *et al* 2011). The number of pixels with valid EVI data in June, October and March are shown in table S2.

2.6. MODIS MAIAC EVI: EVI data from Terra (June 2000 to May 2008) and Aqua (June 2003 to May 2008) MODIS sensors at 1×1 km^2 spatial resolution and 8-day temporal frequency generated with the Multi-angle Implementation of Atmospheric Correction (MAIAC) algorithm (Lyapustin *et al* 2012) are used in this study (WWW-MAIAC). The MAIAC EVI data are standardized to a fixed sun-sensor geometry (nadir viewing direction, solar zenith angle of 45^o). Thus, the MAIAC EVI data are free of sun-sensor geometry effects.

2.7. MODIS LAI: Collection 5 Leaf Area Index (LAI) data from Terra MODIS for the period June 2000 to May 2008 are used in this study (WWW-MOD15A2). Data from June 2005 to May 2006 are excluded from analyses of LAI seasonal changes (figures 1 and 2) due to the dry season drought in 2005 (Samanta *et al* 2010a). The data are at 1×1 km^2 spatial resolution and 8-day temporal frequency. Valid LAI data in each 1×1 km^2 8-day pixel are identified using quality flags (Samanta *et al* 2011, Poulter and Cramer, 2009).

2.8. MISR Bidirectional Reflectance Factor: Land Surface Data (version 22) from the Terra Multiangle Imaging Spectroradiometer (MISR) for the period June 2000 to May 2008 are used in this study (WWW-ASDC). Data from June 2005 to May 2006 are not used due to the dry season drought in 2005 (Samanta *et al* 2010a). The data are at a spatial resolution of 1.1 × 1.1 km^2 and include Bidirectional Reflectance Factors (BRF) at the nine MISR view angles (nadir, ±26.1°, ±45.6°, ±60.0° and ±70.5°) in four spectral bands (446, 558, 672, and 866 nm). MISR data with LandQA=0 (cloud free, aerosol optical depth below 0.3) are considered valid.

2.9. GLAS Centroid and Apparent Reflectance: Data from the Geoscience Laser Altimeter System (GLAS) instrument onboard the Ice, Cloud and land Elevation Satellite (ICESat) acquired during four periods – May 20 to June 23, 2005 (L3c), May 24 to June 26, 2006 (L3f), October 3 to November 8, 2004 (L3a) and October 2 to November 5, 2007 (L3i) – are used to analyze the sensitivity of the waveform centroid relative height (WCRH) and Apparent Reflectance (AR) to LAI (WWW-GLAS). The same data were used in (Morton *et al* 2014). For comparison purposes, low quality data were filtered as described in (Morton *et al* 2014). Additionally, GLAS footprints over non-forest and/or bare ground were screened by imposing the following conditions: (a) MODIS Land Cover corresponding to GLAS footprints is "Evergreen Broadleaf Forests" and (b) number of GLAS waveform Gaussian peaks exceeds one. GLAS lidar analysis is focused on the region spanning 0° to 10°S and 60°W to 80°W – the spatial extent of the blue and red squares in figure S1(a).

3. Sun-Sensor Geometry

Three angles characterize the sun-sensor geometry of a pixel (figure S1(c)): (a) solar zenith angle (SZA), (b) relative azimuth angle (RAA), and (c) view zenith angle (VZA). All three change

during the year in the case of MODIS. The distribution of these angles for pixels in the study region during each of the twenty-three 16-day compositing periods in a year is shown in figure 1 for Terra MODIS. The geometry for Aqua MODIS is very similar to that of Terra MODIS. The view zenith angles are fixed in the case of MISR. The following discussion of sun-sensor geometry is specific to this study's region (figure S1(a)).

The geometry in terms of SZA and RAA is approximately cyclical with a period of six months (figures 1(b) and (c)). Terra and Aqua MODIS and Terra MISR measurements are made at higher SZA ($\sim 30^o$ to 40^o) about the solstices, June/July and December/January, and at lower SZA ($\sim 20^o$ to 30^o) about the equinoxes, September/October and February/March (figure 1(b)). The progression of Terra and Aqua MODIS RAA during the year shows a similar cyclical behavior (figure 1(c)). The measurements are made closer to the solar azimuthal plane, or the principal plane, (RAA $\sim 0°$ and $180°$), about the equinoxes and approximately $\pm 30°$ to $\pm 45°$ off the orthogonal plane (RAA $\sim 130^o$ and 50^o) about the solstices (figure 1(c) and figure S2). View zenith angle varies between $0°$ (nadir) and $60°$ (figure 1(d)). The RAA of MISR sampling along the spacecraft flight track follows its Terra counterpart, but is shifted by about $90°$ (not shown). Half of Terra and Aqua MODIS observations about the solstices were collected at VZA below $15°$ and $20°$, respectively. Around 50% of the measurements about the equinoxes were made at VZA below $35°$ (Terra) and $20°$ (Aqua). The MISR VZAs are strongly peaked as expected around their nominal values of $0.0°$, $\pm 26.1°$, $\pm 45.6°$, $\pm 60.0°$ and $\pm 70.5°$ (figure S2).

Choosing three 16-day composites, one each in June (Jun 25 to Jul 10), October (Oct 15 to 30) and March (Mar 5 to 20), is sufficient to assess whether the previously reported seasonality in radiometric greenness (Xiao *et al* 2005, Huete *et al* 2006, Brando *et al* 2010) and leaf area (Myneni *et al* 2007, Samanta *et al* 2012) of Amazonian rainforests is an artefact of sun-sensor geometry (Galvão *et al* 2011, Morton *et al* 2014) or not. The three periods correspond to the beginning of the dry season, end of the dry season and mid wet season, respectively. The Terra and Aqua MODIS observations provide pairs of matching RAA (October vs. March), varying RAA (June vs. October), matching SZA (Terra and Aqua in June and March), varying SZA (October from Terra and Aqua) (figure S2). The Terra MISR sensor samples the surface close to the principal plane in June and near the orthogonal plane in October and March. This manner of sampling is opposite to that of MODIS (figure S2). The juxtaposition of MODIS and MISR sampling provides an interesting opportunity for assessing the presence or absence of seasonal variations in these rainforests.

4. Forest Reflectance

4.1. Bidirectional Reflectance Factor (BRF): The reflected radiation field from a vegetation canopy illuminated by a solar beam in a coordinate system with the polar axis pointed to the sun is considered here. The reflected radiance is expressed relative to a surface perpendicular to the solar beam and depends on the phase angle, γ, and azimuth, ψ. The phase angle is the angle between the directions to the sun and sensor (figure S1(c)). The plane ψ is chosen such that the phase angle varies between $-(90° + \theta_0)$ and $+(90° - \theta_0)$ where θ_0 is the sun zenith angle. In this coordinate system the Bidirectional Reflectance Factor, $BRF(\gamma, \psi)$, is the ratio of radiance reflected from the vegetation canopy to the radiance reflected from an ideal Lambertian surface under identical illumination conditions. The Lambertian surface in this instance is perpendicular to the solar beams. For a plane given by ψ and $\psi + 180°$, the BRF is a function of SZA, phase angle and wavelength. Its magnitude and angular shape depends on the composition, density, geometric structure of the reflecting medium, in addition to the foliage optical properties.

4.2. Transformation of MODIS and MISR BRF data: Let $BRF_{xy}(\theta_0, \theta_v, \Delta\varphi)$ be the observed BRF at a location (x, y) on the Earth's surface. The BRF_{xy} is a standard product of MODIS and MISR sensors, which is expressed relative to a horizontal surface. The sun-sensor geometry is represented by the sun, θ_0, and sensor, θ_v, view zenith angles, and the view azimuth φ_v (figure S1(c)). First, we introduce a new coordinate system with the polar axis pointed to the sun. The quantities, $I_{xy} = BRF_{xy} \cos\theta_0$, represent radiances reflected from forests illuminated by a

parallel beam of unit intensity. The radiances are expressed relative to the unit surface perpendicular to the solar beam and depend on the phase angle, γ, and azimuth, ψ, in this system. The phase angle is the angle between directions to the sun and sensor, i.e., $\gamma = \text{acos}[\cos\theta_v \cos\theta_0 + \sin\theta_v \sin\theta_0 \cos\varphi_v]$.

Second, we group I_{xy} with respect to the phase angle (figure S3). This procedure transforms the standard BRF product into BRF expressed in terms of the phase angle, γ, and azimuth, ψ. The azimuth specifies sampling plane of satellite-borne sensors. The MODIS instrument scans the Earth across the Terra and Aqua spacecraft flight track, which is approximately from East to West (figure S3(a)). The MISR instrument measures reflected radiation along the Terra flight track, which is approximately from North to South (figure S3(b)). The sampling planes are fixed for MODIS and MISR instruments. We assign the sign "plus" to γ if the direction to the sensor approaches the direction to sun from East (Terra MODIS), West (Aqua MODIS) or North (Terra MISR), and "minus" otherwise. The phase angle varies between $-(90° + \theta_0)$ and $90° - \theta_0$. The probability density distribution function $p(\theta_0, \gamma)$ of the phase angle is evaluated from the fraction of data in each group.

Finally, the reflected radiances in each group are averaged. This methodology is applied to transform standard BRF products from Terra and Aqua MODIS observations (figure S3(a)). In the case of MISR, the algorithm is applied to each MISR camera to derive camera specific BRF (figure S3(b)) and corresponding probability density functions. The camera specific BRFs for which $|\gamma - \bar{\gamma}| \leq \sigma$ are used in further analyses. Here $\bar{\gamma}$ and σ denote camera specific mean and standard deviation of the phase angle γ.

4.3. Effect of Changing Canopy Properties on BRF: figures S5(a) and (b) illustrate the effect of changing canopy properties on BRF. Here, SZA is held constant. An increase in LAI, with leaf optical properties unchanged, increases the interception of incoming solar radiation by the vegetation canopy, which in turn increases the amount of reflected radiation. This increases the magnitude of BRF at all phase angles, i.e. a non-linear upward shift in the angular signature of the BRF, as shown in figure S5(b). The overall shape of the BRF remains unchanged. This is a well-known fact: the reflectance of dense vegetation, or a vegetation canopy with a dark background, is an increasing function of LAI (e.g. figure 1 in (Huang *et al* 2008)). Changes in leaf optical properties either augment or suppress the LAI effect on the reflectance factor (Samanta *et al* 2012). Thus, changing canopy properties and holding SZA constant changes the magnitude of the BRF but not the overall shape of the signature. This explains the observed BRF changes in figures 3(a) and (b).

4.4. Effect of Changing SZA on BRF: figures S5(c) and (d) illustrate the effect of changing SZA on BRF. Here, canopy properties are held constant. The cumulative contribution of within-canopy sources generated by single- and multiple-scattered photons to canopy-exiting radiation along a given direction increases with photon path length, L, as $\sim(1 - \exp(-\sigma L))$, where L is the distance between sources within the canopy and the upper boundary of the canopy and σ is the extinction coefficient. An increase in SZA results in longer photon path lengths for positive phase angles (figure S5(c)). The opposite is true for negative phase angles. Increasing SZA with constant canopy therefore results in an asymmetric transformation of the BRF signature, that is, enhanced values for positive phase angles and depressed values for negative phase angles (figure S5(d)). It also decreases the range of BRF variation at positive phase angles and a corresponding increase in the range of BRF variation at negative phase angles. Thus, both the shape and magnitude of the BRF signature are changed. The asymmetric transformation also causes the two BRF signatures to intersect, as illustrated in figure S5(d). The phase angle at which the two signatures intersect can be calculated using the principle of directional reciprocity (Section 4.6).

It is important to note that the path L varies with SZA as $\sim 1/\cos(SZA)$. It means that effect of changing SZA on the BRF's angular shape is weak at low SZA. For example, a change in SZA from 20° to 30° involves a change in L from ~1.06 to ~1.15. The impact, however, increases with SZA. This explains why SZA variation has no discernable impact on the angular signatures of reflectances in figures 3(a) and (b).

4.5. Effect of Changing Canopy Properties and SZA on BRF: figures S5(e) and (f) illustrate the effect of changing both canopy properties and SZA on BRF. Changing canopy properties but holding SZA constant changes the magnitude of BRF but retains its overall angular shape (Section 4.3). Changing SZA but holding canopy properties invariant changes the magnitude of BRF differently for positive and negative phase angles, thus changing the shape of the BRF as well (Section 4.4). Changing canopy properties and SZA simultaneously combines these two effects, i.e. the BRF is transformed asymmetrically and shifted in magnitude. For example, decreasing SZA depresses the BRF at positive phase angles and enhances the same at negative phase angles – transformation of the green colored BRF signature to dashed-blue color signature in figure S5(f). Increasing canopy properties, say LAI and/or foliage optical properties, shifts the overall BRF signature up in magnitude – transformation of the dashed-blue color signature to solid-blue color signature in figure S5(f). This explains the BRF signature changes in figures 3(c) and (d). Importantly, it follows from this argumentation that *higher or equal values of BRF at lower SZA relative to BRFs at higher SZA always indicate a change in canopy properties*.

4.6. Proof of Dry Season Changes From the Directional Reciprocity Principle: The optical reciprocity theorem (Davis and Knyazikhin, 2005) provides a proof relevant to our study. It states that switching detector and source and inverting the directions of propagation yield the same result for BRF. It follows from the theorem that the BRFs of a canopy, or two similar canopies, corresponding to different sun positions, say Ω_0 and Ω_1, necessarily intersect at $\gamma_0 = -\text{acos}(\Omega_0 \cdot \Omega_1)$. Indeed, the BRF in direction Ω_1 due to a mono-directional solar beam in direction $-\Omega_0$ is related to the BRF in direction Ω_0 due to a mono-directional solar beam in direction $-\Omega_1$ as $BRF(-\Omega_0, +\gamma) = BRF(-\Omega_1, -\gamma)$. If $BRF(-\Omega_0, \gamma)$ is symmetric at $\gamma_0 = \text{acos}(\Omega_0 \cdot \Omega_1)$ (e.g., as in October), the BRFs should intersect at $\gamma_0 = -\text{acos}(\Omega_0 \cdot \Omega_1)$. Changing canopy properties with illumination conditions unchanged results in an upward or downward shift in the angular signature of the BRF (Section 4.5). This causes the intersection point to deviate from γ_0, indicating a difference in canopy properties. The deviation of the intersection point around $-5.5°$ from $\gamma_0 = -37.1°$ shown in figure 3(d) is significant, indicating *different canopy properties in June and October*.

Supplementary Discussion

Galvão *et al* (2011) and Morton *et al* (2014) claim that previous studies (Xiao *et al* 2005, Huete *et al* 2006, Myneni *et al* 2007, Brando *et al* 2010, Samanta *et al* 2012) misinterpreted changes in near-infrared (NIR) reflectance caused by seasonal changes in sun-satellite sensor geometry as seasonal variations in rainforest canopy structure and greenness. They conclude that Amazonian rainforests maintain consistent structure and greenness during the dry season based on their analysis of satellite borne sensor data (MODIS and Lidar) and model exercises. Here we present a detailed critique of their analysis.

An incomplete analysis of the seasonal cycle, i.e. one that is focused only on the dry season, encourages misleading interpretation of both intra- and inter-annual greenness (EVI or LAI) variations as artefacts of changing sun-sensor geometry. For example, if the sun-sensor geometry artefact argument is valid, then the seasonal course of LAI from December to May should be similar to that from June to November because of a repeat in sun-sensor geometry (figures 1(b) and (c)), but it is not (figure 1(a)). Also, if the change in MODIS sampling from the orthogonal plane in June to the principal plane in October (figures S2(a) and (c)) causes the rainforests to appear greener, then the change in MISR sampling from the principal plane in June to the orthogonal plane in October (figures S2(b) and (d)) should cause the rainforests to appear browner. But, greening is observed as well (figure 3(d)).

Interannually, the attribution of anomalous dry season greening (increase in EVI or LAI) in drought year 2005, *vis a vis* dry seasons of non-drought years, to a higher proportion of brighter backscattering MODIS observations is flawed because it is selectively based on data from the first fortnight of October (ED-figure 9 (Morton *et al* 2014)). A higher fraction of backscattering measurements is not seen in 2005 when the analysis is focused on July to September period

(figure S4(b)) as in the original studies (Samanta *et al* 2010a, Samanta *et al* 2010b, Saleska *et al* 2007). Moreover, if claims of geometric artefacts are true, higher backscatter fraction and greenness should also be seen during the more intense dry season drought in 2010 (Xu *et al* 2011). They are not (figure S4(b)), even in their selective analysis (ED-figure 9 (Morton *et al* 2014)).

Crucially, the misinterpretations in Morton *et al* (2014) stem from reliance on prognostications of an untested radiative transfer model. In a critical test of how well the model simulates variation in sunlit and shaded proportions of the canopy, which is central to arguments about geometric artefacts, the model underestimates measurements by ~45% (figure S4(c)). The model is also unrealistically sensitive to litter reflectance in dense vegetation (table 1 (Morton *et al* 2014)), an indication of incorrect physics and/or modeling of foliage spatial distribution. The failure to test the model is compounded by an unquestioned belief in its validity, else the observed dry season greening in geometry-corrected EVI would not have been ignored (figure 3(b) (Morton *et al* 2014) and ED-figure 7(b) (Morton *et al* 2014)). Various statistical analyses of this geometry-corrected EVI data strongly reject the null hypothesis of no change in forest greenness (Saleska *et al* 2015). Indeed the physics of radiative transfer in dense media (Section 2.9 (Knyazikhin *et al* 1999)) informs that these changes in geometry-corrected EVI (figure 2, figure 3(b) in (Morton *et al* 2014) and ED-figure 7(b) in (Morton *et al* 2014)) correspond to large changes in LAI (figure. 1(a)). Thus, there is no valid statistical or theoretical basis to dismiss dry season increase in geometry-corrected EVI (figure 2(b), figure 3(b) in (Morton *et al* 2014) and ED-figure 7(b) in (Morton *et al* 2014)).

The unorthodox belief that Amazonian rainforests should conform to model predictions affects their interpretation of satellite lidar data also. The conclusion that structure and greenness of rainforests remain invariant does not follow from absence of evidence in lidar data for their model prediction that an increase in LAI from 4.5 to 6.5 should result in an increase in Waveform Centroid Relative Height - the height of median return energy relative to the full waveform extent (WCRH; table 1 in (Morton *et al* 2014)). A prudent interpretation might be that the model prediction does not conform to data. Even if the model is assumed to be capable of accurate predictions, the predicted change in WCRH (0.06) is comparable to the spatial standard deviations of June and October WCRH data (~0.07). This clearly suggests a need for additional analysis.

The lack of insight into what might be reasonably expected from lidar data and saturation of lidar signals in dense vegetation compound the problem of detecting seasonal LAI changes. For example, studies that have investigated the relationship between LAI and lidar waveforms (Castillo *et al* 2012, Tang *et al* 2012, Drake *et al* 2002) show that WCRH saturates in mature and secondary growth tropical forests aged over ~20 years (Tang *et al* 2012, Drake *et al* 2002) because the majority of lidar hits are confined to the upper canopy. This saturation of signals emanating from vegetation is different than sensor saturation (Neuenschwander *et al* 2008) – the latter have been filtered out from all analyses.

The saturation effect can be potentially documented through these three analyses. First, although a range of LAI values are observed in Amazonian rainforests, from about 4 to 6 in June and greater than 6 in October, the two lidar metrics, WCRH and Apparent Reflectance (AR), exhibit no correspondent variations (figure S6). Second, rainforests with low (3.5 to 4.5) and high (greater than 5.5) LAI have the same WCRH and AR (figures S7 (a) and (b)). Third, rainforests with low (<0.5) and high (>0.6) WCRH have the same LAI (figure S7(c)). Likewise, rainforests with low (<0.5) and high (>0.6) AR have identical LAI (figure S7(d)). Inference of saturation from figure S6 and figures S7 (a)–(d) depends on the validity of the MODIS LAI data. To alleviate this concern, we present similar results for deciduous broadleaf forests where a broader range of LAI values are encountered. The curvilinear relationship in deciduous forests, where WCRH increases for LAI values 0 to 3 and saturates thereafter (figures S8(a) and (c)), is as expected, and is similar to other relations between LAI and remote measurements (Knyazikhin *et al* 1999, Huang *et al* 2008).

Unlike WCRH, the AR shows no relationship to LAI (figures S6 (b) and (d), figures S8 (b) and (d)), even in sparsely foliated canopies (LAI less

than 3; figures S8 (b) and (d)). Also, the inverse relationship with WCRH is perplexing (figures S7 (e) and (f)). To ascertain whether these results indicate potential data quality problems, we investigated the relationship between the lidar metrics and key climatic variables that govern plant growth, i.e. water, radiation and temperature (Nemani *et al* 2003). The WCRH data are positively related (p-value < 0.001) to all three climatic variables (table S4). This is as it should be, i.e. tall and dense tree stands with higher WCRH are located in climatically favorable environments of higher annual precipitation, solar radiation and mean temperature (table S4). The AR data, on the other hand, show negative relation with two of the three climatic variables. We therefore conclude that GLAS AR data have quality problems.

Morton *et al* (2014)'s interpretations of AR data are contradictory - on the one hand, their validity is discounted by citing corruption from aerosols due to biomass burning, and on the other hand, their invariance is counted as proof that Amazonian rainforests maintain consistent structure and greenness (figure 2(c) (Morton *et al* 2014)). Why table 1 (Morton *et al* 2014) does not show model predictions of AR seasonal variations, unlike WCRH, is unknown. Given these ambiguities, their analyses of AR data must also be deemed inconclusive.

In addition to the analyses presented in this article, three independent studies have rebutted Galvão *et al* (2011) and Morton *et al* (2014) claims with a multitude of satellite and in situ data (Maeda *et al* 2014, Hilker *et al* 2014, Jones *et al* 2014). Dry season greening in sun-sensor geometry corrected data obtained from Morton et al. is due for publication (Saleska *et al* 2015).

Supplementary References

Brando P M, Goetz S J, Baccini A, Nepstad D C, Beck P S and Christman M C 2010 Seasonal and interannual variability of climate and vegetation indices across the Amazon. *Proc. Natl. Acad. Sci. USA.* **107** 14685–14690

Castillo M, Rivard B, Sánchez-Azofeifa A, Calvo-Alvarado J and Dubayah R 2012 LIDAR remote sensing for secondary Tropical Dry Forest identification. *Remote Sens. Environ.* **121** 132–143

Davis A B and Knyazikhin Y 2005 A primer in 3D radiative transfer. *Three Dimensional Radiative Transfer in the Cloudy Atmosphere*, eds Marshak A, Davis A B (Springer-Verlag, Berlin Heidelberg), pp 153-242

Drake J B, et al. 2002 Estimation of tropical forest structural characteristics using large-footprint lidar. *Remote Sens. Environ.* **79** 305–319

Galvão L S, Dos Santos J R, Roberts D A, Breunig F M, Toomey M and de Moura Y M 2011 On intra-annual EVI variability in the dry season of tropical forest: A case study with MODIS and hyperspectral data. *Remote Sens. Environ.* **115** 2350–2359

Hilker T *et al* 2014 Vegetation dynamics and rainfall sensitivity of the Amazon. *Proc. Natl. Acad. Sci. USA.* **111** 16041–16046

Huang D *et al* 2008 Stochastic transport theory for investigating the three-dimensional canopy structure from space measurements. *Remote Sens. Environ.* **112** 35–50

Huete A R *et al* 2006 Amazon rainforests green-up with sunlight in dry season. *Geophys. Res. Lett.* **33** L06405

Jones M O, Kimball J S and Nemani R R 2014 Asynchronous Amazon forest canopy phenology indicates adaptation to both water and light availability. *Environ. Res. Lett.* **9** 124021

Knyazikhin Y *et al* 1999 *MODIS leaf area index (LAI) and fraction of photosynthetically active radiation absorbed by vegetation (FPAR) product (MOD15) algorithm theoretical basis document*, <https://lpdaac.usgs.gov/products/modis_products_table/mcd15a2>

Lyapustin A I *et al* 2012 Multi-angle implementation of atmospheric correction for MODIS (MAIAC): 3. Atmospheric correction. *Remote Sens. Environ.* **127** 385–393

Maeda E E, Heiskanen J, Aragão L E O C and Rinne J 2014 Can MODIS EVI monitor ecosystem productivity in the Amazon rainforest? *Geophys. Res. Lett.* **41** 7176–7183

Morton D C *et al* 2014 Amazon forests maintain consistent canopy structure and greenness during the dry season. *Nature* **506** 221–224

Myneni R B *et al* 2007 Large seasonal swings in leaf area of Amazon rainforests. *Proc. Natl. Acad. Sci. USA* **104** 4820–4823

Nemani R R *et al* 2003 Climate-driven increases in global terrestrial net primary production from 1982 to 1999. *Science* **300** 1560–1563

Nepstad D C *et al* 1994 The role of deep roots in the hydrological and carbon cycles of Amazonian forests and pastures *Nature* **372** 666–669

Neuenschwander A L, Urban T J, Gutierrez R and Schutz B E 2008 Characterization of ICESat/GLAS waveforms over terrestrial ecosystems: Implications for vegetation mapping. *J. Geophys. Res. Biogeosci.* **113** G02S03

Poulter B and Cramer W 2009 Satellite remote sensing of tropical forest canopies and their seasonal dynamics. *Int. J. Remote Sens.* **30** 6575–6590

Saleska S R *et al* 2015 Dry-season greening of Amazon forests. Brief Communications Arising in *Nature* (in press)

Saleska S R, Didan K, Huete A R and Da Rocha H R 2007 Amazon forests green-up during 2005 drought. *Science* **318** 612–612

Samanta A *et al* 2010a Amazon forests did not green-up during the 2005 drought. *Geophy. Res. Lett.* **37** L05401

Samanta A *et al* 2012 Seasonal changes in leaf area of Amazon forests from leaf flushing and abscission. *J. Geophys. Res. Biogeosci.* **117** G01015

Samanta A, Costa M H, Nunes, E L, Vieira S A, Xu, L and Myneni R B 2011 Comment on "Drought-Induced Reduction in Global Terrestrial Net Primary Production from 2000 Through 2009". *Science* **333** 1093

Samanta A, Ganguly S and Myneni R B 2010b MODIS Enhanced Vegetation Index data do not show greening of Amazon forests during the 2005 drought. *New Phytol.* **189** 11–15

Tang H *et al* 2012 Retrieval of vertical LAI profiles over tropical rain forests using waveform lidar at La Selva, Costa Rica. *Remote Sens. Environ.***124** 242–250

WWW-ASDC. NASA Langley Research Center Atmospheric Science Data Center (ASDC) Home page. Available at https://eosweb.larc.nasa.gov/

WWW-CERES. Atmospheric Science Data Center: The Clouds and the Earth's Radiant Energy System (CERES). Available at https://eosweb.larc.nasa.gov/project/ceres/ceres_table

WWW-CRU. Climatic Research Unit (CRU) Time-Series High-Resolution Gridded Datasets. Available at http://www.cru.uea.ac.uk/cru/data/hrg/

WWW-GLAS. Geoscience Laser Altimeter System (GLAS) lidar waveform data. Available at https://nsidc.org/data/icesat/data-dictionaries-landing-page.html

WWW-MAIAC. MAIAC Amazon Data. *Level 1 and Atmosphere Archive and Distribution System (LAADS)*. Available at ftp://ladsweb.nascom.nasa.gov/MAIAC/

WWW-MCD12Q1. Land Cover Type Yearly L3 Global 500 m SIN Grid (MCD12Q1). *Land Process Distributed Active Archive Center*. Available at https://lpdaac.usgs.gov/products/modis_products_table/mcd12q1

WWW-MOD13A2. Vegetation Indices 16-Day L3 Global 1km (MOD13A2). *Land Process Distributed Active Archive Center*. Available at https://lpdaac.usgs.gov/products/modis_products_table/myd13a12

WWW-MOD15A2. Leaf Area Index - Fraction of Photosynthetically Active Radiation 8-Day L4 Global 1km (MOD15A2). *Land Process Distributed Active Archive Center.* Available at https://lpdaac.usgs.gov/products/modis_products_table/mod15a12

WWW-MYD13A2. Vegetation Indices 16-Day L3 Global 1km (MYD13A2). *Land Process Distributed Active Archive Center*. Available at https://lpdaac.usgs.gov/products/modis_products_table/myd13a12

WWW-TRMM. Tropical Rainfall Measuring Mission (TRMM) data. *Goddard Earth Science Data and Information Center*. Available at http://mirador.gsfc.nasa.gov/

Xiao X *et al* 2005 Satellite-based modeling of gross primary production in a seasonally moist tropical evergreen forest. *Remote. Sens. Environ.* **94** 105–122

Xu L *et al* 2011 Widespread decline in greenness of Amazonian vegetation due to the 2010 drought. *Geophy. Res. Lett.* **38** L07402

Yang W *et al* 2006 MODIS leaf area index products: From validation to algorithm improvement. *IEEE Trans. Geosci. Remote. Sens.* **44** 1885–1898

Supplementary Figures

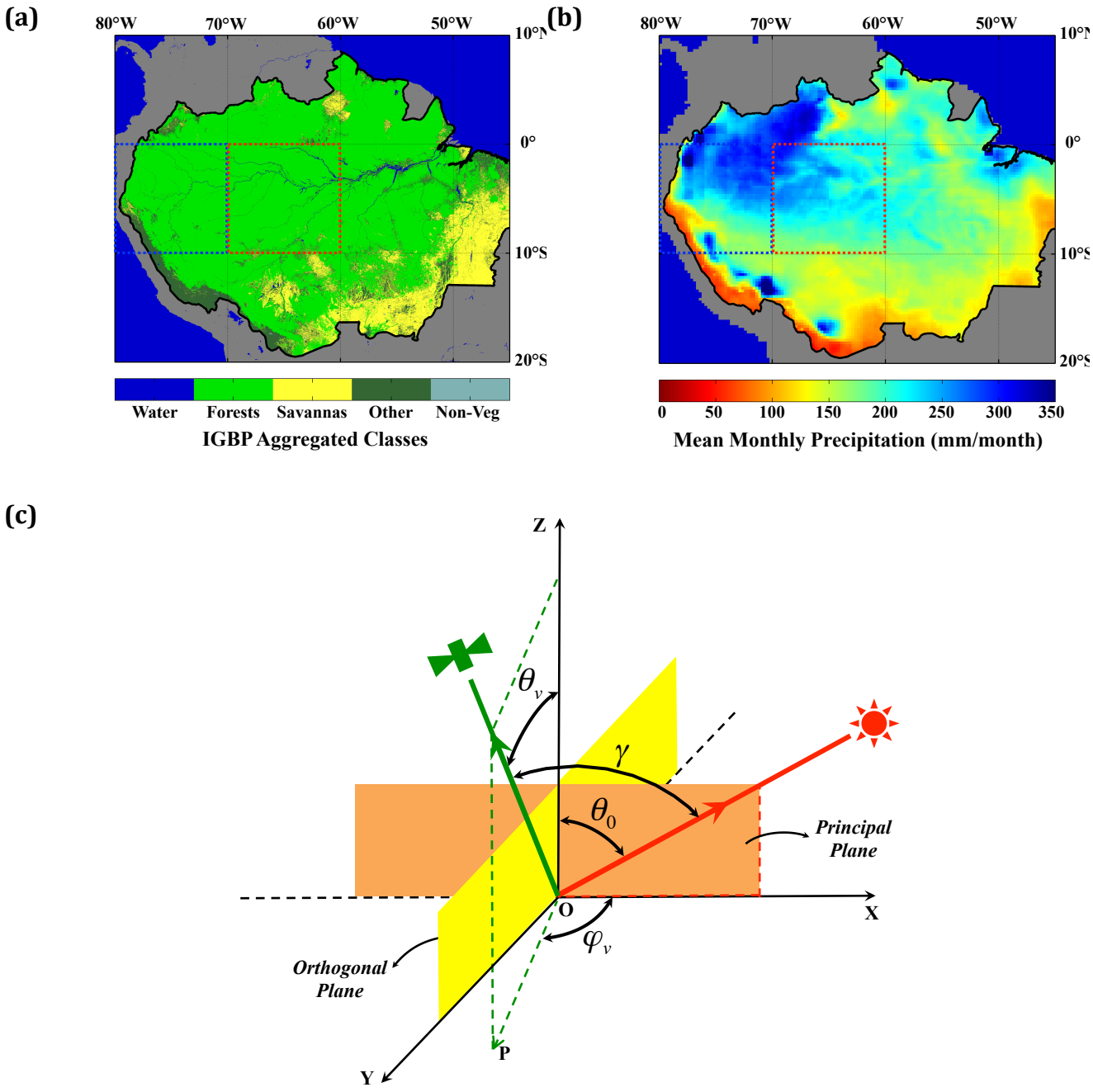

Figure S1. The study domain and sun-sensor geometry. (a) The domain of MODIS and MISR analysis is the red square. The domain of GLAS lidar analysis is both blue and red squares. (b) Monthly mean rainfall from TRMM. (c) Three angles characterize the sun-sensor measurement geometry of a pixel: (1) solar zenith angle, SZA=θ_0 ($0° < \theta_0 \leq 90°$), (2) view zenith angle, VZA=θ_v ($0° \leq \theta_v \leq 90°$) and (3) view azimuth, φ_v ($0° \leq \varphi_v \leq 360°$), measured relative to the principal plane. The angle between the projection, OP, of the direction to the sensor and X axis is the relative azimuth angle (RAA), i.e., RAA=φ_v if $0 \leq \varphi_v < 180°$ and RAA=$360° - \varphi_v$, otherwise. It varies between 0° and 180°. The angle between the directions to the sun and sensor is the phase angle, PA=γ.

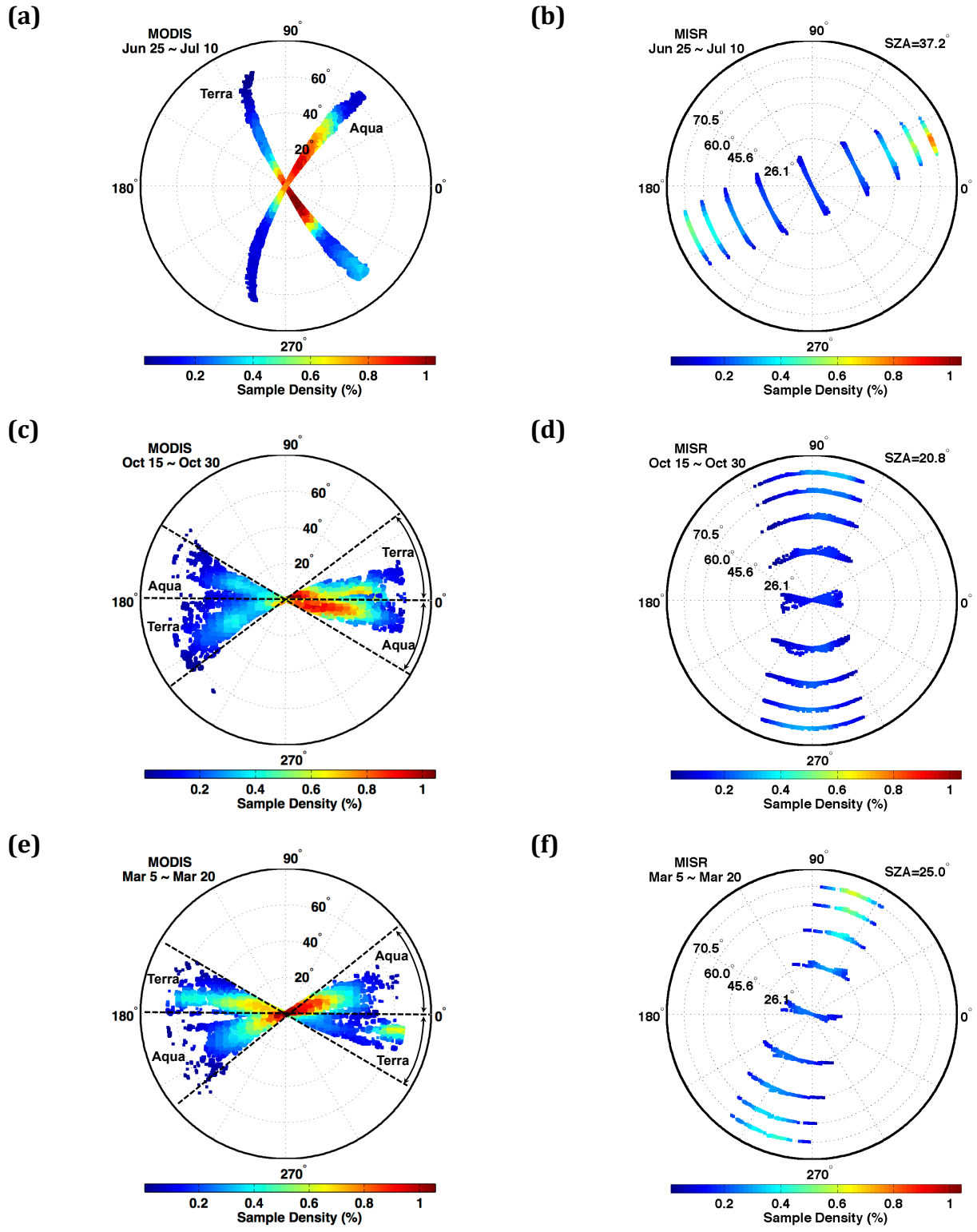

Figure S2. MODIS and MISR sampling geometries. Terra and Aqua MODIS (left panels) and Terra MISR (right panels) sampling geometries during a 16-day compositing period in the months of (a, b) June 2003, (c, d) October 2003, and (e, f) March 2003. The MODIS sensors sample the surface close to the orthogonal plane in June and near the principal plane in October and March. This sampling is opposite to that of MISR sensor.

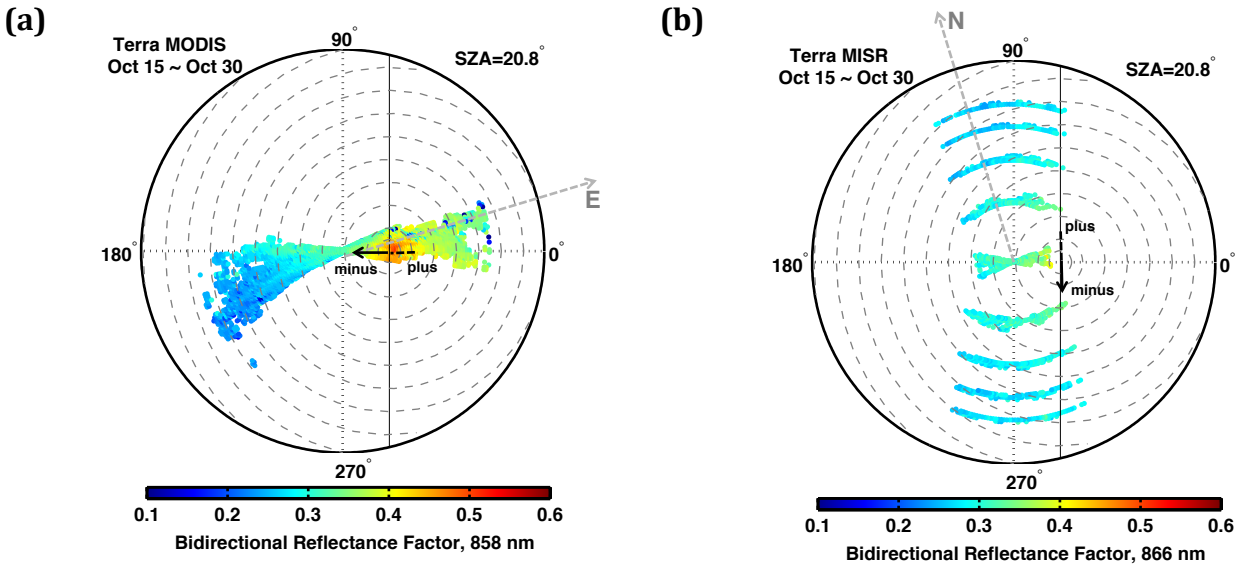

Figure S3. MODIS and MISR reflectances in a modified coordinate system. Terra MODIS (a) and MISR (b) NIR BRFs during a 16-day composite in October 2003. BRF values are expressed in a coordinate system with the polar axis pointed to the Sun. Solid arrows indicate sampling direction that determines the phase angle sign (angle between solar and sensor view directions).

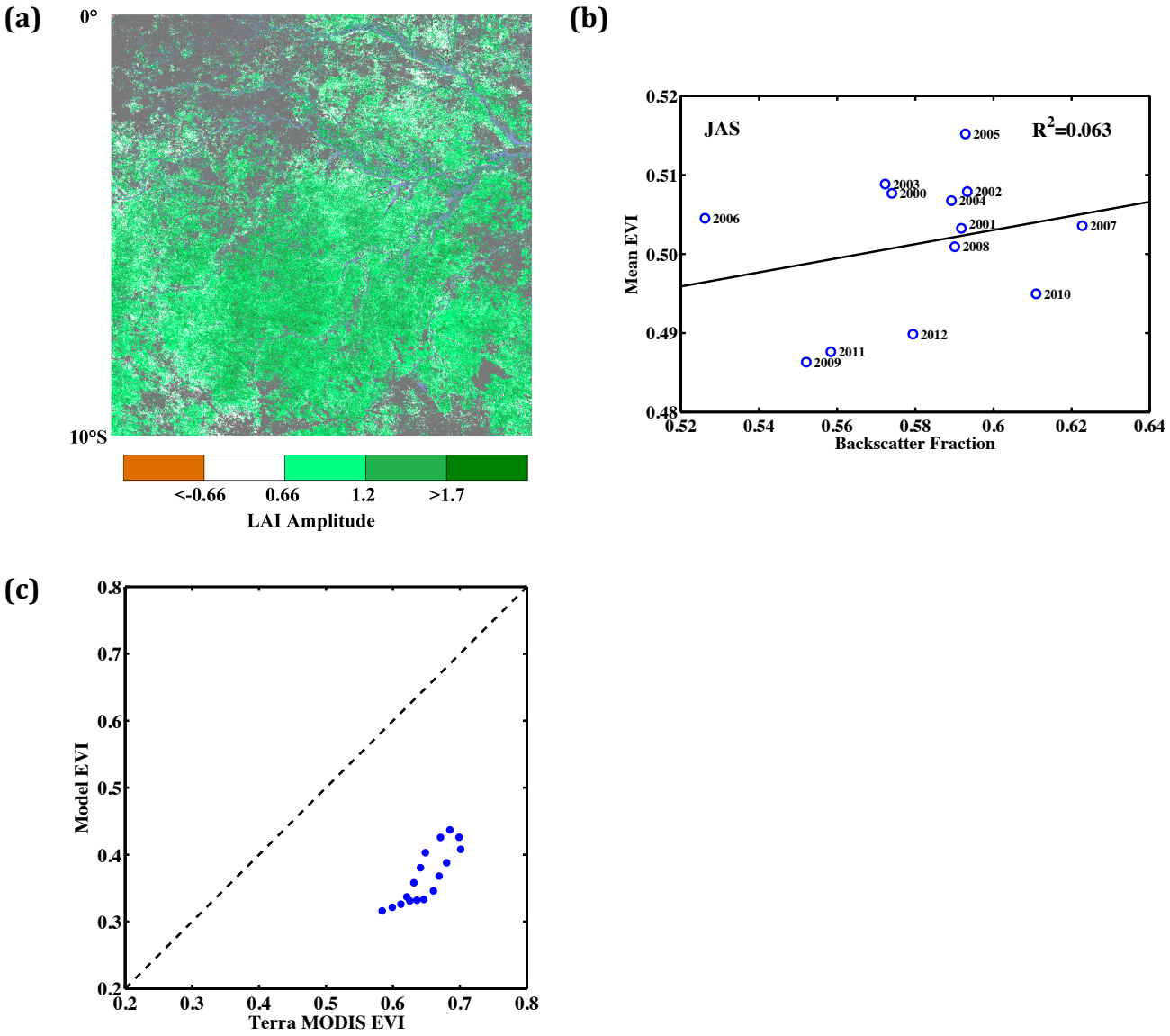

Figure S4. Evidence for seasonality of leaf area and misinterpretation of data following the guidance of an erroneous radiative transfer model (Morton *et al* 2014). (a) Spatial pattern of seasonal Terra MODIS LAI amplitude expressed as the difference between the maximum value during September to November and the minimum value during the following May to June period. White pixels denote locations with LAI amplitudes less than |0.66|, which is the accuracy of MODIS LAI data (Yang *et al* 2006). White and colored pixels together denote pixels that exhibited dry season greening in at least 4 out of 7 seasonal cycles (63% of all forest pixels in the study region). (b) Mean Terra MODIS EVI over rainforests as a function of backscattering fraction evaluated from all 16-day compositing periods in July, August and September (DOY 177 to 272). The backscattering fraction is defined (Morton *et al* 2014) as the fraction of observations with view azimuth less than 90° and greater than 270°. (c) Comparison of model simulated EVI (obtained by digitizing figure 1(c) in Morton *et al* (2014)) with Terra MODIS EVI over Amazonian rainforests. The MODIS EVI is from a 16-day October composite (15th to the 30th) accumulated over 7 seasonal cycles (Section 2.5). The comparison is for phase angles in the range ±10°, that is, ±10° around the hot spot (view zenith angles from 10° to 30° in figure 1(c) of (Morton *et al* 2014)).

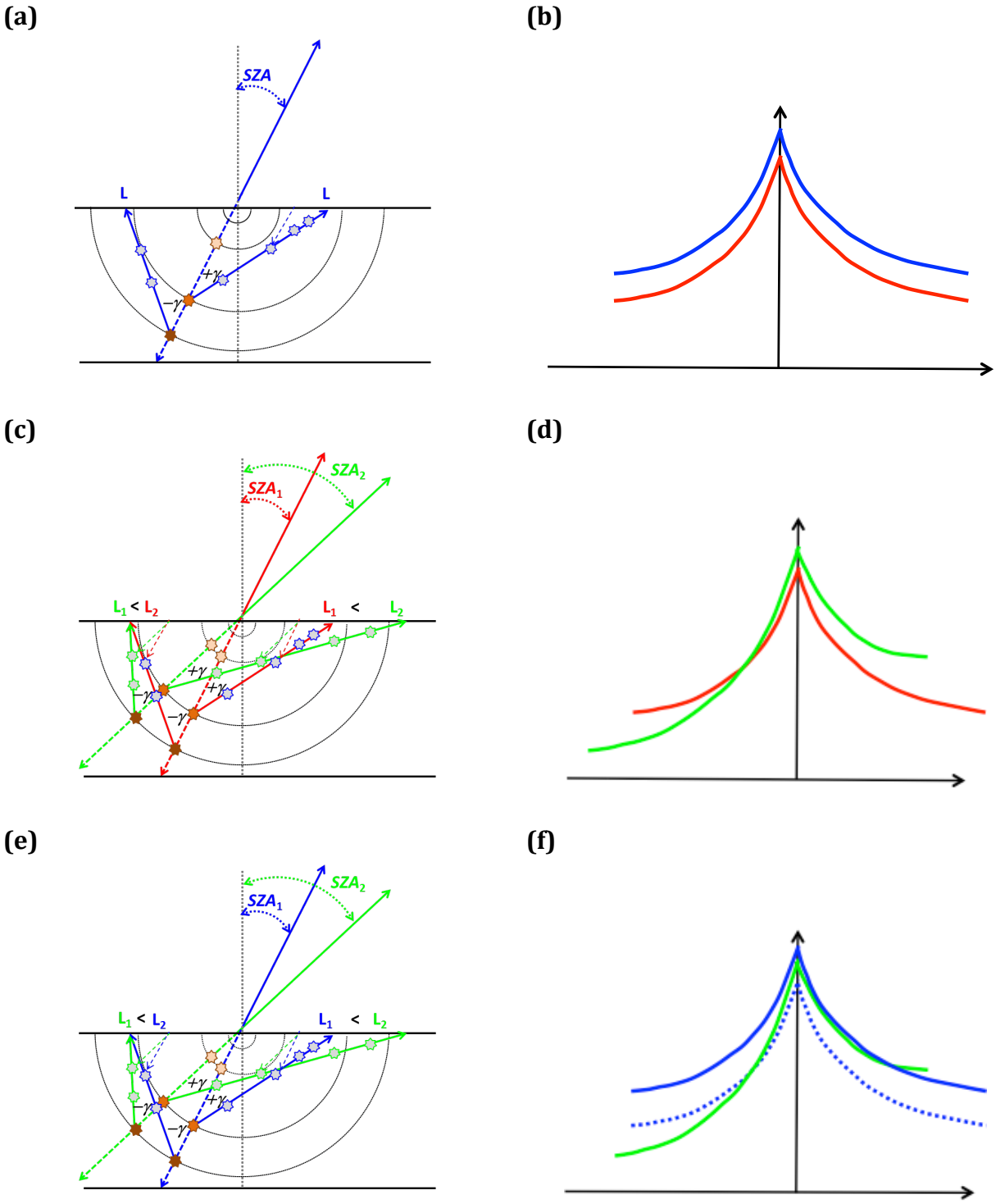

Figure S5. Interpretation of angular signatures of reflectance. Illustration of how the angular signature of Bidirectional Reflectance Factors (BRF) is transformed when (a, b) sun-sensor geometry is held invariant but canopy properties are changed; (c, d) sun-sensor geometry is changed but canopy properties are held invariant; (e, f) both sun-sensor geometry and canopy properties are changed. The dashed arrows depict direction of incident parallel beam of unit intensity.

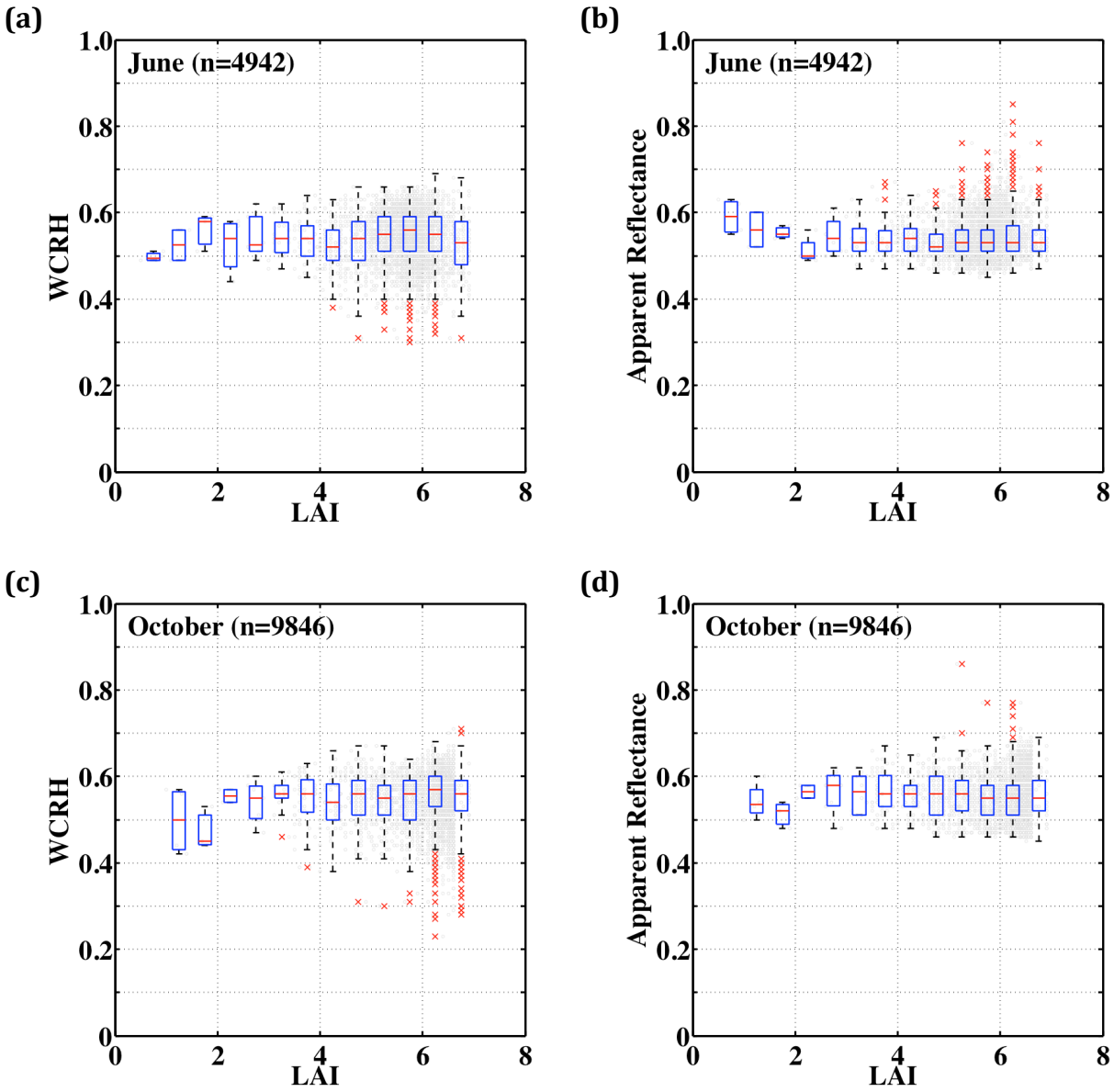

Figure S6. Saturation of GLAS lidar metrics over central Amazonian forests. Distributions of GLAS Waveform Centroid Relative Height (WCRH) and Apparent Reflectance as a function of Terra MODIS LAI in the case of central Amazonian rainforests at the (a, b) beginning and (c, d) end of the dry season. Gray dots and red crosses show distributions of lidar metrics within 0.5 LAI bins. Upper, middle (red line) and lower box edges show the 75%, 50% and 25% percentiles of GLAS metrics. The red crosses are outliers, each representing upper and lower 0.25% of the GLAS lidar observations. June represents data from May-20 to June-23, 2005 and May-24 to June-26, 2006. October represents data from October-3 to November-8, 2004 and October-2 to November-5, 2007. MODIS pixels with valid LAI values and four or more GLAS lidar observations were used (table S3).

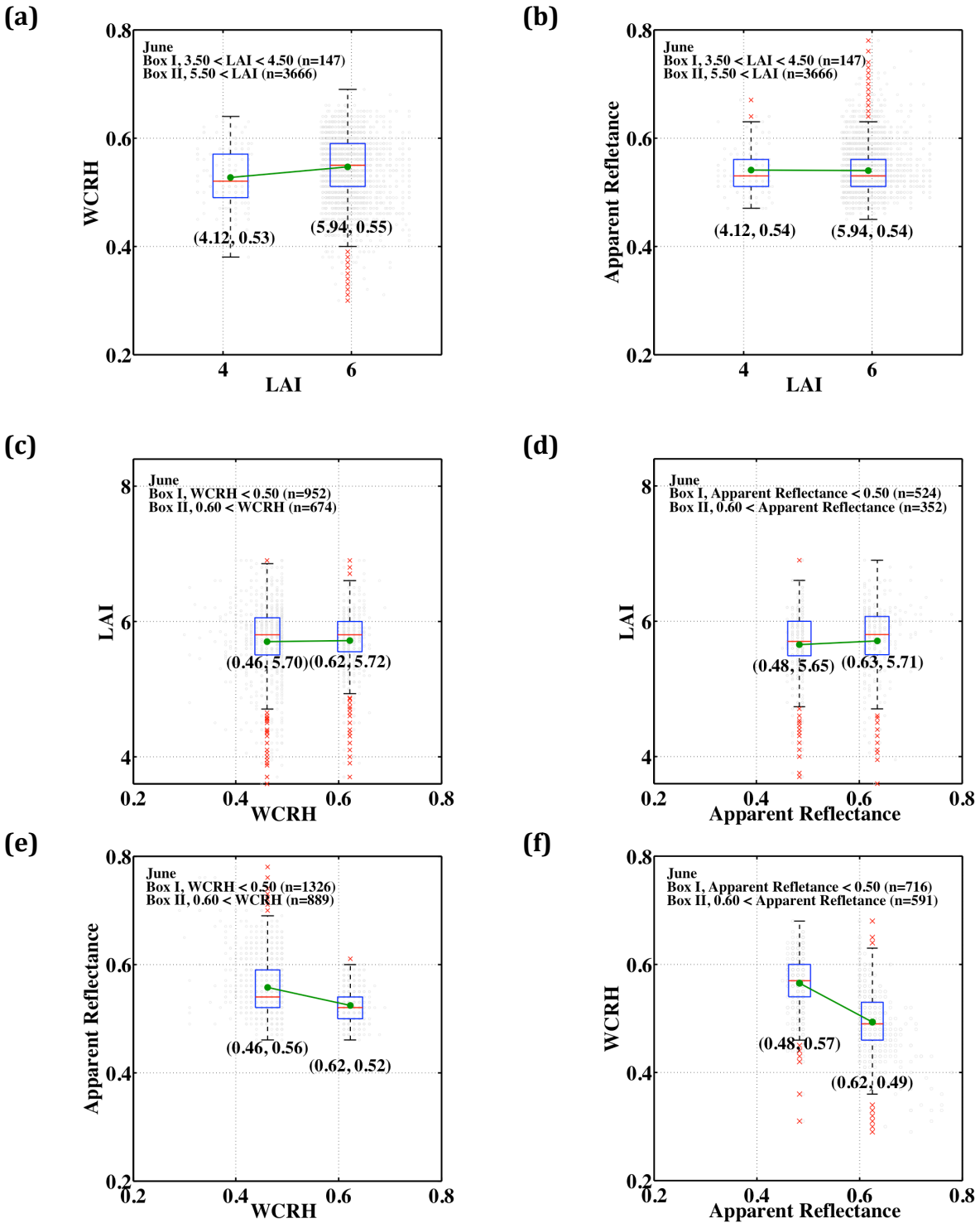

Figure S7. Relationship between GLAS lidar metrics and with LAI. (a, b) Variation in GLAS Waveform Centroid Relative Height (WCRH) and Apparent Reflectance (AR) for pixels with low and high Terra MODIS LAI values. (c, d) Variation in LAI for pixels with low and high values of WCRH and AR. (e, f) Relationship between WCRH and AR. Gray dots and red crosses show the data. Upper, middle (red line) and lower box edges separate the 75%, 50% and 25% percentiles of data used. The red crosses are outliers, each representing upper and lower 0.25% of the data. Similar relations are found for October (not shown).

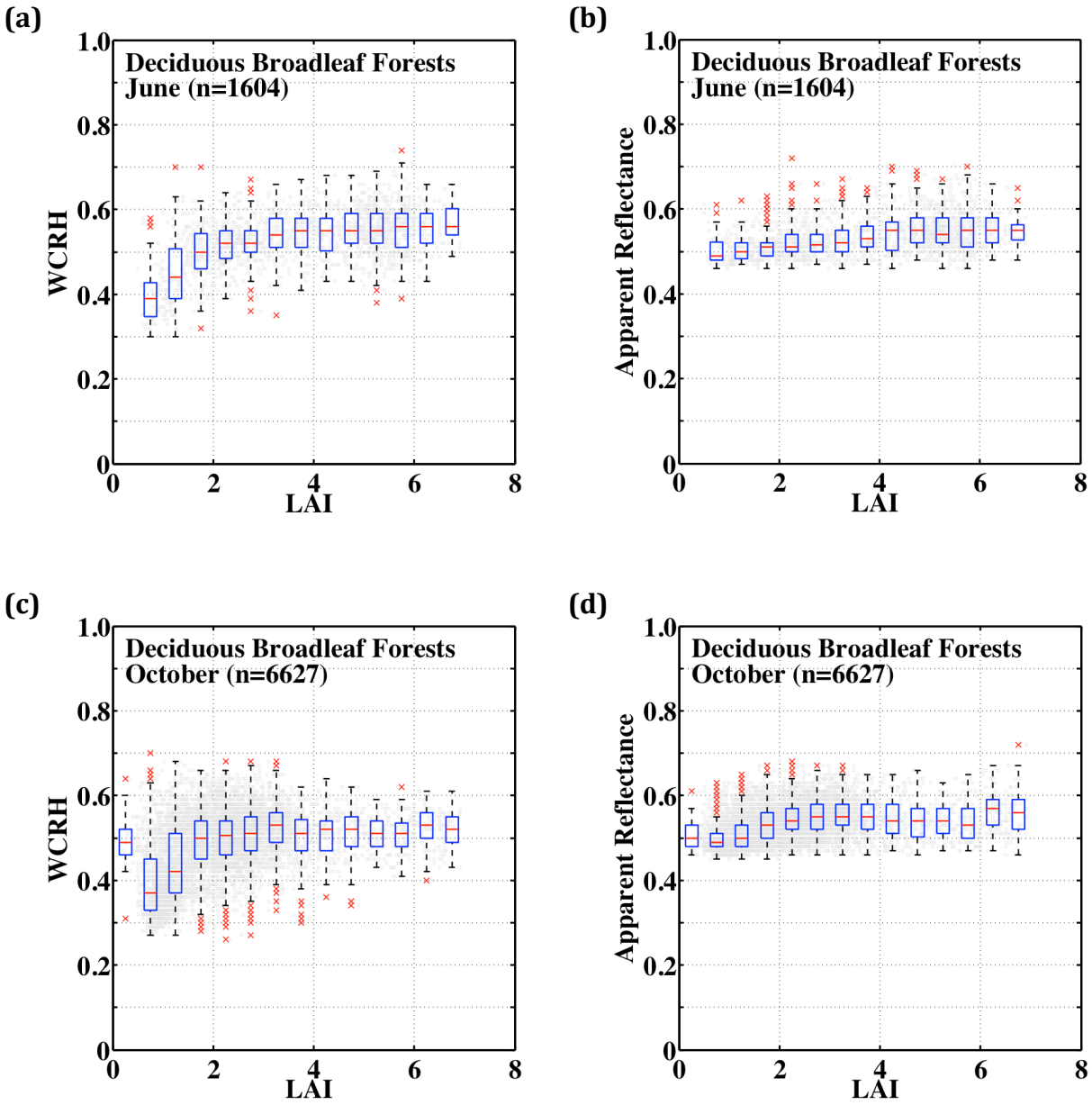

Figure S8. Relationship between GLAS lidar metrics and LAI in deciduous broadleaf forests. Distributions of GLAS Waveform Centroid Relative Height (WCRH) and Apparent Reflectance as a function of Terra MODIS LAI in the case of deciduous (temperate) broadleaf forests in the northern hemisphere in (a, b) June and (c, d) October. Gray dots and red crosses show distributions of lidar metrics within 0.5 LAI bins. Upper, middle (red line) and lower box edges show the 75%, 50% and 25% percentiles of GLAS metrics. The red crosses are outliers, each representing upper and lower 0.25% of the GLAS lidar observations. June represents data from May-20 to June-23, 2005 and May-24 to June-26, 2006. October represents data from October-3 to November-8, 2004 and October-2 to November-5, 2007. MODIS pixels with valid LAI values and four or more GLAS lidar observations were used (table S3).

Supplementary Tables

Table S1. Number of greening pixels (Section 1) from Terra and Aqua MODIS sensors

	Terra		Aqua	
Year	Number of greening pixels	As a % of rainforest pixels	Number of greening pixels	As a % of rainforest pixels
2000	804,550	59.02	N/A	N/A
2001	723,796	53.10	N/A	N/A
2002	990,863	72.69	N/A	N/A
2003	518,857	38.06	238,998	17.53
2004	919,820	67.48	233,140	17.10
2005	N/A	N/A	N/A	N/A
2006	901,602	66.14	227,926	16.72
2007	783,164	57.45	260,370	19.10

Table S2. Number of pixels with valid EVI and BRF data in June, October and March accumulated over a 7-year period (June 2000 to May 2008, excluding June 2005 to May 2006 due to the dry season drought in 2005) from Terra MODIS and MISR sensors. The table also shows the same for the Aqua MODIS sensor, but accumulated over a 4-year period (June 2003 to May 2008 excluding June 2005 to May 2006)

		Fraction of Rainforest Pixels With Valid Data (%)		
Sensor	Number of Valid Data	June	October	March
Terra MODIS	One or more	96.67	94.38	70.92
Aqua MODIS	One or more	33.65	30.32	12.10
Terra MISR	One or more	48.07	25.75	15.33

Table S3. Number of pixels with valid Terra MODIS LAI data and four or more valid GLAS footprints in June and October

	June		October	
Year	Number of valid LAI pixels	Number of corresponding GLAS footprints	Number of valid LAI pixels	Number of corresponding GLAS footprints
		Amazonian Rainforests		
2004	N/A	N/A	3,859	17,293
2005	3,031	13,536	N/A	N/A
2006	1,911	8,607	N/A	N/A
2007	N/A	N/A	5,987	29,858
Total	4,942	22,143	9,846	47,151
		Deciduous Broadleaf Forests		
2004	N/A	N/A	2,419	10,719
2005	955	4,164	N/A	N/A
2006	649	2,761	N/A	N/A
2007	N/A	N/A	4,208	19,650
Total	1,604	6,925	6,627	30,369

Table S4. Regression relationships between climate and GLAS Waveform Centroid Relative Height (WCRH) and Apparent Reflectance (AR). Climate is represented by annual total precipitation from TRMM, photosynthetically active radiation from CERES and mean annual temperature from CRU. Long-term means of climate variables were evaluated from 2001 to 2010 data, but excluding 2005 and 2010 drought years. Each TRMM pixel contains 10 or more GLAS observations; CERES pixel has 160 or more, and CRU pixel has 40 or more

x	y	Slope	Intercept	R^2	p-value
WCRH	Annual Precipitation (mm $year^{-1}$)	4428.3	297.1	0.17	<0.001
WCRH	Photosynthetically Active Radiation (W m^{-2})	21.8	83.6	0.08	<0.001
WCRH	Mean Annual Temperature (°C)	8.3	22.1	0.15	<0.001
AR	Annual Precipitation (mm $year^{-1}$)	-600.4	3011.2	0.00	0.16
AR	Photosynthetically Active Radiation (W m^{-2})	-65.6	130.9	0.26	<0.001
AR	Mean Annual Temperature (°C)	-10.3	32.1	0.10	<0.001

Table S5. List of Abbreviations

AR	Apparent Reflectance
Aqua	NASA scientific research satellite in a Sun-synchronous near polar circular orbit around the Earth; crosses Equator at 1:30pm
BRF	Bidirectional Reflectance Factor
C5	Collection 5
CERES	Clouds and the Earth's Radiant Energy System
CRU	Climatic Research Unit
DOY	Day of Year (designates the beginning of the compositing period)
ED	Extended Data
EVI	Enhanced Vegetation Index
GLAS	Geoscience Laser Altimeter System
ICESat	Ice, Cloud and land Elevation Satellite
JAS	July, August, and September
LAI	Leaf Area Index
LiDAR	Light Detection and Ranging
MAIAC	Multi-angle Implementation of Atmospheric Correction
MISR	Multiangle Imaging Spectroradiometer
MODIS	Moderate-resolution Imaging Spectroradiometer
NASA	National Aeronautics and Space Administration
NIR	Near Infrared
PA	Phase angle
PAR	Photosynthetically Active Radiation
PDF	Probability Density Function
RAA	Relative Azimuth Angle between solar and sensor view directions
SI	Supplementary Information
SZA	Solar Zenith Angle
SOM	Space Oblique Mercator
Terra	NASA scientific research satellite in a Sun-synchronous near polar circular orbit around the Earth; crosses Equator at 10:30am
TRMM	Tropical Rainfall Measuring Mission
VI	Vegetation Index
VZA	View Zenith Angle
WCRH	Waveform Centroid Relative Height

SUPPLEMENTARY INFORMATION

Sunlight mediated seasonality in canopy structure and photosynthetic activity of Amazonian rainforests

Jian Bi, Yuri Knyazikhin, Sungho Choi, Taejin Park, Jonathan Barichivich, Philippe Ciais, Rong Fu, Sangram Ganguly, Forrest Hall, Thomas Hilker, Alfredo Huete, Matthew Jones, John Kimball, Alexei I. Lyapustin, Matti Mõttus, Ramakrishna R. Nemani, Shilong Piao, Benjamin Poulter, Scott R. Saleska, Sassan S. Saatchi, Liang Xu, Liming Zhou, and Ranga B. Myneni

This document provides Supplementary information not provided in the main text of the article "Sunlight Mediated Seasonality in Canopy Structure and Photosynthetic Activity of Amazonian Rainforests." It contains (*i*) Supplementary Data and Methods, which provides an extended description of the data and methods used; (*ii*) Supplementary Discussion related to various issues in previous studies that led to incorrect conclusions; (*iii*) Supplementary References; (*iv*) Supplementary Figures and (*v*) Supplementary Tables.

Supplementary Data and Methods

1. Study region and greening pixels

This study is focused on a 1200×1200 km^2 region in central Amazonia (MODIS tile "h11v09"; 0° to 10°S and 60°W to 70°W; figure S1(a)). About 95% of this region is covered with terra firme rainforests (Nepstad *et al* 1994). The average annual rainfall varies from about 1800 mm in the south to about 3700 mm in the northwest (figure S1(b)). The number of dry months, generally defined as months with rainfall less than 100 mm, varies from about 4 in the south to less than 2 in the northwest. For comparison purposes (Morton *et al* 2014), the dry season is defined as June to October (137 mm/month) and the wet season as November to May (276 mm/month). This is one of two tiles studied by (Morton *et al* 2014). Expanding the area to match that study did not alter our results and conclusions.

Terra MODIS and MISR data analysed in this study consisted of seven seasonal cycles (June to May), while the Aqua MODIS data consisted of four cycles, as in (Morton *et al* 2014). Forest pixels with valid Enhanced Vegetation Index (EVI) data are classified as greening pixels during a seasonal cycle if the average EVI value during the month of October is greater than the average EVI value during the month of June. Here, EVI refers to Terra MODIS Collection 5 EVI data (Section 2.5). The MODIS and MISR analyses in this study are focused on these "greening pixels" because we wish to address this key question: is the dry season greening purely an artefact of variations in sun-sensor geometry (Galvão *et al* 2011, Morton *et al* 2014) or does it reflect actual changes in canopy after accounting for variations in sun-sensor geometry (Xiao *et al* 2005, Huete *et al* 2006, Myneni *et al* 2007, Brando *et al* 2010, Samanta *et al* 2012)? The proportion of greening pixels varies from year to year. It averages ~60% of all rainforest pixels in the case of the Terra MODIS sensor (table S1) due to strict quality filtering. Nearly every rainforest pixel in the study region exhibits dry season greening at least once, if not more, because the data are accumulated, not averaged, over multiple seasonal cycles.

2. Data

2.1. TRMM Precipitation Data: Monthly precipitation data from the Tropical Rainfall Measuring Mission (TRMM) at quarter degree spatial resolution for the period January 1998 to December 2012 (TRMM product 3B43, Version 7) are used in this study (WWW-TRMM).

2.2. CERES Surface PAR Fluxes: Monthly at-surface Photosynthetically Active Radiation (PAR,

400-700 nm; the sum of "Computed PAR Surface Flux Direct – All-sky" and "Computed PAR Surface Flux Diffuse – All-sky") data at 1°×1° spatial resolution from June 2000 to May 2008 are used in this study (WWW-CERES).

2.3. CRU Temperature Data: The latest version of the 0.5° temperature data set produced by the Climatic Research Unit (CRU; University of East Anglia; CRU TS3.21) is used in this study (WWW-CRU).

2.4. MODIS Land Cover: Evergreen broadleaf forests in the study region are identified using the Collection 5 land cover data set "MODIS Land Cover Type Yearly L3 Global 500 m SIN Grid" (MCD12Q1) (WWW-MCD12Q1).

2.5. MODIS NIR Reflectance and EVI: The following Collection 5 EVI data are used in this study: (a) Terra Moderate Resolution Imaging Spectroradiometer (MODIS) EVI data from June 2000 to May 2008 (WWW-MOD13A2) and (b) Aqua MODIS EVI data from June 2003 to May 2008 (WWW-MYD13A2). Data from June 2005 to May 2006 are not used due to the dry season drought in 2005 (Samanta *et al* 2010a). These data sets also include surface reflectance at the near infrared (NIR) spectral band (858 nm) and sun-sensor measurement geometry. The data are at a spatial resolution of 1×1 km^2 and 16-day temporal frequency. The same EVI data were used in previous studies (Galvão *et al* 2011, Morton *et al* 2014). The quality of NIR reflectance and MODIS EVI data in each pixel is assessed using the 16-bit quality flags (Samanta *et al* 2010b, Xu *et al* 2011). The number of pixels with valid EVI data in June, October and March are shown in table S2.

2.6. MODIS MAIAC EVI: EVI data from Terra (June 2000 to May 2008) and Aqua (June 2003 to May 2008) MODIS sensors at 1×1 km^2 spatial resolution and 8-day temporal frequency generated with the Multi-angle Implementation of Atmospheric Correction (MAIAC) algorithm (Lyapustin *et al* 2012) are used in this study (WWW-MAIAC). The MAIAC EVI data are standardized to a fixed sun-sensor geometry (nadir viewing direction, solar zenith angle of 45^o). Thus, the MAIAC EVI data are free of sun-sensor geometry effects.

2.7. MODIS LAI: Collection 5 Leaf Area Index (LAI) data from Terra MODIS for the period June 2000 to May 2008 are used in this study (WWW-MOD15A2). Data from June 2005 to May 2006 are excluded from analyses of LAI seasonal changes (figures 1 and 2) due to the dry season drought in 2005 (Samanta *et al* 2010a). The data are at 1×1 km^2 spatial resolution and 8-day temporal frequency. Valid LAI data in each 1×1 km^2 8-day pixel are identified using quality flags (Samanta *et al* 2011, Poulter and Cramer, 2009).

2.8. MISR Bidirectional Reflectance Factor: Land Surface Data (version 22) from the Terra Multiangle Imaging Spectroradiometer (MISR) for the period June 2000 to May 2008 are used in this study (WWW-ASDC). Data from June 2005 to May 2006 are not used due to the dry season drought in 2005 (Samanta *et al* 2010a). The data are at a spatial resolution of 1.1 × 1.1 km^2 and include Bidirectional Reflectance Factors (BRF) at the nine MISR view angles (nadir, ±26.1°, ±45.6°, ±60.0° and ±70.5°) in four spectral bands (446, 558, 672, and 866 nm). MISR data with LandQA=0 (cloud free, aerosol optical depth below 0.3) are considered valid.

2.9. GLAS Centroid and Apparent Reflectance: Data from the Geoscience Laser Altimeter System (GLAS) instrument onboard the Ice, Cloud and land Elevation Satellite (ICESat) acquired during four periods – May 20 to June 23, 2005 (L3c), May 24 to June 26, 2006 (L3f), October 3 to November 8, 2004 (L3a) and October 2 to November 5, 2007 (L3i) – are used to analyze the sensitivity of the waveform centroid relative height (WCRH) and Apparent Reflectance (AR) to LAI (WWW-GLAS). The same data were used in (Morton *et al* 2014). For comparison purposes, low quality data were filtered as described in (Morton *et al* 2014). Additionally, GLAS footprints over non-forest and/or bare ground were screened by imposing the following conditions: (a) MODIS Land Cover corresponding to GLAS footprints is "Evergreen Broadleaf Forests" and (b) number of GLAS waveform Gaussian peaks exceeds one. GLAS lidar analysis is focused on the region spanning 0° to 10°S and 60°W to 80°W – the spatial extent of the blue and red squares in figure S1(a).

3. Sun-Sensor Geometry

Three angles characterize the sun-sensor geometry of a pixel (figure S1(c)): (a) solar zenith angle (SZA), (b) relative azimuth angle (RAA), and (c) view zenith angle (VZA). All three change

during the year in the case of MODIS. The distribution of these angles for pixels in the study region during each of the twenty-three 16-day compositing periods in a year is shown in figure 1 for Terra MODIS. The geometry for Aqua MODIS is very similar to that of Terra MODIS. The view zenith angles are fixed in the case of MISR. The following discussion of sun-sensor geometry is specific to this study's region (figure S1(a)).

The geometry in terms of SZA and RAA is approximately cyclical with a period of six months (figures 1(b) and (c)). Terra and Aqua MODIS and Terra MISR measurements are made at higher SZA ($\sim 30^o$ to 40^o) about the solstices, June/July and December/January, and at lower SZA ($\sim 20^o$ to 30^o) about the equinoxes, September/October and February/March (figure 1(b)). The progression of Terra and Aqua MODIS RAA during the year shows a similar cyclical behavior (figure 1(c)). The measurements are made closer to the solar azimuthal plane, or the principal plane, (RAA $\sim 0°$ and $180°$), about the equinoxes and approximately $\pm 30°$ to $\pm 45°$ off the orthogonal plane (RAA $\sim 130^o$ and 50^o) about the solstices (figure 1(c) and figure S2). View zenith angle varies between $0°$ (nadir) and $60°$ (figure 1(d)). The RAA of MISR sampling along the spacecraft flight track follows its Terra counterpart, but is shifted by about $90°$ (not shown). Half of Terra and Aqua MODIS observations about the solstices were collected at VZA below $15°$ and $20°$, respectively. Around 50% of the measurements about the equinoxes were made at VZA below $35°$ (Terra) and $20°$ (Aqua). The MISR VZAs are strongly peaked as expected around their nominal values of $0.0°$, $\pm 26.1°$, $\pm 45.6°$, $\pm 60.0°$ and $\pm 70.5°$ (figure S2).

Choosing three 16-day composites, one each in June (Jun 25 to Jul 10), October (Oct 15 to 30) and March (Mar 5 to 20), is sufficient to assess whether the previously reported seasonality in radiometric greenness (Xiao *et al* 2005, Huete *et al* 2006, Brando *et al* 2010) and leaf area (Myneni *et al* 2007, Samanta *et al* 2012) of Amazonian rainforests is an artefact of sun-sensor geometry (Galvão *et al* 2011, Morton *et al* 2014) or not. The three periods correspond to the beginning of the dry season, end of the dry season and mid wet season, respectively. The Terra and Aqua MODIS observations provide pairs of matching RAA (October vs. March), varying RAA (June vs. October), matching SZA (Terra and Aqua in June and March), varying SZA (October from Terra and Aqua) (figure S2). The Terra MISR sensor samples the surface close to the principal plane in June and near the orthogonal plane in October and March. This manner of sampling is opposite to that of MODIS (figure S2). The juxtaposition of MODIS and MISR sampling provides an interesting opportunity for assessing the presence or absence of seasonal variations in these rainforests.

4. Forest Reflectance

4.1. Bidirectional Reflectance Factor (BRF): The reflected radiation field from a vegetation canopy illuminated by a solar beam in a coordinate system with the polar axis pointed to the sun is considered here. The reflected radiance is expressed relative to a surface perpendicular to the solar beam and depends on the phase angle, γ, and azimuth, ψ. The phase angle is the angle between the directions to the sun and sensor (figure S1(c)). The plane ψ is chosen such that the phase angle varies between $-(90° + \theta_0)$ and $+(90° - \theta_0)$ where θ_0 is the sun zenith angle. In this coordinate system the Bidirectional Reflectance Factor, $BRF(\gamma, \psi)$, is the ratio of radiance reflected from the vegetation canopy to the radiance reflected from an ideal Lambertian surface under identical illumination conditions. The Lambertian surface in this instance is perpendicular to the solar beams. For a plane given by ψ and $\psi + 180°$, the BRF is a function of SZA, phase angle and wavelength. Its magnitude and angular shape depends on the composition, density, geometric structure of the reflecting medium, in addition to the foliage optical properties.

4.2. Transformation of MODIS and MISR BRF data: Let $BRF_{xy}(\theta_0, \theta_v, \Delta\varphi)$ be the observed BRF at a location (x, y) on the Earth's surface. The BRF_{xy} is a standard product of MODIS and MISR sensors, which is expressed relative to a horizontal surface. The sun-sensor geometry is represented by the sun, θ_0, and sensor, θ_v, view zenith angles, and the view azimuth φ_v (figure S1(c)). First, we introduce a new coordinate system with the polar axis pointed to the sun. The quantities, $I_{xy} = BRF_{xy} \cos\theta_0$, represent radiances reflected from forests illuminated by a

parallel beam of unit intensity. The radiances are expressed relative to the unit surface perpendicular to the solar beam and depend on the phase angle, γ, and azimuth, ψ, in this system. The phase angle is the angle between directions to the sun and sensor, i.e., $\gamma = \text{acos}[\cos\theta_v \cos\theta_0 + \sin\theta_v \sin\theta_0 \cos\varphi_v]$.

Second, we group I_{xy} with respect to the phase angle (figure S3). This procedure transforms the standard BRF product into BRF expressed in terms of the phase angle, γ, and azimuth, ψ. The azimuth specifies sampling plane of satellite-borne sensors. The MODIS instrument scans the Earth across the Terra and Aqua spacecraft flight track, which is approximately from East to West (figure S3(a)). The MISR instrument measures reflected radiation along the Terra flight track, which is approximately from North to South (figure S3(b)). The sampling planes are fixed for MODIS and MISR instruments. We assign the sign "plus" to γ if the direction to the sensor approaches the direction to sun from East (Terra MODIS), West (Aqua MODIS) or North (Terra MISR), and "minus" otherwise. The phase angle varies between $-(90° + \theta_0)$ and $90° - \theta_0$. The probability density distribution function $p(\theta_0, \gamma)$ of the phase angle is evaluated from the fraction of data in each group.

Finally, the reflected radiances in each group are averaged. This methodology is applied to transform standard BRF products from Terra and Aqua MODIS observations (figure S3(a)). In the case of MISR, the algorithm is applied to each MISR camera to derive camera specific BRF (figure S3(b)) and corresponding probability density functions. The camera specific BRFs for which $|\gamma - \bar{\gamma}| \leq \sigma$ are used in further analyses. Here $\bar{\gamma}$ and σ denote camera specific mean and standard deviation of the phase angle γ.

4.3. Effect of Changing Canopy Properties on BRF: figures S5(a) and (b) illustrate the effect of changing canopy properties on BRF. Here, SZA is held constant. An increase in LAI, with leaf optical properties unchanged, increases the interception of incoming solar radiation by the vegetation canopy, which in turn increases the amount of reflected radiation. This increases the magnitude of BRF at all phase angles, i.e. a non-linear upward shift in the angular signature of the BRF, as shown in figure S5(b). The overall shape of the BRF remains unchanged. This is a well-known fact: the reflectance of dense vegetation, or a vegetation canopy with a dark background, is an increasing function of LAI (e.g. figure 1 in (Huang *et al* 2008)). Changes in leaf optical properties either augment or suppress the LAI effect on the reflectance factor (Samanta *et al* 2012). Thus, changing canopy properties and holding SZA constant changes the magnitude of the BRF but not the overall shape of the signature. This explains the observed BRF changes in figures 3(a) and (b).

4.4. Effect of Changing SZA on BRF: figures S5(c) and (d) illustrate the effect of changing SZA on BRF. Here, canopy properties are held constant. The cumulative contribution of within-canopy sources generated by single- and multiple-scattered photons to canopy-exiting radiation along a given direction increases with photon path length, L, as $\sim(1 - \exp(-\sigma L))$, where L is the distance between sources within the canopy and the upper boundary of the canopy and σ is the extinction coefficient. An increase in SZA results in longer photon path lengths for positive phase angles (figure S5(c)). The opposite is true for negative phase angles. Increasing SZA with constant canopy therefore results in an asymmetric transformation of the BRF signature, that is, enhanced values for positive phase angles and depressed values for negative phase angles (figure S5(d)). It also decreases the range of BRF variation at positive phase angles and a corresponding increase in the range of BRF variation at negative phase angles. Thus, both the shape and magnitude of the BRF signature are changed. The asymmetric transformation also causes the two BRF signatures to intersect, as illustrated in figure S5(d). The phase angle at which the two signatures intersect can be calculated using the principle of directional reciprocity (Section 4.6).

It is important to note that the path L varies with SZA as $\sim 1/\cos(SZA)$. It means that effect of changing SZA on the BRF's angular shape is weak at low SZA. For example, a change in SZA from 20° to 30° involves a change in L from ~1.06 to ~1.15. The impact, however, increases with SZA. This explains why SZA variation has no discernable impact on the angular signatures of reflectances in figures 3(a) and (b).

4.5. Effect of Changing Canopy Properties and SZA on BRF: figures S5(e) and (f) illustrate the effect of changing both canopy properties and SZA on BRF. Changing canopy properties but holding SZA constant changes the magnitude of BRF but retains its overall angular shape (Section 4.3). Changing SZA but holding canopy properties invariant changes the magnitude of BRF differently for positive and negative phase angles, thus changing the shape of the BRF as well (Section 4.4). Changing canopy properties and SZA simultaneously combines these two effects, i.e. the BRF is transformed asymmetrically and shifted in magnitude. For example, decreasing SZA depresses the BRF at positive phase angles and enhances the same at negative phase angles – transformation of the green colored BRF signature to dashed-blue color signature in figure S5(f). Increasing canopy properties, say LAI and/or foliage optical properties, shifts the overall BRF signature up in magnitude – transformation of the dashed-blue color signature to solid-blue color signature in figure S5(f). This explains the BRF signature changes in figures 3(c) and (d). Importantly, it follows from this argumentation that *higher or equal values of BRF at lower SZA relative to BRFs at higher SZA always indicate a change in canopy properties*.

4.6. Proof of Dry Season Changes From the Directional Reciprocity Principle: The optical reciprocity theorem (Davis and Knyazikhin, 2005) provides a proof relevant to our study. It states that switching detector and source and inverting the directions of propagation yield the same result for BRF. It follows from the theorem that the BRFs of a canopy, or two similar canopies, corresponding to different sun positions, say Ω_0 and Ω_1, necessarily intersect at $\gamma_0 = -\text{acos}(\Omega_0 \cdot \Omega_1)$. Indeed, the BRF in direction Ω_1 due to a mono-directional solar beam in direction $-\Omega_0$ is related to the BRF in direction Ω_0 due to a mono-directional solar beam in direction $-\Omega_1$ as $BRF(-\Omega_0, +\gamma) = BRF(-\Omega_1, -\gamma)$. If $BRF(-\Omega_0, \gamma)$ is symmetric at $\gamma_0 = \text{acos}(\Omega_0 \cdot \Omega_1)$ (e.g., as in October), the BRFs should intersect at $\gamma_0 = -\text{acos}(\Omega_0 \cdot \Omega_1)$. Changing canopy properties with illumination conditions unchanged results in an upward or downward shift in the angular signature of the BRF (Section 4.5). This causes the intersection point to deviate from γ_0, indicating a difference in canopy properties. The deviation of the intersection point around $-5.5°$ from $\gamma_0 = -37.1°$ shown in figure 3(d) is significant, indicating *different canopy properties in June and October*.

Supplementary Discussion

Galvão *et al* (2011) and Morton *et al* (2014) claim that previous studies (Xiao *et al* 2005, Huete *et al* 2006, Myneni *et al* 2007, Brando *et al* 2010, Samanta *et al* 2012) misinterpreted changes in near-infrared (NIR) reflectance caused by seasonal changes in sun-satellite sensor geometry as seasonal variations in rainforest canopy structure and greenness. They conclude that Amazonian rainforests maintain consistent structure and greenness during the dry season based on their analysis of satellite borne sensor data (MODIS and Lidar) and model exercises. Here we present a detailed critique of their analysis.

An incomplete analysis of the seasonal cycle, i.e. one that is focused only on the dry season, encourages misleading interpretation of both intra- and inter-annual greenness (EVI or LAI) variations as artefacts of changing sun-sensor geometry. For example, if the sun-sensor geometry artefact argument is valid, then the seasonal course of LAI from December to May should be similar to that from June to November because of a repeat in sun-sensor geometry (figures 1(b) and (c)), but it is not (figure 1(a)). Also, if the change in MODIS sampling from the orthogonal plane in June to the principal plane in October (figures S2(a) and (c)) causes the rainforests to appear greener, then the change in MISR sampling from the principal plane in June to the orthogonal plane in October (figures S2(b) and (d)) should cause the rainforests to appear browner. But, greening is observed as well (figure 3(d)).

Interannually, the attribution of anomalous dry season greening (increase in EVI or LAI) in drought year 2005, *vis a vis* dry seasons of non-drought years, to a higher proportion of brighter backscattering MODIS observations is flawed because it is selectively based on data from the first fortnight of October (ED-figure 9 (Morton *et al* 2014)). A higher fraction of backscattering measurements is not seen in 2005 when the analysis is focused on July to September period

(figure S4(b)) as in the original studies (Samanta *et al* 2010a, Samanta *et al* 2010b, Saleska *et al* 2007). Moreover, if claims of geometric artefacts are true, higher backscatter fraction and greenness should also be seen during the more intense dry season drought in 2010 (Xu *et al* 2011). They are not (figure S4(b)), even in their selective analysis (ED-figure 9 (Morton *et al* 2014)).

Crucially, the misinterpretations in Morton *et al* (2014) stem from reliance on prognostications of an untested radiative transfer model. In a critical test of how well the model simulates variation in sunlit and shaded proportions of the canopy, which is central to arguments about geometric artefacts, the model underestimates measurements by ~45% (figure S4(c)). The model is also unrealistically sensitive to litter reflectance in dense vegetation (table 1 (Morton *et al* 2014)), an indication of incorrect physics and/or modeling of foliage spatial distribution. The failure to test the model is compounded by an unquestioned belief in its validity, else the observed dry season greening in geometry-corrected EVI would not have been ignored (figure 3(b) (Morton *et al* 2014) and ED-figure 7(b) (Morton *et al* 2014)). Various statistical analyses of this geometry-corrected EVI data strongly reject the null hypothesis of no change in forest greenness (Saleska *et al* 2015). Indeed the physics of radiative transfer in dense media (Section 2.9 (Knyazikhin *et al* 1999)) informs that these changes in geometry-corrected EVI (figure 2, figure 3(b) in (Morton *et al* 2014) and ED-figure 7(b) in (Morton *et al* 2014)) correspond to large changes in LAI (figure. 1(a)). Thus, there is no valid statistical or theoretical basis to dismiss dry season increase in geometry-corrected EVI (figure 2(b), figure 3(b) in (Morton *et al* 2014) and ED-figure 7(b) in (Morton *et al* 2014)).

The unorthodox belief that Amazonian rainforests should conform to model predictions affects their interpretation of satellite lidar data also. The conclusion that structure and greenness of rainforests remain invariant does not follow from absence of evidence in lidar data for their model prediction that an increase in LAI from 4.5 to 6.5 should result in an increase in Waveform Centroid Relative Height - the height of median return energy relative to the full waveform extent (WCRH; table 1 in (Morton *et al* 2014)). A prudent interpretation might be that the model prediction does not conform to data. Even if the model is assumed to be capable of accurate predictions, the predicted change in WCRH (0.06) is comparable to the spatial standard deviations of June and October WCRH data (~0.07). This clearly suggests a need for additional analysis.

The lack of insight into what might be reasonably expected from lidar data and saturation of lidar signals in dense vegetation compound the problem of detecting seasonal LAI changes. For example, studies that have investigated the relationship between LAI and lidar waveforms (Castillo *et al* 2012, Tang *et al* 2012, Drake *et al* 2002) show that WCRH saturates in mature and secondary growth tropical forests aged over ~20 years (Tang *et al* 2012, Drake *et al* 2002) because the majority of lidar hits are confined to the upper canopy. This saturation of signals emanating from vegetation is different than sensor saturation (Neuenschwander *et al* 2008) – the latter have been filtered out from all analyses.

The saturation effect can be potentially documented through these three analyses. First, although a range of LAI values are observed in Amazonian rainforests, from about 4 to 6 in June and greater than 6 in October, the two lidar metrics, WCRH and Apparent Reflectance (AR), exhibit no correspondent variations (figure S6). Second, rainforests with low (3.5 to 4.5) and high (greater than 5.5) LAI have the same WCRH and AR (figures S7 (a) and (b)). Third, rainforests with low (<0.5) and high (>0.6) WCRH have the same LAI (figure S7(c)). Likewise, rainforests with low (<0.5) and high (>0.6) AR have identical LAI (figure S7(d)). Inference of saturation from figure S6 and figures S7 (a)–(d) depends on the validity of the MODIS LAI data. To alleviate this concern, we present similar results for deciduous broadleaf forests where a broader range of LAI values are encountered. The curvilinear relationship in deciduous forests, where WCRH increases for LAI values 0 to 3 and saturates thereafter (figures S8(a) and (c)), is as expected, and is similar to other relations between LAI and remote measurements (Knyazikhin *et al* 1999, Huang *et al* 2008).

Unlike WCRH, the AR shows no relationship to LAI (figures S6 (b) and (d), figures S8 (b) and (d)), even in sparsely foliated canopies (LAI less

than 3; figures S8 (b) and (d)). Also, the inverse relationship with WCRH is perplexing (figures S7 (e) and (f)). To ascertain whether these results indicate potential data quality problems, we investigated the relationship between the lidar metrics and key climatic variables that govern plant growth, i.e. water, radiation and temperature (Nemani *et al* 2003). The WCRH data are positively related (p-value < 0.001) to all three climatic variables (table S4). This is as it should be, i.e. tall and dense tree stands with higher WCRH are located in climatically favorable environments of higher annual precipitation, solar radiation and mean temperature (table S4). The AR data, on the other hand, show negative relation with two of the three climatic variables. We therefore conclude that GLAS AR data have quality problems.

Morton *et al* (2014)'s interpretations of AR data are contradictory - on the one hand, their validity is discounted by citing corruption from aerosols due to biomass burning, and on the other hand, their invariance is counted as proof that Amazonian rainforests maintain consistent structure and greenness (figure 2(c) (Morton *et al* 2014)). Why table 1 (Morton *et al* 2014) does not show model predictions of AR seasonal variations, unlike WCRH, is unknown. Given these ambiguities, their analyses of AR data must also be deemed inconclusive.

In addition to the analyses presented in this article, three independent studies have rebutted Galvão *et al* (2011) and Morton *et al* (2014) claims with a multitude of satellite and in situ data (Maeda *et al* 2014, Hilker *et al* 2014, Jones *et al* 2014). Dry season greening in sun-sensor geometry corrected data obtained from Morton et al. is due for publication (Saleska *et al* 2015).

Supplementary References

Brando P M, Goetz S J, Baccini A, Nepstad D C, Beck P S and Christman M C 2010 Seasonal and interannual variability of climate and vegetation indices across the Amazon. *Proc. Natl. Acad. Sci. USA.* **107** 14685–14690

Castillo M, Rivard B, Sánchez-Azofeifa A, Calvo-Alvarado J and Dubayah R 2012 LIDAR remote sensing for secondary Tropical Dry Forest identification. *Remote Sens. Environ.* **121** 132–143

Davis A B and Knyazikhin Y 2005 A primer in 3D radiative transfer. *Three Dimensional Radiative Transfer in the Cloudy Atmosphere*, eds Marshak A, Davis A B (Springer-Verlag, Berlin Heidelberg), pp 153-242

Drake J B, et al. 2002 Estimation of tropical forest structural characteristics using large-footprint lidar. *Remote Sens. Environ.* **79** 305–319

Galvão L S, Dos Santos J R, Roberts D A, Breunig F M, Toomey M and de Moura Y M 2011 On intra-annual EVI variability in the dry season of tropical forest: A case study with MODIS and hyperspectral data. *Remote Sens. Environ.* **115** 2350–2359

Hilker T *et al* 2014 Vegetation dynamics and rainfall sensitivity of the Amazon. *Proc. Natl. Acad. Sci. USA.* **111** 16041–16046

Huang D *et al* 2008 Stochastic transport theory for investigating the three-dimensional canopy structure from space measurements. *Remote Sens. Environ.* **112** 35–50

Huete A R *et al* 2006 Amazon rainforests green-up with sunlight in dry season. *Geophys. Res. Lett.* **33** L06405

Jones M O, Kimball J S and Nemani R R 2014 Asynchronous Amazon forest canopy phenology indicates adaptation to both water and light availability. *Environ. Res. Lett.* **9** 124021

Knyazikhin Y *et al* 1999 *MODIS leaf area index (LAI) and fraction of photosynthetically active radiation absorbed by vegetation (FPAR) product (MOD15) algorithm theoretical basis document*, <https://lpdaac.usgs.gov/products/modis_products_table/mcd15a2>

Lyapustin A I *et al* 2012 Multi-angle implementation of atmospheric correction for MODIS (MAIAC): 3. Atmospheric correction. *Remote Sens. Environ.* **127** 385–393

Maeda E E, Heiskanen J, Aragão L E O C and Rinne J 2014 Can MODIS EVI monitor ecosystem productivity in the Amazon rainforest? *Geophys. Res. Lett.* **41** 7176–7183

Morton D C *et al* 2014 Amazon forests maintain consistent canopy structure and greenness during the dry season. *Nature* **506** 221–224

Myneni R B *et al* 2007 Large seasonal swings in leaf area of Amazon rainforests. *Proc. Natl. Acad. Sci. USA* **104** 4820–4823

Nemani R R *et al* 2003 Climate-driven increases in global terrestrial net primary production from 1982 to 1999. *Science* **300** 1560–1563

Nepstad D C *et al* 1994 The role of deep roots in the hydrological and carbon cycles of Amazonian forests and pastures *Nature* **372** 666–669

Neuenschwander A L, Urban T J, Gutierrez R and Schutz B E 2008 Characterization of ICESat/GLAS waveforms over terrestrial ecosystems: Implications for vegetation mapping. *J. Geophys. Res. Biogeosci.* **113** G02S03

Poulter B and Cramer W 2009 Satellite remote sensing of tropical forest canopies and their seasonal dynamics. *Int. J. Remote Sens.* **30** 6575–6590

Saleska S R *et al* 2015 Dry-season greening of Amazon forests. Brief Communications Arising in *Nature* (in press)

Saleska S R, Didan K, Huete A R and Da Rocha H R 2007 Amazon forests green-up during 2005 drought. *Science* **318** 612–612

Samanta A *et al* 2010a Amazon forests did not green-up during the 2005 drought. *Geophy. Res. Lett.* **37** L05401

Samanta A *et al* 2012 Seasonal changes in leaf area of Amazon forests from leaf flushing and abscission. *J. Geophys. Res. Biogeosci.* **117** G01015

Samanta A, Costa M H, Nunes, E L, Vieira S A, Xu, L and Myneni R B 2011 Comment on "Drought-Induced Reduction in Global Terrestrial Net Primary Production from 2000 Through 2009". *Science* **333** 1093

Samanta A, Ganguly S and Myneni R B 2010b MODIS Enhanced Vegetation Index data do not show greening of Amazon forests during the 2005 drought. *New Phytol.* **189** 11–15

Tang H *et al* 2012 Retrieval of vertical LAI profiles over tropical rain forests using waveform lidar at La Selva, Costa Rica. *Remote Sens. Environ.***124** 242–250

WWW-ASDC. NASA Langley Research Center Atmospheric Science Data Center (ASDC) Home page. Available at https://eosweb.larc.nasa.gov/

WWW-CERES. Atmospheric Science Data Center: The Clouds and the Earth's Radiant Energy System (CERES). Available at https://eosweb.larc.nasa.gov/project/ceres/ceres_table

WWW-CRU. Climatic Research Unit (CRU) Time-Series High-Resolution Gridded Datasets. Available at http://www.cru.uea.ac.uk/cru/data/hrg/

WWW-GLAS. Geoscience Laser Altimeter System (GLAS) lidar waveform data. Available at https://nsidc.org/data/icesat/data-dictionaries-landing-page.html

WWW-MAIAC. MAIAC Amazon Data. *Level 1 and Atmosphere Archive and Distribution System (LAADS)*. Available at ftp://ladsweb.nascom.nasa.gov/MAIAC/

WWW-MCD12Q1. Land Cover Type Yearly L3 Global 500 m SIN Grid (MCD12Q1). *Land Process Distributed Active Archive Center*. Available at https://lpdaac.usgs.gov/products/modis_products_table/mcd12q1

WWW-MOD13A2. Vegetation Indices 16-Day L3 Global 1km (MOD13A2). *Land Process Distributed Active Archive Center*. Available at https://lpdaac.usgs.gov/products/modis_products_table/myd13a12

WWW-MOD15A2. Leaf Area Index - Fraction of Photosynthetically Active Radiation 8-Day L4 Global 1km (MOD15A2). *Land Process Distributed Active Archive Center.* Available at https://lpdaac.usgs.gov/products/modis_products_table/mod15a12

WWW-MYD13A2. Vegetation Indices 16-Day L3 Global 1km (MYD13A2). *Land Process Distributed Active Archive Center*. Available at https://lpdaac.usgs.gov/products/modis_products_table/myd13a12

WWW-TRMM. Tropical Rainfall Measuring Mission (TRMM) data. *Goddard Earth Science Data and Information Center*. Available at http://mirador.gsfc.nasa.gov/

Xiao X *et al* 2005 Satellite-based modeling of gross primary production in a seasonally moist tropical evergreen forest. *Remote. Sens. Environ.* **94** 105–122

Xu L *et al* 2011 Widespread decline in greenness of Amazonian vegetation due to the 2010 drought. *Geophy. Res. Lett.* **38** L07402

Yang W *et al* 2006 MODIS leaf area index products: From validation to algorithm improvement. *IEEE Trans. Geosci. Remote. Sens.* **44** 1885–1898

Supplementary Figures

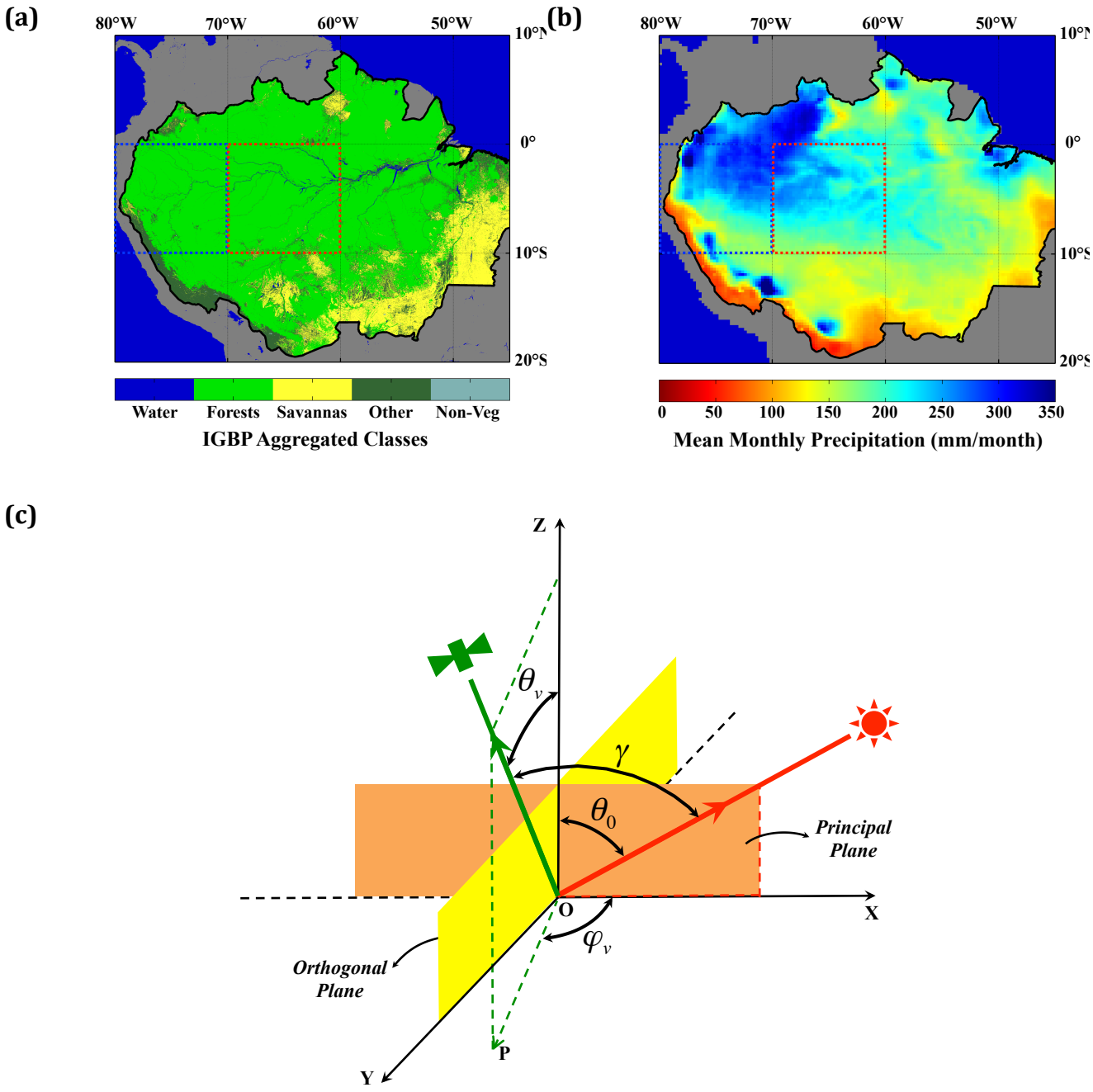

Figure S1. The study domain and sun-sensor geometry. (a) The domain of MODIS and MISR analysis is the red square. The domain of GLAS lidar analysis is both blue and red squares. (b) Monthly mean rainfall from TRMM. (c) Three angles characterize the sun-sensor measurement geometry of a pixel: (1) solar zenith angle, SZA=θ_0 ($0° < \theta_0 \leq 90°$), (2) view zenith angle, VZA=θ_v ($0° \leq \theta_v \leq 90°$) and (3) view azimuth, φ_v ($0° \leq \varphi_v \leq 360°$), measured relative to the principal plane. The angle between the projection, OP, of the direction to the sensor and X axis is the relative azimuth angle (RAA), i.e., RAA=φ_v if $0 \leq \varphi_v < 180°$ and RAA=$360° - \varphi_v$, otherwise. It varies between 0° and 180°. The angle between the directions to the sun and sensor is the phase angle, PA=γ.

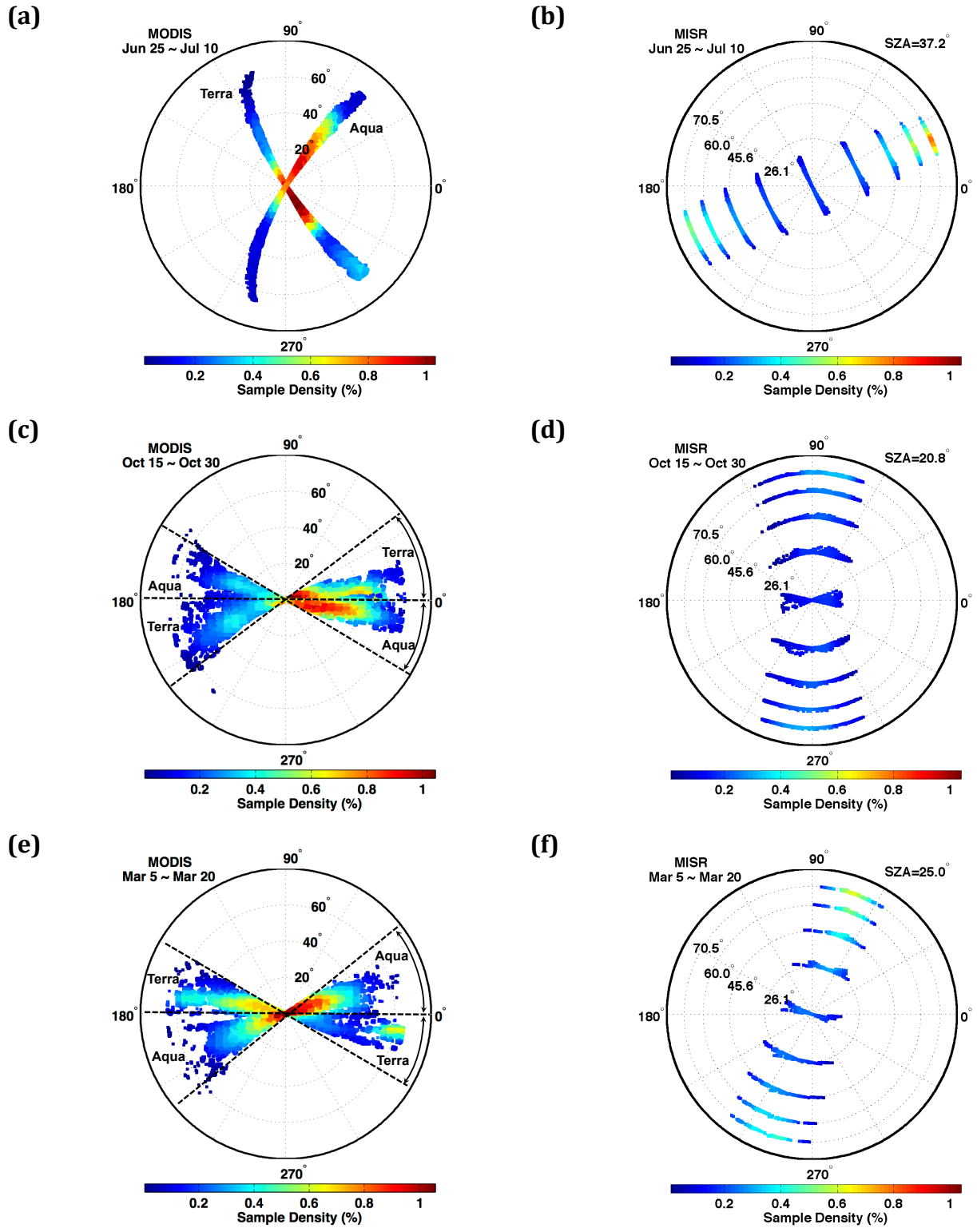

Figure S2. MODIS and MISR sampling geometries. Terra and Aqua MODIS (left panels) and Terra MISR (right panels) sampling geometries during a 16-day compositing period in the months of (a, b) June 2003, (c, d) October 2003, and (e, f) March 2003. The MODIS sensors sample the surface close to the orthogonal plane in June and near the principal plane in October and March. This sampling is opposite to that of MISR sensor.

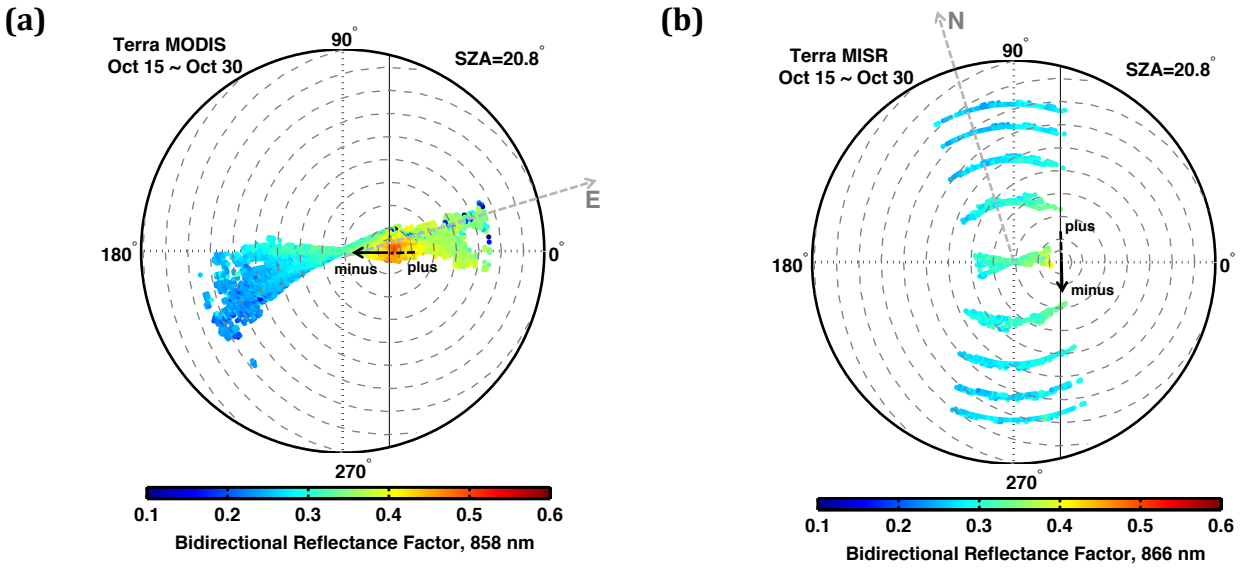

Figure S3. MODIS and MISR reflectances in a modified coordinate system. Terra MODIS (a) and MISR (b) NIR BRFs during a 16-day composite in October 2003. BRF values are expressed in a coordinate system with the polar axis pointed to the Sun. Solid arrows indicate sampling direction that determines the phase angle sign (angle between solar and sensor view directions).

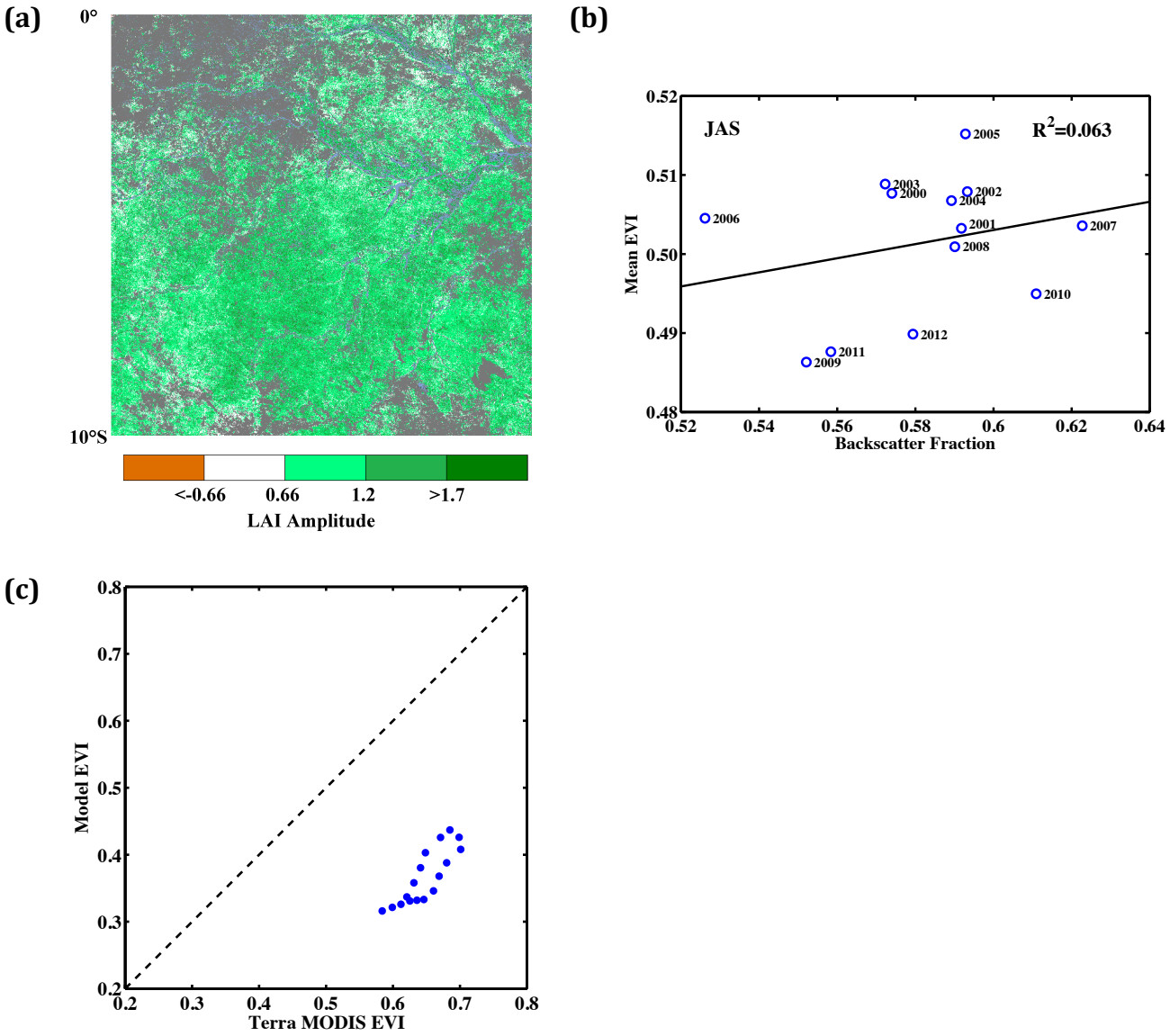

Figure S4. Evidence for seasonality of leaf area and misinterpretation of data following the guidance of an erroneous radiative transfer model (Morton *et al* 2014). (a) Spatial pattern of seasonal Terra MODIS LAI amplitude expressed as the difference between the maximum value during September to November and the minimum value during the following May to June period. White pixels denote locations with LAI amplitudes less than |0.66|, which is the accuracy of MODIS LAI data (Yang *et al* 2006). White and colored pixels together denote pixels that exhibited dry season greening in at least 4 out of 7 seasonal cycles (63% of all forest pixels in the study region). (b) Mean Terra MODIS EVI over rainforests as a function of backscattering fraction evaluated from all 16-day compositing periods in July, August and September (DOY 177 to 272). The backscattering fraction is defined (Morton *et al* 2014) as the fraction of observations with view azimuth less than 90° and greater than 270°. (c) Comparison of model simulated EVI (obtained by digitizing figure 1(c) in Morton *et al* (2014)) with Terra MODIS EVI over Amazonian rainforests. The MODIS EVI is from a 16-day October composite (15th to the 30th) accumulated over 7 seasonal cycles (Section 2.5). The comparison is for phase angles in the range ±10°, that is, ±10° around the hot spot (view zenith angles from 10° to 30° in figure 1(c) of (Morton *et al* 2014)).

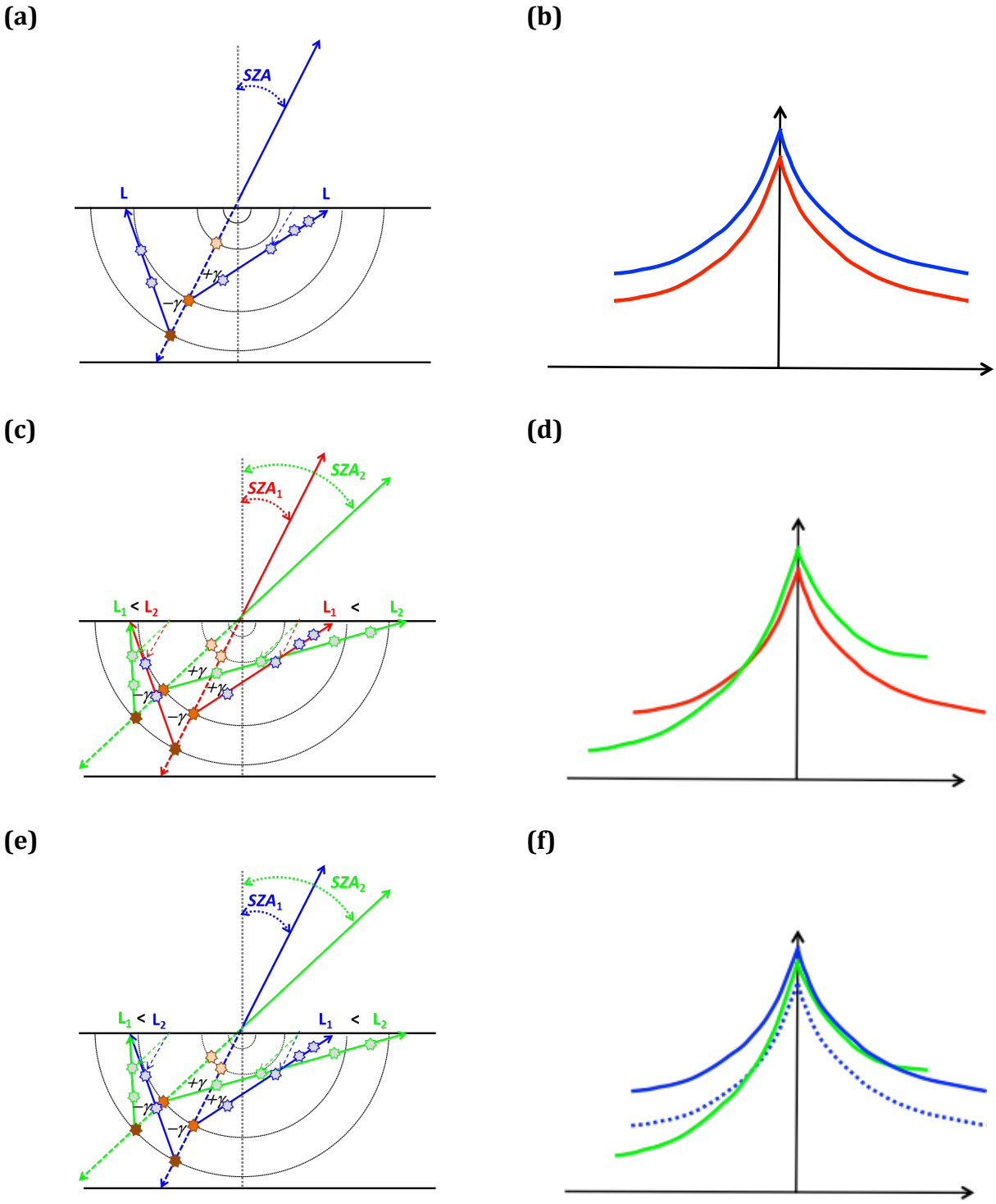

Figure S5. Interpretation of angular signatures of reflectance. Illustration of how the angular signature of Bidirectional Reflectance Factors (BRF) is transformed when (a, b) sun-sensor geometry is held invariant but canopy properties are changed; (c, d) sun-sensor geometry is changed but canopy properties are held invariant; (e, f) both sun-sensor geometry and canopy properties are changed. The dashed arrows depict direction of incident parallel beam of unit intensity.

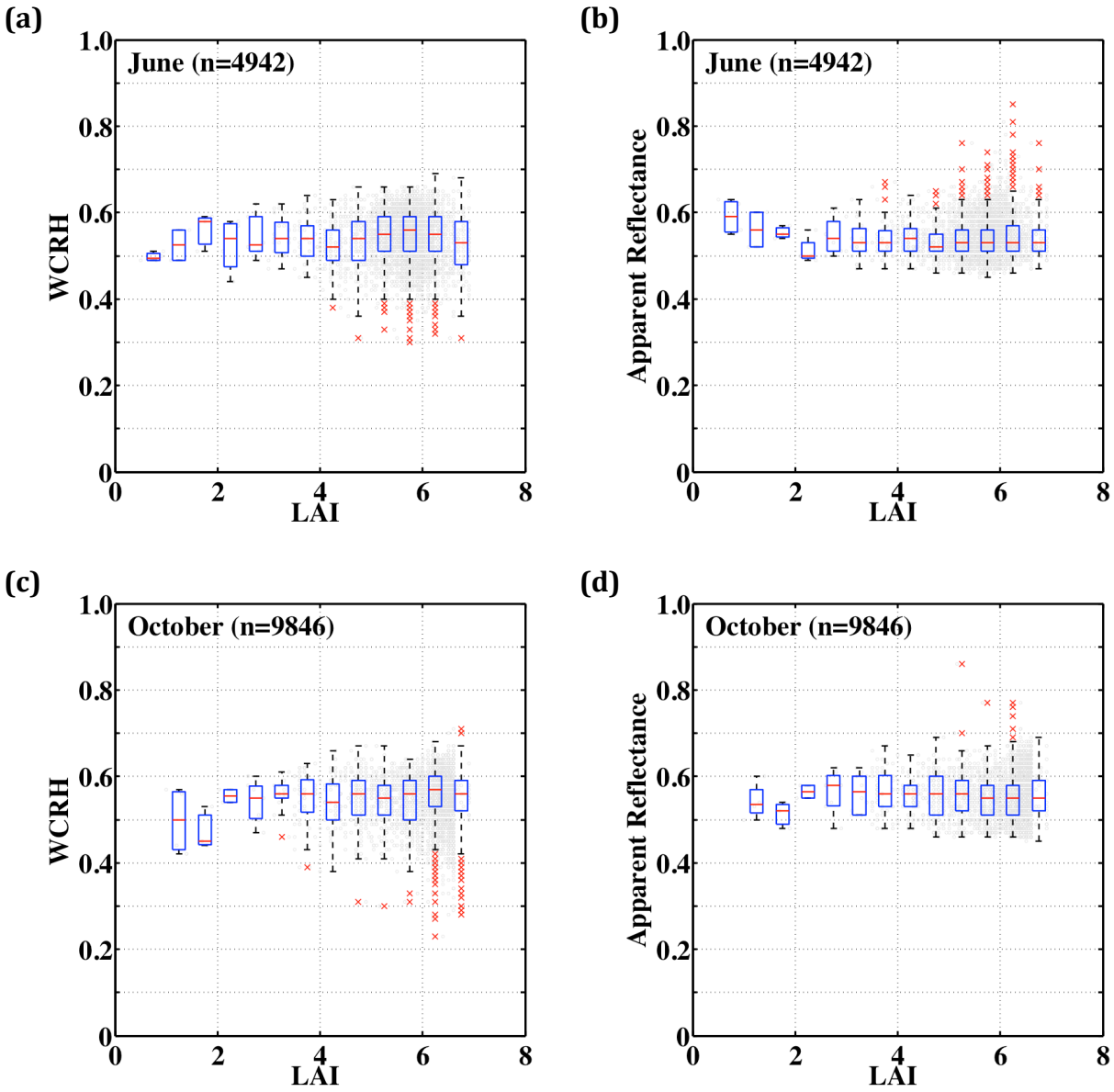

Figure S6. Saturation of GLAS lidar metrics over central Amazonian forests. Distributions of GLAS Waveform Centroid Relative Height (WCRH) and Apparent Reflectance as a function of Terra MODIS LAI in the case of central Amazonian rainforests at the (a, b) beginning and (c, d) end of the dry season. Gray dots and red crosses show distributions of lidar metrics within 0.5 LAI bins. Upper, middle (red line) and lower box edges show the 75%, 50% and 25% percentiles of GLAS metrics. The red crosses are outliers, each representing upper and lower 0.25% of the GLAS lidar observations. June represents data from May-20 to June-23, 2005 and May-24 to June-26, 2006. October represents data from October-3 to November-8, 2004 and October-2 to November-5, 2007. MODIS pixels with valid LAI values and four or more GLAS lidar observations were used (table S3).

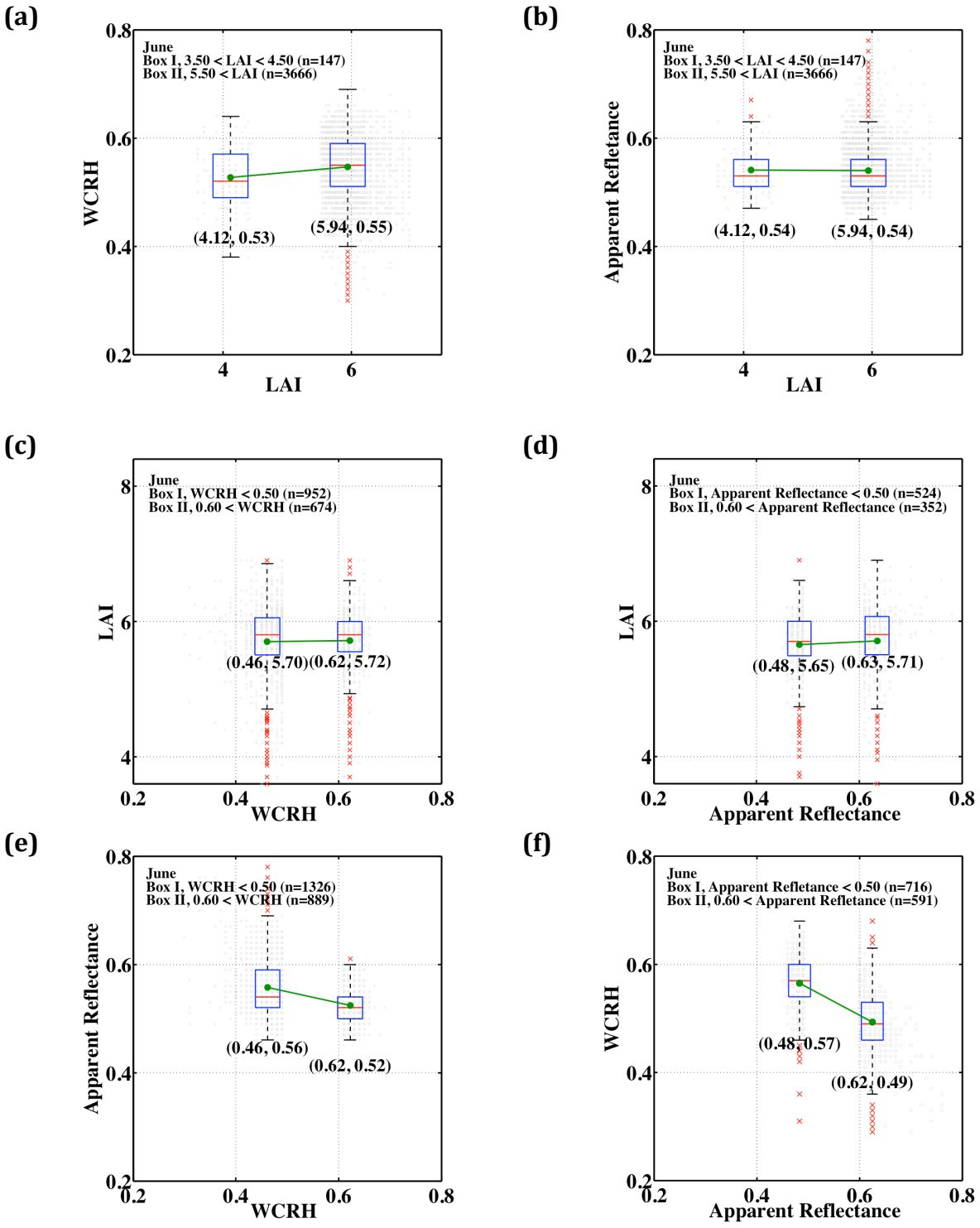

Figure S7. Relationship between GLAS lidar metrics and with LAI. (a, b) Variation in GLAS Waveform Centroid Relative Height (WCRH) and Apparent Reflectance (AR) for pixels with low and high Terra MODIS LAI values. (c, d) Variation in LAI for pixels with low and high values of WCRH and AR. (e, f) Relationship between WCRH and AR. Gray dots and red crosses show the data. Upper, middle (red line) and lower box edges separate the 75%, 50% and 25% percentiles of data used. The red crosses are outliers, each representing upper and lower 0.25% of the data. Similar relations are found for October (not shown).

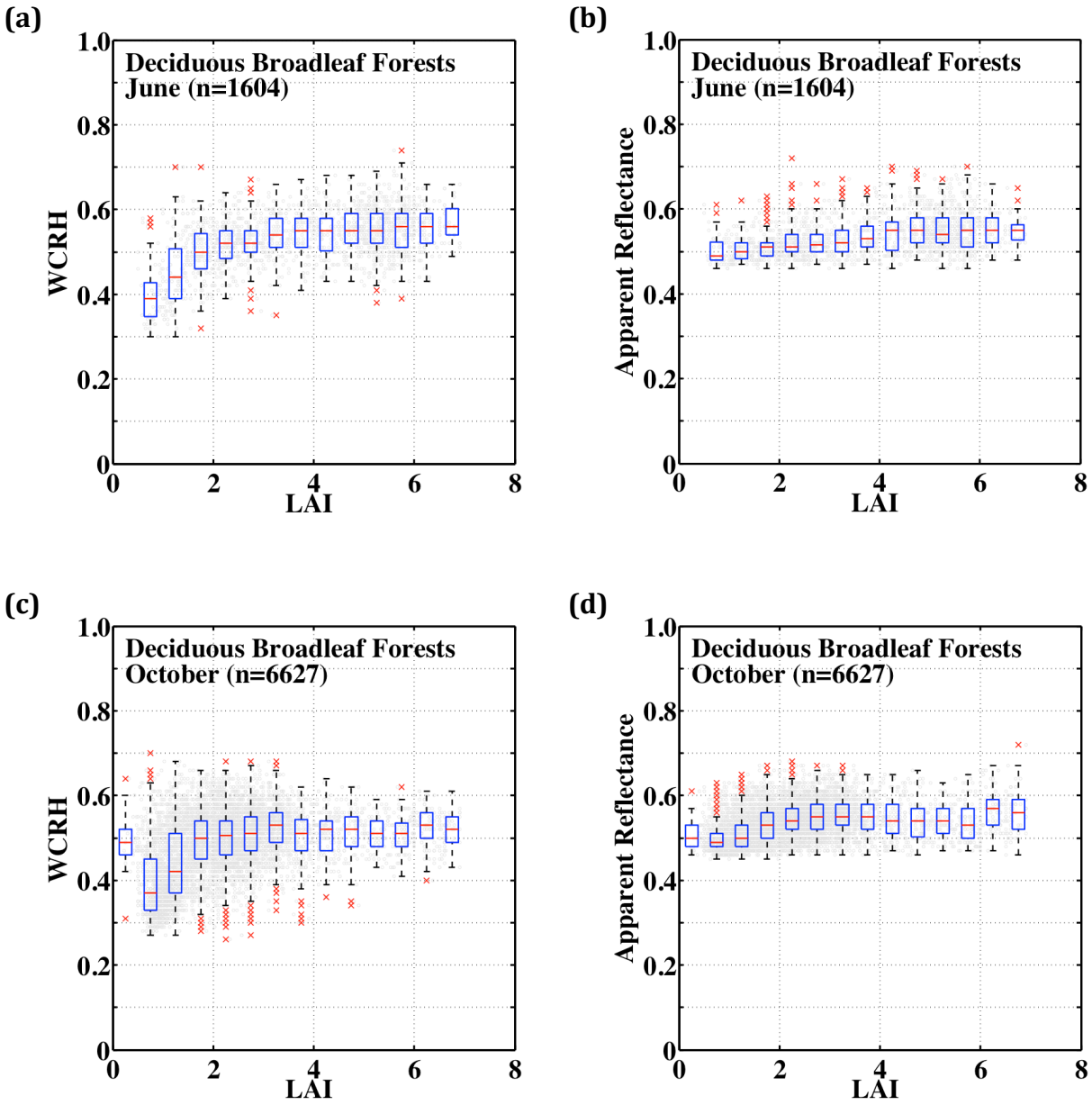

Figure S8. Relationship between GLAS lidar metrics and LAI in deciduous broadleaf forests. Distributions of GLAS Waveform Centroid Relative Height (WCRH) and Apparent Reflectance as a function of Terra MODIS LAI in the case of deciduous (temperate) broadleaf forests in the northern hemisphere in (a, b) June and (c, d) October. Gray dots and red crosses show distributions of lidar metrics within 0.5 LAI bins. Upper, middle (red line) and lower box edges show the 75%, 50% and 25% percentiles of GLAS metrics. The red crosses are outliers, each representing upper and lower 0.25% of the GLAS lidar observations. June represents data from May-20 to June-23, 2005 and May-24 to June-26, 2006. October represents data from October-3 to November-8, 2004 and October-2 to November-5, 2007. MODIS pixels with valid LAI values and four or more GLAS lidar observations were used (table S3).

Supplementary Tables

Table S1. Number of greening pixels (Section 1) from Terra and Aqua MODIS sensors

	Terra		Aqua	
Year	Number of greening pixels	As a % of rainforest pixels	Number of greening pixels	As a % of rainforest pixels
2000	804,550	59.02	N/A	N/A
2001	723,796	53.10	N/A	N/A
2002	990,863	72.69	N/A	N/A
2003	518,857	38.06	238,998	17.53
2004	919,820	67.48	233,140	17.10
2005	N/A	N/A	N/A	N/A
2006	901,602	66.14	227,926	16.72
2007	783,164	57.45	260,370	19.10

Table S2. Number of pixels with valid EVI and BRF data in June, October and March accumulated over a 7-year period (June 2000 to May 2008, excluding June 2005 to May 2006 due to the dry season drought in 2005) from Terra MODIS and MISR sensors. The table also shows the same for the Aqua MODIS sensor, but accumulated over a 4-year period (June 2003 to May 2008 excluding June 2005 to May 2006)

		Fraction of Rainforest Pixels With Valid Data (%)		
Sensor	Number of Valid Data	June	October	March
Terra MODIS	One or more	96.67	94.38	70.92
Aqua MODIS	One or more	33.65	30.32	12.10
Terra MISR	One or more	48.07	25.75	15.33

Table S3. Number of pixels with valid Terra MODIS LAI data and four or more valid GLAS footprints in June and October

	June		October	
Year	Number of valid LAI pixels	Number of corresponding GLAS footprints	Number of valid LAI pixels	Number of corresponding GLAS footprints
		Amazonian Rainforests		
2004	N/A	N/A	3,859	17,293
2005	3,031	13,536	N/A	N/A
2006	1,911	8,607	N/A	N/A
2007	N/A	N/A	5,987	29,858
Total	4,942	22,143	9,846	47,151
		Deciduous Broadleaf Forests		
2004	N/A	N/A	2,419	10,719
2005	955	4,164	N/A	N/A
2006	649	2,761	N/A	N/A
2007	N/A	N/A	4,208	19,650
Total	1,604	6,925	6,627	30,369

Table S4. Regression relationships between climate and GLAS Waveform Centroid Relative Height (WCRH) and Apparent Reflectance (AR). Climate is represented by annual total precipitation from TRMM, photosynthetically active radiation from CERES and mean annual temperature from CRU. Long-term means of climate variables were evaluated from 2001 to 2010 data, but excluding 2005 and 2010 drought years. Each TRMM pixel contains 10 or more GLAS observations; CERES pixel has 160 or more, and CRU pixel has 40 or more

x	y	Slope	Intercept	R^2	p-value
WCRH	Annual Precipitation (mm $year^{-1}$)	4428.3	297.1	0.17	<0.001
WCRH	Photosynthetically Active Radiation (W m^{-2})	21.8	83.6	0.08	<0.001
WCRH	Mean Annual Temperature (°C)	8.3	22.1	0.15	<0.001
AR	Annual Precipitation (mm $year^{-1}$)	-600.4	3011.2	0.00	0.16
AR	Photosynthetically Active Radiation (W m^{-2})	-65.6	130.9	0.26	<0.001
AR	Mean Annual Temperature (°C)	-10.3	32.1	0.10	<0.001

Table S5. List of Abbreviations

AR	Apparent Reflectance
Aqua	NASA scientific research satellite in a Sun-synchronous near polar circular orbit around the Earth; crosses Equator at 1:30pm
BRF	Bidirectional Reflectance Factor
C5	Collection 5
CERES	Clouds and the Earth's Radiant Energy System
CRU	Climatic Research Unit
DOY	Day of Year (designates the beginning of the compositing period)
ED	Extended Data
EVI	Enhanced Vegetation Index
GLAS	Geoscience Laser Altimeter System
ICESat	Ice, Cloud and land Elevation Satellite
JAS	July, August, and September
LAI	Leaf Area Index
LiDAR	Light Detection and Ranging
MAIAC	Multi-angle Implementation of Atmospheric Correction
MISR	Multiangle Imaging Spectroradiometer
MODIS	Moderate-resolution Imaging Spectroradiometer
NASA	National Aeronautics and Space Administration
NIR	Near Infrared
PA	Phase angle
PAR	Photosynthetically Active Radiation
PDF	Probability Density Function
RAA	Relative Azimuth Angle between solar and sensor view directions
SI	Supplementary Information
SZA	Solar Zenith Angle
SOM	Space Oblique Mercator
Terra	NASA scientific research satellite in a Sun-synchronous near polar circular orbit around the Earth; crosses Equator at 10:30am
TRMM	Tropical Rainfall Measuring Mission
VI	Vegetation Index
VZA	View Zenith Angle
WCRH	Waveform Centroid Relative Height